NTNU

Norwegian University of
Science and Technology

Wake Measurements Behind An Array Of Two Model Wind Turbines

Jan Bartl

Master's Thesis

Submission date: October 2011

Supervisor: Lars Sætran, EPT

Co-supervisor: Fabio Pierella, EPT

Norwegian University of Science and Technology
Department of Energy and Process Engineering

ABSTRACT

During the last decades the exploitation of energy from the wind has become one of the most promising renewable energy technologies. The main strive in today's development of wind turbines is to increase the efficiency of the turbine and to build bigger rotors that are able to extract more power out of the wind.

When it comes to the planning and designing of a wind park, also the aerodynamic interactions between the single turbines must be taken into account. The flow in the wake of the first row turbines is characterized by a significant deficit in wind velocity and by increased levels of turbulence. Consequently, the downstream turbines in a wind farm cannot extract as much power from the wind anymore. Furthermore, the additional turbulence in the wake could be a reason for increased material fatigue through flow-induced vibrations at the downstream rotor.

The main focus of this experimental study is to investigate the local velocity deficit and the turbulence intensities in the wake behind an array of two model wind turbines. For two different turbine separation distances, the wake is scanned at several different downstream positions behind the second model turbine. Thus, it is possible to map the axial development of mean velocity and turbulence intensity and to evaluate the influence of turbine separation distance. Furthermore, the effect of varying tip speed ratios of the first and second turbine onto the wake flow field is investigated.

The experiments are performed at the wind tunnel (1.9m x 2.7m cross section) at NTNU Trondheim using two model wind turbines with a rotor diameter of 0.9m. A hot wire probe is used to scan the wake behind the model turbines in defined positions.

The velocity deficit and the turbulence intensity behind an array of two turbines are found to be significantly higher than behind one unobstructed turbine. Moving axially downstream, a gentle broadening of the wake can be observed. The wake profiles measured in close distances behind the rotor are characterized by evident asymmetries. Further downstream in the wake, the flow field becomes more symmetrical. The flow conditions in the inner part of the wake behind the two turbines are observed to be mainly dominated by the operational characteristics of the second turbine rotor. Although the first turbine has hardly any influence on the inner part of the wake, the outer dimensions of the wake can be tracked back to the influence of the first turbine.

AFFIDAVIT

I hereby declare that I wrote thesis on my own without any assistance from a third party. I confirm that no sources have been used other than those clearly marked as other sources. This thesis has not been received by any examination board, neither in this nor in a similar form.

Trondheim, October 31th, 2011

ACKNOWLEDGEMENTS

The present thesis has been performed at Norges Teknisk-Naturvitenskapelige Universitet (NTNU) in Trondheim. It will be submitted for the degree Diplom-Ingenieur at Technische Universität München (TUM) as well as for the degree Civilingenjör at Kungliga Tekniska Högskolan (KTH) in Stockholm.

Many people have been involved in supervising this thesis, who I would like to express my gratitude to:

First of all, I would like to thank Professor Lars Sætran at the Department of Energy and Process Engineering at NTNU for giving me the opportunity to work on this thesis. Thank you for many fruitful discussions and for always being available when help was needed.

My biggest thanks goes to Fabio Pierella with whom I spent numerous hours in the wind tunnel throughout this project. Thank you for teaching me all the experimental procedures, for your creative ways of solving problems but above all for a fun time in and outside of the wind tunnel laboratory.

Also, I would like to thank Pål Egil Eriksen at the Department of Energy and Process Engineering at NTNU whose self-written data conversion programs I used for the evaluation of the hot wire signals.

At TUM I would like to thank Professor Rudolf Schilling at the Chair of Fluid Mechanics for supervising and accrediting this thesis from distance.

Special thanks to Matthias Faust who helped in organizing with words and deeds before the thesis even started.

Many thanks to Andreas Rosenberger for taking over the supervision at TUM. Thank you for proofreading and your helpful comments.

At KTH I would like to thank Damian Vogt of the Department for Heat and Power Technology for officially examining this thesis.

Many thanks to Miroslav Petrov for supervising the project at KTH and for organizing all the paper work involved with this thesis.

Special thanks to Jens Fridh for imparting the contact to Miro and for teaching me how to work experimentally during my time at KTH. During this thesis I could profit in many ways from what I have learned back then.

Finally, I would like to thank my friends Andreas Hövelmann and Michael Tiefenbrunn for proofreading. Thank you for your helpful comments and corrections.

TABLE OF CONTENTS

LIST OF FIGURES

LIST OF TABLES

NOMENCLATURE

Latin Symbols

A	Area	[m²]
c	Cord length	[mm]
C	Coefficient	[-]
D	Rotor Diameter	[mm]
F	Force	[N]
p	Pressure	[Pa]
r	Radius	[mm]
R	Rotor radius	[mm]
Re	Reynolds number	[-]
T	Torque	[Nm]
U	Absolute velocity	[m/s]
V	Relative velocity	[m/s]
x	x-coordinate	[mm]
y	y-coordinate	[mm]
z	z-coordinate	[mm]

Greek Symbols

β	Pitch angle	[°]
γ	Yaw angle	[°]
ρ	Density	[kg/m³]
λ	Tip speed ratio	[-]
θ	Circumferential component	[-]
υ	Kinematic viscosity	[m²/s]
ω	Rotational Speed	[1/s]

Subscripts

avg	Average
ax	Axial reference
hub	Hub
m	Mean

max	Maximum
min	Minimum
rot	Axial measurement station in the plane of the rotor
P	Power
stat	Static
T	Thrust
tip	Tip
tot	Total
Tu1	first (upstream) model wind turbine
Tu2	second (downstream) model wind turbine

Abbreviations

ACD	Actuator Disc Method
AD	Anno Domini
BC	Before Christ
CAD	Computer Aided Design
CFD	Computational Fluid Dynamics
CTA	Constant Temperature Anemometry
EEA	European Environment Agency
GWEC	Global Wind Energy Council
HAWT	Horizontal Axis Wind Turbine
KTH	Kungliga Tekniska Högskolan
NTNU	Norges Teknisk-Naturvitenskapelige Universitet
LDA	Laser Doppler Anemometry
LES	Large Eddy Simulation
PS	Pressure Side
RPM	Revolutions per Minute
SS	Suction Side
TE	Trailing Edge
TI	Turbulence Intensity
TSR	Tip Speed Ratio
Tu1	First (upstream) model wind turbine
Tu2	Second (downstream) model wind turbine
TUM	Technische Universität München

1 BACKGROUND

1.1 Wind Power

The exploitation of wind energy and its conversion to useful energy is one of the oldest methods in energy transformation. The earliest known utilization of wind power was in sailing boats which used the aerodynamic drag and lift forces. Around 1700 BC a wind powered system was used to irrigate agricultural fields in ancient Mesopotamia [1]. Almost two millenniums later, about 500-900 AD, the first windmills were developed in old Persia. In early developments of windmills the kinetic energy in the wind was converted into mechanical energy which was at that time primarily used for grinding grain and pumping water [2].

The first windmills designed for electric power production were developed in the late 19th century in more or less at the same time in the United States, Scotland and Denmark. In the beginning of the 20th century fossil fuelled developments began to dominate the power production all over the world, relegating wind power devices a rather insignificant role in small-scale applications. The renewed interest in wind power for electric power production arose in the late 1960s as the first signs of fossil fuel resources being finite emerged. Wind as a primary energy resource was eventually considered to have a significant potential for electrical power production [3]. The first countries to seize the potential of wind power and setting up commercial wind turbines were Denmark, Germany and the United States.

In the late 1990s a new awareness of a sustainable management of energy resources evolved, stimulating a renewed interest in renewable energy sources. This could be ascribed to substantial drawbacks of both fossil fuelled power plants and nuclear power plants regarding their sustainability. From both sides of the Atlantic one could hear politicians speak of a “global clean-energy revolution” [4] in which the exploitation of wind power could play an essential role. From a global point of view wind power is one of the most promising renewable energy sources as wind is available everywhere on the planet and at some places even features a considerable energy density.

In the end of each calendar year the Global Wind Energy Council (GWEC) publishes a report on the state of the global wind energy market. The latest report for 2010 shows the enormous significance of today’s wind industry. Although the annual growth rate

decreased for the first time, the globally installed wind power capacity increased by 24.1% and in the end of 2010 stands at 197.0 GW. [5]

In terms of capacity China with 44.7 GW installed wind power took over the lead from the United States, which currently have 40.2 GW installed. Within Europe the biggest capacities are set up in Germany and Spain, making up a total of 27.2 GW respectively 20.7 GW in the end of 2010 [5]. Norway's share is considerably smaller as it has lower energy needs and is almost completely supplied by hydropower. Norway's installed wind power comprises a total installed power of 0.4 GW in the end of 2009 [6]. However, Norway could play an important role in the future energy supply in Europe having a large potential for onshore and offshore wind power in its coastal regions at the Atlantic Ocean [7]. As Norway already is the largest hydropower producer in Europe there are considerations that the Norwegian hydropower plants could act as a balance for the growing amount of intermittent wind power entering the electrical grid. Therefore, experts consider Norway to become the "battery" for renewable energy within Europe [8].

According to the European Environment Agency (EEA) wind power can play a key role in achieving Europe's future energy targets. For the year 2030 the EEA predicts an economically competitive potential of 30400 TWh for Europe, of which 27000 TWh would be produced by onshore wind farms and 3400 TWh by offshore wind farms [9]. As the installation and maintenance of onshore wind power is much cheaper and economically more competitive, the main focus is directed on the exploitation of onshore potentials until 2030 [9].

1.2 Wind Turbine Aerodynamics

In the following section it is tried to give an elementary overview of the most important aerodynamic concepts concerning a wind turbine. Starting with the rotating wind turbine as an energy extraction device, it is thereafter looked into the basics of wind turbine blade aerodynamics. Finally, the basic aerodynamic conditions that prevail in a wind turbine wake are presented. However, wind turbine aerodynamics is a very complex field of which many aspects are not yet completely investigated.

1.2.1 Energy Extraction from the Wind

Any kind of fluid contains energy which can exist in different forms: potential energy, thermodynamic pressure, kinetic energy and thermal energy [10]. When looking into basic wind turbine aerodynamics only the kinetic energy and the pressure energy contained in the wind are relevant. Temperature and potential effects in a wind flow can be neglected. As a wind turbine by definition extracts kinetic energy from the wind, the wind passing through the wind turbine rotor has to slow down.

Assuming a boundary between the mass of air passing through the rotor and the unaffected flow a circular stream tube can be imagined as depicted in *Fig. 1.1*. For air flows below $Ma = 0.3$, density changes in the air can be neglected. Under normal ambient conditions, an air flow, which is slower than $U = 100\,m/s$, can be regarded as an incompressible flow. According to the continuity equation the mass flow rate along the stream tube must be constant.

$$\rho A_1 U_1 = \rho A_{Rotor} U_{Rotor} = \rho A_2 U_2 \tag{1.1}$$

Consequently, the cross sectional area of the stream tube must become wider as the wind is slowed down by the rotor. However, the wind velocity does not suddenly change over the rotor, it decreases continuously. Starting in a certain distance in front of the rotor plane, the kinetic energy in the wind is transformed to pressure energy as the blockage of the rotor affects the flow upstream of the rotor.

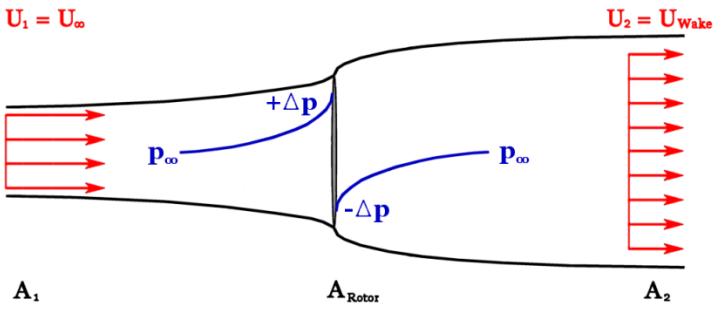

Fig. 1.1: *Imaginary wind tube around a wind turbine rotor showing a decrease in wind velocity and a distinct pressure drop over the rotor*

The static pressure built up upstream of the rotor, on the other hand, is reduced in one distinctive step as shown in *Fig. 1.1*. The air exiting from the rotor is at a static pressure

level below the atmospheric pressure. As the velocity in the imaginary wind tube continues to decrease downstream of the rotor the static pressure rises again and reaches the atmospheric pressure level p_∞ at a certain distance downstream of the rotor [11].

The energy extracted from the wind is partly converted into mechanical energy on the rotor shaft, whereas the other part is dissipated by the generated turbulence in the downstream flow field [11]. When quantifying the power extracted by wind turbine usually a simplified model, called the "Actuator Disc Concept", is used. The turbine rotor is reduced to a simple actuator disc, which induces a velocity variation to the free-stream flow.

Combining the kinetic energy $E_{kin} = \frac{1}{2} m {U_\infty}^2$ and the air mass flow $\dot{m} = \rho U_\infty A$, the power $P_{windtube}$ contained in the imaginary wind tube can be quantified as follows.

$$P_{windtube} = \frac{1}{2} \rho A_{rot} {U_\infty}^3 = \frac{1}{8} \rho \pi {D_{rot}}^2 {U_\infty}^3 \tag{1.2}$$

As the density of the air ρ is almost constant for a normal range of wind velocities, the power $P_{windtube}$ grows proportionally with the cube of the wind velocity U_∞. Moreover, it is obvious that the power available in the imaginary wind tube $P_{windtube}$ increases with the square of the rotor diameter D_{rot}.

One of the most important parameters for wind turbines is the non-dimensional power coefficient C_P, which is defined as the actually extracted power on the rotor axle divided by the maximum power contained in the wind tube.

$$C_P = \frac{P_{rot}}{\frac{1}{2} \rho A_{rot} U_\infty^3} \tag{1.3}$$

Applying the momentum theory, the German aerodynamicist Albert Betz [12] found in 1920 that the maximum power extractable from the wind in an imaginary wind tube amounts

$$C_{P,max} = \frac{16}{27} \approx 0.593 \tag{1.4}$$

This is called the Betz Limit and until today no wind turbine has been designed surpassing this limit. The complete derivation of the Betz Limit can be found in many text books dealing with wind turbine aerodynamics, such as [3] or [11].

Another important parameter used to describe the performance of a wind turbine is the thrust coefficient C_T, which is often used to describe the load onto the turbine blades and the structural design of the turbine tower. It is defined as the total axial thrust force F_T onto the rotor divided by a dynamic reference force from the wind onto the rotor area.

$$C_T = \frac{F_T}{\frac{1}{2}\rho A_{rot} U_\infty^2} \tag{1.5}$$

In theory the power coefficient C_P can be increased by increasing rotational speed of the turbine, by increasing the number of rotor blades or by increasing the lift by either pitching the blades or increasing chord length [11].

The rotational speed ω of the turbine is often represented by a non-dimensional parameter called tip speed ratio λ which is defined as the speed of the rotor tip divided by the approaching wind speed U_∞.

$$\lambda = \frac{\omega R}{U_\infty} \tag{1.6}$$

The non-dimensional parameters C_P and C_T of a wind turbine vary with the incident wind speed as well as the rotational speed of the turbine, which are included in the tip speed ratio λ. This makes it possible to express the performance of a wind turbine in characteristic curves. Typical performance curves for power and thrust of a modern wind turbine are shown in *Fig. 1.2*.

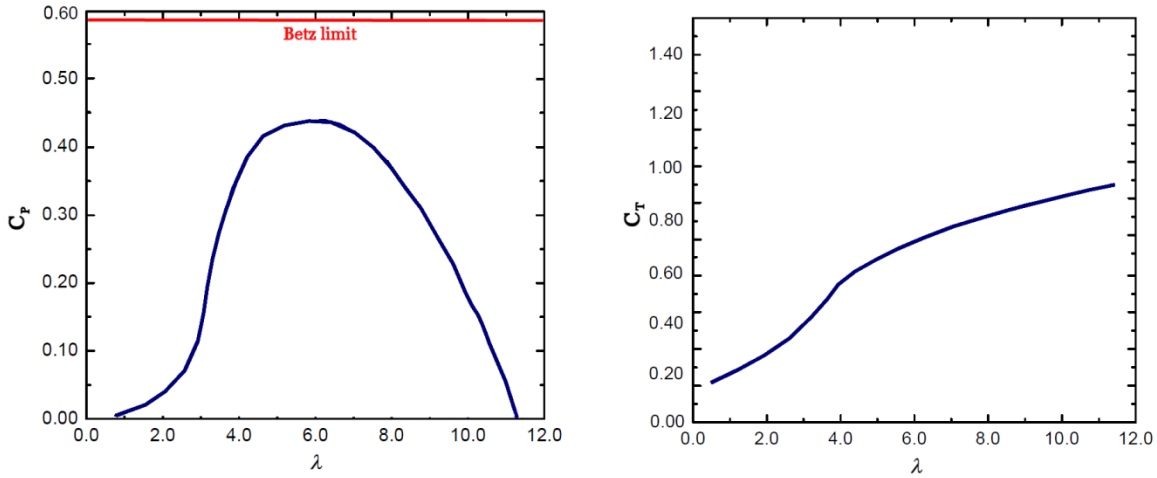

Fig. 1.2: *Typical C_P-λ and C_T–λ curves of a modern wind turbine*

The power coefficient C_P features a distinct maximum at a certain tip speed ratio λ for which ideal flow conditions predominate in every section of the turbine blade profile. This point is usually the design operating point of the wind turbine. Modern wind turbines usually reach a maximum C_P value of around 0.45 to 0.50 [13] which is significantly below the Betz limit. Firstly, no blade design is aerodynamically perfect so that there are always losses due to drag. There always will be aerodynamic losses at the blade tips and blade roots for any blade design [11]. Additionally, friction losses in the bearings and gearbox have to be taken into account. At lower than design tip speed ratios a negative angle of attack at the inner section of the blade (close to the blade root) causes stall. This is often referred to as the "stall region" in which considerable power losses occur [14]. At higher than design tip speed ratios highly positive angles of attack cause a considerable amount of drag on the blades which is responsible for a significant decrease in the power coefficient with increasing tip speed ratios [11]. In this region, the flow separates from the blade profiles. When the turbine does not extract any more energy from the wind, the C_P value consequently goes down to zero again. The inner part of the rotor aerodynamically acts as a propeller, which actually adds energy to the fluid. Only the outer part of the rotor performs as a turbine and still extracts energy from the wind flow. When the amount of energy added to the flow and extracted from the flow are in balance, this is called the "run-away" point of the wind turbine. In case the wind turbine would not be connected to an electrical generator, the turbine would rotate at the tip speed ratio λ at the run-away point. The thrust coefficient C_T of a wind turbine is of great importance for the construction of the rotor support and the structural design of the turbine tower [11]. It continuously grows with increasing tip speed ratio. The blockage effect of the rotor rises with increasing rotational speeds and thus causes higher thrust forces onto the turbine. In the transition from the stall region to the optimum tip speed often a slight buckling of the curve can be observed as the blades are not operated in stalled conditions any more.

1.2.2 Blade Aerodynamics

The blades of a wind turbine are designed with the goal to extract as much energy from the wind as possible. Dependent on the wind speed at the turbine site and a variable or constant rotational speed operation of the turbine, a specific blade design is developed. Most turbine blades are designed according to the blade element method wherein the blades are cut into infinitesimally small span-wise blade elements. On every blade elements the two-dimensional cross section is adjusted so that the angle of attack and the aerodynamic forces are optimized.

During the operation of a wind turbine many situations occur where the flow locally does not hit the blades at the designed angle of attack. This can be caused by the highly stochastic wind field hitting the rotor as well as to slow or to high rotational speeds of the rotor, which can lead to stall at a certain section of the blade. The development of stall at a span-wise blade element is depicted in *Fig. 1.3*.

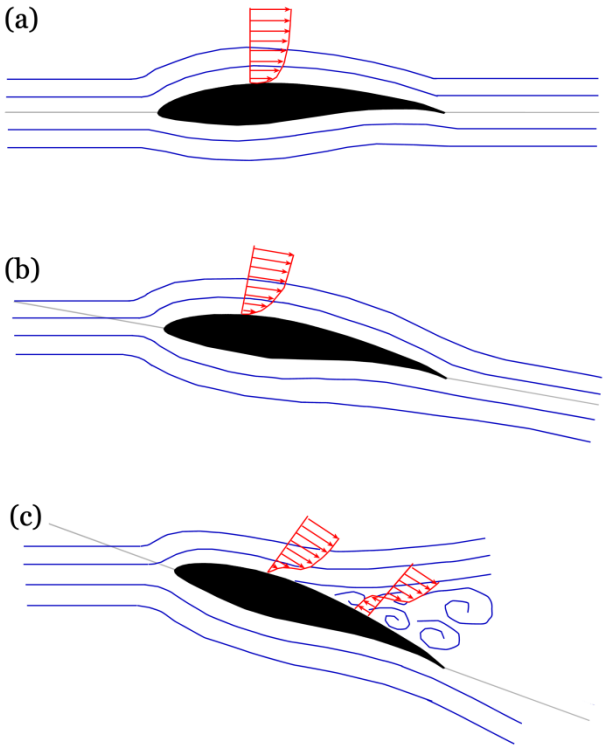

Fig. 1.3: *Stream lines around wind turbine blades at different angles of attack*

Fig. 1.3 (a) shows a wind turbine blade profile hit by the incoming relative flow at the design angle of attack. The flow adheres and follows the blade profile perfectly. When the relative angle of attack is increased as shown in *Fig. 1.3* (b) it is still possible that the flow

adheres and follows the profile. Exceeding the critical angle of attack, a certain limit dependent on the blade profile itself, however, the flow cannot follow the blades contour anymore and highly turbulent recirculation zones appear near the blade surface as shown in *Fig 1.3* (c). So-called stalled conditions are dominant in this section of the blade resulting in substantial aerodynamic losses.
The span-wise position on the blade, the operating conditions of the turbine and the composition of the incoming wind to the rotor have a considerable influence on the flow exiting from the turbine rotor. The flow behind the turbine rotor is called wake and it is characterized by very turbulent flow. The flow field in the wake behind the rotor is influenced by a number of aerodynamic effects.

1.2.3 Wake Aerodynamics

The aerodynamic conditions prevailing in the wake of a wind turbine have been one of the main topics of research since the beginning of wind turbine research. As mentioned above stall is an essential phenomenon during the operation of a wind turbine which together with non-uniform transient inflow defines the general aerodynamic conditions prevailing in the wake of a wind turbine. Although a modern rotor of a horizontal axis wind turbine only consists of three rotating blades, many aerodynamic effects combine to a very complex flow field in the wake. In a comprehensive literature study about wind turbine wakes from 2003, Vermeer et al. conclude that “some of the most basic aerodynamic mechanisms governing the power output are not yet fully understood” [10].
The main features of the turbine wake are a considerable velocity deficit and increased turbulence levels. The velocity deficit yields a significantly lower power extraction of the downstream wind turbines in a wind farm arrangement. The increased turbulence levels in the wake can involve bigger fatigue loads on the downstream turbines [14].
The aerodynamic structures of the flow field in the wake of a wind turbine rotor depend on many different parameters. The aerodynamics of the incoming flow, the aerodynamic design of the blade as well as the rotational speed of the rotor itself have an influence on which sections of the blades stall occurs or not. However, there are some basic aerodynamic phenomena which are predominant in almost every wind turbine rotor.

One of the most important aerodynamic phenomena is the rotation of the flow field in the wake of a wind turbine rotor. The velocity triangles in front of (Index 1) and behind (Index 2) a cross section of a wind turbine blade are sketched in *Fig. 1.4*.

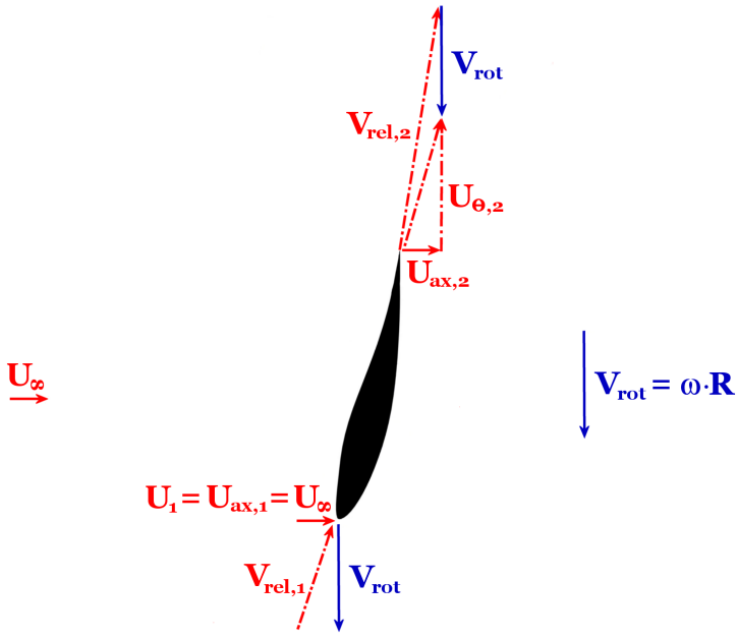

Fig. 1.4: *Velocity triangle on a wind turbine blade*

Under idealized conditions there is a purely axial inflow (1) $U_1 = U_{ax,1} = U_\infty$ to the wind turbine rotor. In the flow field downstream of the rotor (2), however, the absolute flow velocity features a velocity component in circumferential direction $U_{\theta,2}$ creating a rotation of the flow in the wake behind the rotor. As it can be seen in *Fig 1.4,* the circumferential component $U_{\theta,2}$ causes the wake to counter-rotate in respect to the direction of rotation of the turbine rotor V_{rot}. Manwell et al. rationalize that the "flow behind the rotor rotates in the opposite direction to the rotor, in reaction to the torque exerted by the flow on the rotor" [3].

However, also a number of other aerodynamic phenomena have to be taken into account when investigating the turbulent structures in the wake. Another dominating phenomenon is the formation of the tip vortex which leads to a shear layer that separates the highly turbulent flow in the rotor wake from the surrounding ambient flow. Wind turbine blades have a profile that creates aerodynamic lift similar to the profile of an airplane wing. The air around a blade profile is accelerated that a pressure side (PS) and a

suction side (SS) are established. The pressure difference between the PS and the SS generates the aerodynamic lift and thereby sets the blades into rotation.

On the tip of the blade a three-dimensional secondary flow establishes. In order to decrease the pressure difference between the high pressure air on the pressure side flows around the blade tip to the lower pressure on the suction side as shown in *Fig. 1.5*. This secondary flow around the tip mixes with the main flow around the blade which creates a vortex behind the blade tip.

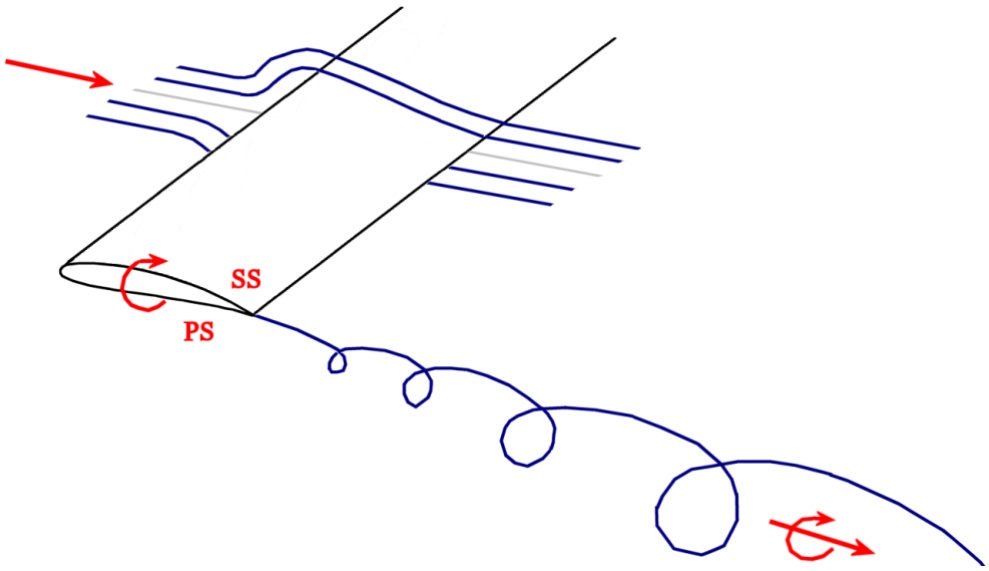

Fig. 1.5: *Formation of the tip vortex*

A similar observation can be made at the wingtips of airplanes where the tip vortex phenomenon considerably reduces the effective area of the wing that creates lift. The tip vortex is characterized by high velocities and low pressures and induces additional aerodynamic losses. This can be attributed to the fact that the effective angle of attack is reduced in regions close to the tip as some air is sucked sideways through the pressure gradient at the tip [15].

On most wind turbine blade designs there is also a sharp edge near the root of the blade. Also around the root edge a secondary flow establishes due to the pressure gradient between the blade's pressure and suction side. When mixing with the main flow the root vortex is generated in the same way as described above. However, the aerodynamic losses caused by the root vortex are assumed to be considerably lower than those by the tip vortex as the relative velocities are significantly lower near the root [16].

The tip vortices shed by the turbine blades move further downstream in helical spirals. As the speed of the blade tips $U_{tip} = \omega R_{tip}$ usually is much higher than the incoming wind speed U_∞, the distance between the tip vortex spirals is very low. Therefore, the vortex system can be approximated as a very turbulent cylindrical shear layer [17]. A schematic sketch of the tip vortices forming a cylindrical shear layer is presented in *Fig. 1.7*.

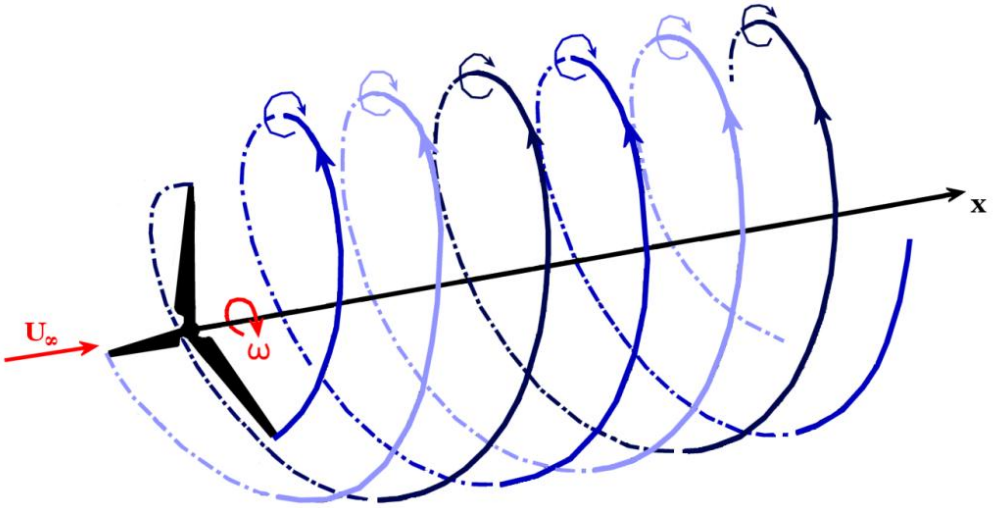

Fig. 1.6: *Cylindrical shear layer in the wake of the rotor induced by tip vortices*

The low velocity turbulent flow in the wake is separated from the surrounding faster moving laminar flow by this shear layer. Moreover, the considerably weaker root vortices create a turbulent swirl in the region around the rotor axis, which is however of significantly weaker intensity.

It has been shown that the aerodynamics in the wake behind a wind turbine rotor is characterized by a complex vortex system, which is influenced by a number of different phenomena: the structures in the incoming wind flow, the swirl generated by the rotation of the blades, the root vortices and the shear layer created by the tip vortices. Additionally, the geometry of the wind turbine tower and nacelle affect the turbulent structures prevailing in the wake.

The distinct tip and root vortices destabilize when moving downstream. The small-scale turbulence of the vortices brakes down into large-scale turbulence due to turbulent mixing processes [18]. *Fig. 1.8* shows a model of the turbulent mixing process in the wake behind the rotor and the corresponding velocity profiles.

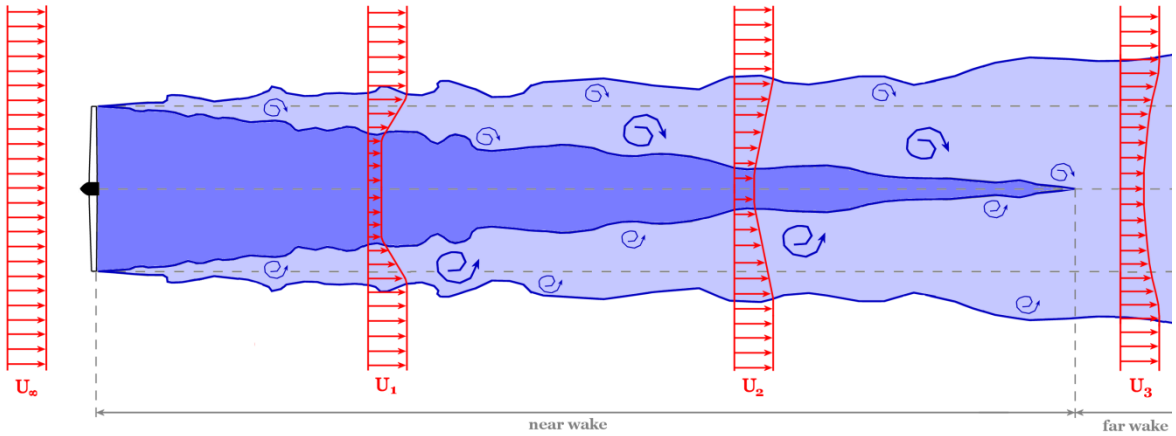

Fig. 1.7: *Turbulent mixing process in the wake behind a wind turbine rotor*

Moving further downstream, the cylindrical shear layer expands due to turbulent diffusion. The turbulence in the shear layer mixes the slow moving fluid in the wake with high velocity fluid surrounding it. Thus, momentum is transported into the wake, which results in a wake expansion but reduction in velocity deficit [19]. The mean velocity gradually recovers and the velocity profiles smoothen when moving downstream in the wake as shown in *Fig. 1.8*. At a certain downstream distance the shear layer reaches the center of the wakes indicating the end of the "near wake" region. After a "transition region" the wake is completely developed, which is thus called the "far wake region" [17].

The root vortices and tip vortices are predominant in the near wake regions. The number of blades, adherent or stalled flow and three-dimensional flow have a large influence on the flow in this region [10]. In the far wake region, however, the focus is no longer on the flow phenomena around the rotor blades. The single turbulence generating phenomena have mixed into a general turbulence distribution, which dominates the flow [18]. When modeling an entire wind farm, far wake simulation is the main focus [10].

When defining the downstream distance x/D, where the near wake ends, different values can be found in the literature. Vermeer et al. [10] as well as Sanderse [19] define the near wake to be over at around x/D=1, whereas Gómez-Elivra et al. [17] claim that the near wake ends somewhere between x/D= 2-5 rotor diameters.

1.3 Wind Farm Arrangement

During the last decades strong efforts have been made to increase the efficiency of wind turbines in order to extract as much energy as possible from the wind. The research focused on optimizing the single components of a turbine. Gearless wind turbines were introduced and another main focus was the aerodynamic optimization of the turbine blades.

When it comes to optimizing a whole wind farm as one single power production device, also the aerodynamic interactions between the single turbines of the wind farm have to be taken into account. As the first row wind turbines extract a considerable amount of the kinetic energy in the wind there is much less energy left for the turbines in the following rows. The distance between the single turbines, the arrangement pattern and the amount of power extracted from the wind by the single turbines are some of the most important parameters when designing a wind farm.

Fig. 1.8: *Wind turbine wake effects in the Danish offshore wind farm "Horns Rev 1" [20]*

Fig. 1.9 shows the turbulent flow field in the Danish offshore wind farm "Horns Rev 1". At the time the picture was taken the air in the rotor plane of the turbines was very humid. The rotating wind turbine blades locally induced condensation of the humid air making it possible to see the turbulent flow structures in the wake of the wind turbines [20]. It can

be clearly seen that the turbulent flow in the wake of the first row turbines hits and interacts with the following turbine rows.

There are two main effects of wake interaction in a wind farm arrangement. Obviously, the velocity deficit in the wake of the first turbine yields a significantly lower power extraction of the following downstream wind turbines. Furthermore, the increased turbulence levels in the wake of the first row turbines cause higher fatigue loads for the downstream turbines [10].

In order to investigate the aerodynamic properties prevailing in a wind turbine wake CFD computer simulations and wind tunnel experiments on model wind turbines are nowadays performed. Full scale measurements on wind turbine wakes are by far too expensive or simply not possible.

In a CFD simulation Ivanell et al. [21] investigated the propagation of the wake through an array of two wind turbines. In this Large Eddy Simulation (LES) study the Actuator Disc Method (ACD) was used for modelling the wind turbines. Appling the 3D solver "EllipSys3D" and multi block finite volume grid, the first turbine was impinged with a pre-generated turbulence. *Fig. 1.10* shows a 2D plot of the velocity deficit in the wake propagating through three turbine rows at a zero degree inflow angle.

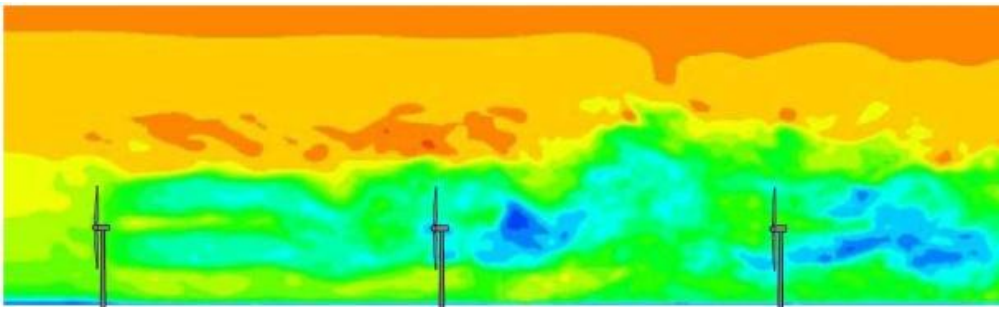

Fig. 1.9: *CFD simulation of the propagation of wind turbine wake in a wind farm arrangement [21]*

From this simulation Ivanell et al. [21] conclude that turbulent inflow to the first row turbines leads to a complex but realistic flow structure in the wake. They state, however, that this study does not give any correlation between the turbulence intensity of the inflow and the level of production yet. In order to be able to find a correlation further investigations would have to be made including real wind farm measurement data for verification.

When designing a wind farm an economic compromise for the separation distance of the single wind turbines has to be found. On the one hand space in a wind farm is not unlimited; on the other hand the losses in energy extraction due to wake interactions are quite considerable. In modern wind farms, such as the Horns Rev 1 from 2002, the single wind turbines are set up with a separation distance of around 7 rotor diameters (7D) [22]. In a recent study, however, Barber et al. [23] recommend that the spacing between the single turbines should be increased to 12-15D in order to optimize the overall power output. According to Barthelmie et al. [24] the average power losses that can be ascribed to wind turbine wakes range in the order of 10-20% compared to a wind farm of unobstructed turbines.

The effect of increased fatigue loads on the downstream turbine due to turbulent flow in the wake was measured to be 80% in a real wind farm in Vindeby, Denmark [19]. As a consequence the blades of the downstream turbines are predicted to have a considerably shorter lifetime. Nevertheless, the difference in fatigue loads on turbines operating in the wakes of multiple upstream turbines was found to be small [19].

In fact the arrangement of the single turbines in a wind farm in order to maximize the overall power output is a very complex problem. In a study from 2007 Marmidis et al. [25] applied the mathematical “Monte Carlo” method to simulate the maximum energy production versus the minimum installation costs of different placement patterns of the turbines in a wind farm.

When optimizing a wind farm with respect to the overall maximum power output, not only the separation distance and the placement pattern, but also the operation points of the single turbines are of importance. By extracting a lower amount of energy from wind by the upstream wind turbine more kinetic wind energy is left for the downstream turbine. This reduction in the so-called axial induction factor can be achieved by controlling the blade pitch angle or the tip speed ratio of the upstream turbine. An investigation by Johnson and Thomas [26] has shown that an operation of the first turbine slightly below its maximum power point considerably increases the power output of the downstream turbine and thereby increases the overall output of the two turbine setup. This implies that the total power output of wind farm might be enhanced by actively controlling pitch angle, yaw angle and tip speed ratio of the single wind turbines.

1.4 Motivation

One of the main goals in modern wind farm design is to reduce the interaction between the single wind turbines. However, the disposable space for a wind farm is not unlimited which results unavoidably in interactions of the wind turbine wakes for certain wind directions. In a wind farm the wakes of the first row turbines cause a non-uniform flow field, which hits the second row turbines.

The wake of a horizontal-axis wind turbine can be characterized by turbulent flow structures in rotational motion. A substantial velocity deficit and high turbulence intensities are the main features in the wake of a wind turbine. The velocity deficit is equal to a loss of kinetic energy in the wake, which constitutes a loss of power available for the downstream turbines. Increased turbulence levels may affect the dynamic loads onto the rotor blades of the downwind turbines. Furthermore, it could be possible that the swirling motion exiting from a wind turbine rotor could excite an eigenfrequency of the blades of the downstream turbine and thereby cause material fatigue.

Investigating the influence of the wake of the upstream turbine onto the performance and dynamic behavior of the downstream turbine the next logical step is to examine the wake behind the downstream turbine. A number of numerical models have been and are being developed which require comprehensive experimental data for validation. Wind tunnel simulations under controlled conditions are a powerful means to achieve this.

Moreover, this experimental study of the wake behind an array of two model wind turbines shall contribute to a comprehensive understanding of the turbulent flow structures in wind turbine wakes, which could be helpful in the planning and design of future wind farms.

2 OBJECTIVES

The main focus of performing the measurements in the wind tunnel laboratory at NTNU is to get a picture of the flow conditions, i.e. the local velocity deficit and the turbulence intensities, in the wake behind an array of two model wind turbines. This study shall help to get an extensive knowledge of the complex flow field in wind turbine wakes and act as an experimental database for the validation of numerical models. It is desirable that this experimental study can contribute to yield data that can be used in the design of future wind farms.

The objectives of the present work are the experimental investigation of

- the influence of the wake of the first turbine onto performance of the downstream turbine at different turbine separation distances
- the axial development of the local velocity deficit and turbulence intensities in the wake downstream of the second turbine
- the axial development of the dimensions of the wake
- the influence on the velocity deficit and turbulence intensities when the distance between the turbine is increased
- the effect of different tip speed ratio combinations of the first and second turbine onto the flow field in the wake behind the second turbine

3 METHODOLOGY

This experimental investigation is performed in the wind tunnel at NTNU's Department of Energy and Process Technology. The closed-return wind tunnel is equipped with one force balance which makes it possible to measure the thrust force onto one of the two model wind turbines.

Two fully operational three-bladed model wind turbines with a rotor diameter of about $D_{rot} = 0.9m$ are available. Both turbines are equipped with torque sensors on their rotor shafts and optical RPM-sensors inside the hub casing. It is thereby possible to measure the power the turbine extracts from the wind directly.

Inside the wind tunnel there is a three-axis traverse system installed, which can be controlled by a LabVIEW computer program. This traverse system allows scanning the flow field in the wake of the wind turbine arrangement automatically. To do this, a parallel setup of a Pitot tube and a hot wire probe is used. The hot wire signal is calibrated against the signal acquired from the parallel Pitot tube, which itself is calibrated against a manual Lambrecht manometer. The hot wire probe is connected to a Constant Temperature Anemometry (CTA) circuit. The output signal yields a velocity signal with very high frequency resolution which then can be recalculated into a mean velocity and turbulence intensity.

A National Instruments BNC-2110 data acquisition board and an in-house designed LabVIEW routine are used to record the acquired data on the computer.

For the post-processing of the recorded data an in-house programmed FORTRAN routine temperature-corrects the data acquired from the hot wire and converts it to mean velocity and turbulence intensity values. Finally, meaningful plots are created using the software MATLAB for the evaluation of the measured flow parameters.

4 EXPERIMENTAL SETUP

4.1 Test Rig

4.1.1 Closed-Return Wind Tunnel

This experimental study is performed in the large wind tunnel at the Department of Energy and Process Technology at NTNU. The driving fan has a maximum power of $P = 220kW$ which makes it possible to generate wind speeds up to $U_\infty = 30\ m/s$ in the test section of the wind tunnel. The air flow enters the test section through an inlet contraction which is equipped with static pressure holes at the circumferences of two defined cross sections. In *chapter 4.2.3* it is explained how these pressure holes are used to calculate the inlet speed of the wind tunnel.

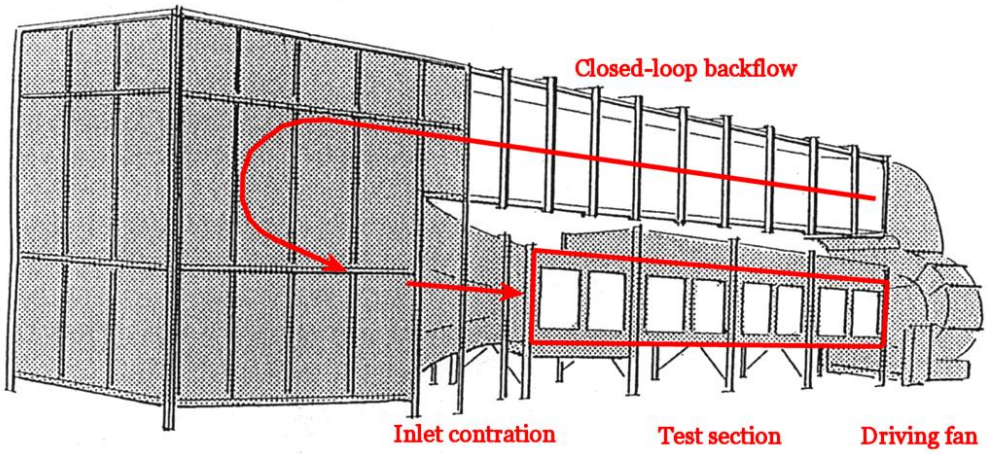

Fig. 4.1: *Wind tunnel at the Fluid Engineering laboratory at NTNU [27]*

As shown in *Fig. 4.1* the airflow then enters the $x = 12.0\ m$ long test section of the wind tunnel. It has a cross section of $y = 1.9\ m$ height and $z = 2.7\ m$ width. The roof of the tunnel is adjusted so that a zero static pressure gradient is present in flow direction over the entire test section [14]. After passing through the driving fan, the air flows back to the inlet contraction in a closed loop tunnel above the test section.

4.1.2 Model Wind Turbines

In NTNU's wind tunnel laboratory two fully operational model wind turbines are available. Both model wind turbines were originally designed as prototypes for tidal turbines by the Norwegian company Hammerfest Strøm AS. The turbines are now equipped with new wind-optimized blades which are described in *chapter 4.1.3* in detail. *Fig. 4.2* shows a picture of the first experimental setup with both model wind turbines established in NTNU's wind tunnel.

Fig. 4.2: *The two model wind turbines set up in the wind tunnel of NTNU*

The first model wind turbine (Tu1) is mounted on a 6-component force balance, which is located underneath the test section of the wind tunnel. The force balance makes it possible to measure the thrust force onto the turbine and is more thoroughly described in *chapter 4.2.9*. The second model wind turbine (Tu2) is fixed on the wind tunnel floor through a wooden plate. The rotors of both model turbines are driven by a 0.37 kW AC electric motor produced by Siemens [28]. The motor is located at the level of the wind tunnel floor and drives the rotor axis through a belt, which runs inside the turbine mast for the first turbine respectively behind the turbine mast for the second turbine. The rotational speed both turbine rotors is controlled by a Siemens Micromaster 440 frequency inverter from

outside of the wind tunnel. The motors can be impinged with a wide range of rotational speeds and similarly work as generators when the turbine rotors are subject to an external wind load. The inverters are connected to a standard electrical heater which acts as an electrical resistance for the excess power produced by the turbine rotors in this case.

Fig. 4.3 shows a sketch of the basic experimental setup in the wind tunnel. The separation distance x/D between the two model turbines can be varied. The dashed red lines refer to the axial downstream measurement locations where the aerodynamic probes are traversed in order to record the flow field in the wake of the turbines. An overview of the most important dimensions is presented in *Table 4.1*.

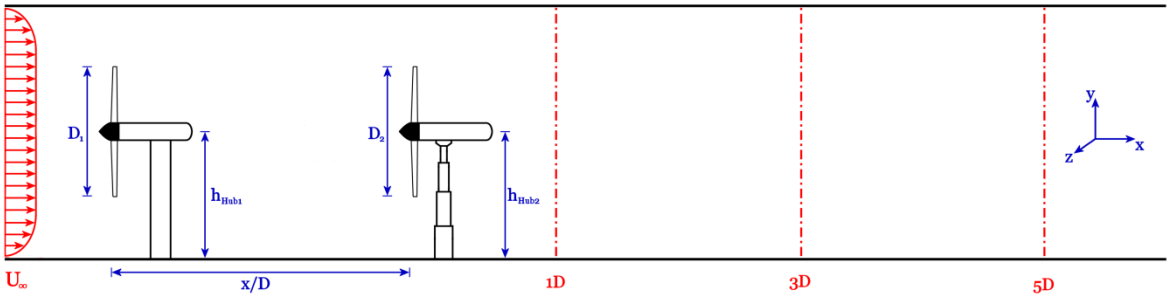

Fig. 4.3: *Experimental setup and reference orientation*

Rotor diameter Tu1	D_1	940 mm
Rotor diameter Tu2	D_2	900 mm
Hub diameter Tu1	d_{hub1}	130 mm
Hub diameter Tu1	d_{hub2}	90 mm
Hub height Tu1	h_{hub1}	950 mm
Hub height Tu2	h_{hub2}	950 mm
Separation distance between the turbines	x/D_1	3 resp. 5
Wind tunnel height	h	2000 mm
Wind tunnel width	w	2700 mm
Wind tunnel length	l	12000 mm

Table 4.1: *Dimensions of the experimental setup*

In comparison to a real wind turbine, the rotor dimension of the model turbines are in the scale of about 1: 100. With a hub diameter of $d_{hub,1} = 130\ mm$ respectively $d_{hub,2} = 90\ mm$ the dimensions of the nacelle are much bigger in respect to the rotor diameter than in a real turbine. This has to be taken into account when analyzing and comparing the structure of the wake behind the turbine.

The first model wind turbine which is mounted on the force balance is additionally supported by four wooden blocks in order to achieve the same hub height as the second turbine. Both turbines are positioned centrally in the wind tunnel having an equal distance to both wind tunnel side walls. Paying to the fact that both turbines are equipped with the exactly same blades but the hub diameter of the first turbine is slightly bigger, the rotor diameter of the first turbine exceeds that of the second turbine insignificantly.

4.1.3 Turbine Blades

As mentioned above both model wind turbines are equipped with the same blades. Standard NREL airfoils of the type S826 with a 14% thickness are used. The chord length distribution and the twist of the rotor blade are designed according to a standard blade element momentum method [29].
Fig. 4.4 shows a view onto the model blade in streamwise and circumferential projection.

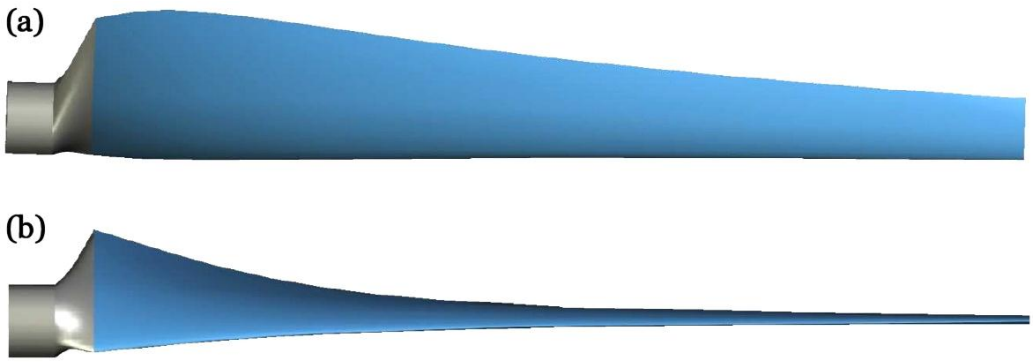

Fig. 4.4: *View on blade in (a) streamwise and (b) circumferential projection [29]*

The profile which features a separation ramp at the back is designed for a Reynolds number of $Re = \frac{\omega R c}{v} = 2\ x\ 10^6$ to give maximum lift [29]. According to Krogstad and Lund the blade geometry can be characterized by a "gentle separation due to trailing edge ramp", a "rapid transition on suction side due to small radius of curvature", a "low sensitivity to surface roughness" and a "strong separation on lower side at negative angle of attack" [29]. A cross section of the NREL S826 profile is shown in *Fig. 4.5*. Further information on the profile can be found in the document [30].

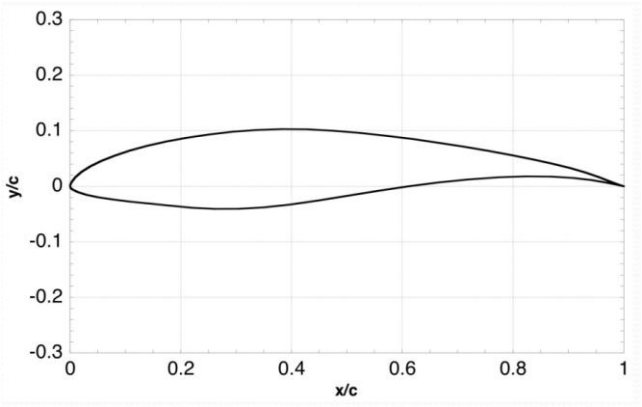

Fig. 4.5: *Scaled blade profile NREL S826 14% thickness [30]*

A comprehensive investigation of the blade geometry mounted on the Department's second model wind turbine (Tu2) was performed by Karlsen [16] as well as Krogstad and Lund [29] applying experimental and computational methods.

4.1.4 Traverse Mechanism

The test section at NTNU's wind tunnel is equipped with an automatic computer-controlled traverse mechanism as sketched in *Fig. 4.6*. The traverse system is fixed on rails right underneath the roof of the wind tunnel. It is possible to bring the traverse mechanism into the right streamwise position by moving it manually on the rails.

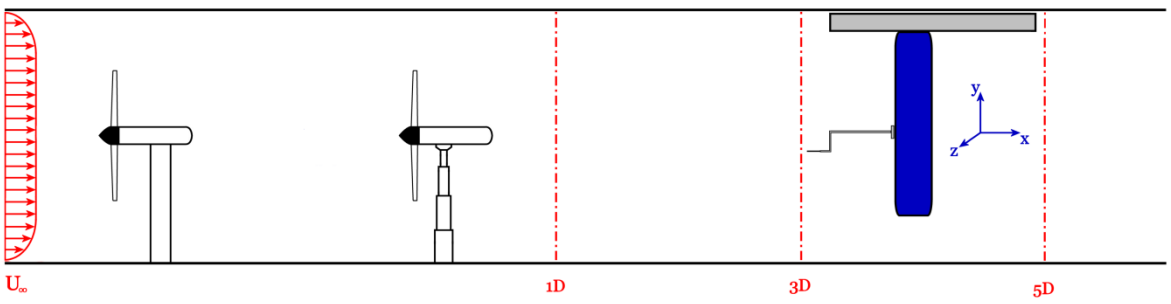

Fig. 4.6: *Automatic traverse system installed in NTNU's wind tunnel*

With an aerodynamic probe connected to it, the traverse system allows automatic flow measurements at almost any position in the wind tunnel. The position of the probe can be controlled by a computer in all three dimensions using in-house designed LabVIEW software.

4.2 Instruments

4.2.1 Barometer

The ambient pressure is acquired through a mercury barometer produced by Lambrecht. It is manually read from a mercury column in the unit [mm Hg]. If needed, the pressure can be recalculated into [Pa] using the formula

$$p\,[Pa] = \frac{101325}{760} \cdot h\,[mmHg] \qquad (4.1)$$

4.2.2 Inlet nozzle

Before the air flow enters the test section of the wind tunnel, it passes through an inlet contraction, which is simultaneously used as a nozzle that measures the inlet velocity. In this contraction there are pressure holes around the entire circumference at two defined axial stations as schematically shown in *Fig. 4.7*. By measuring the pressures p_1 and p_2 at these defined circumferences and knowing the areas A_1 and A_2, it is possible to calculate the velocity U_2 at the outlet of the contraction. This velocity is equal to the inlet velocity to the test section $U_{\infty,contraction}$ of the wind tunnel.

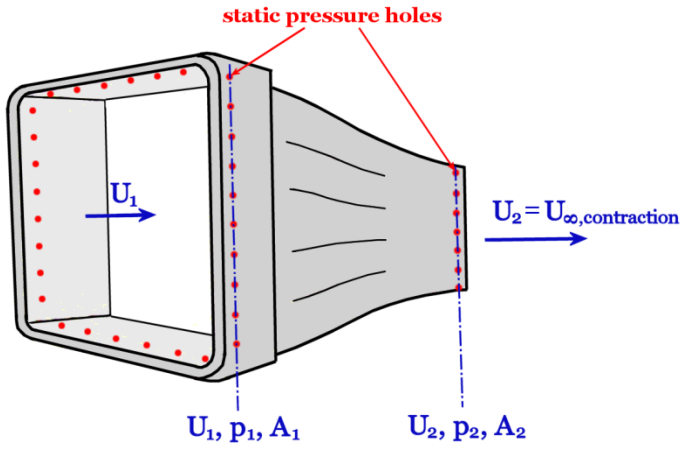

Fig. 4.7: *Schematic sketch of the inlet contraction*

Applying the continuity equation the inlet velocity can be calculated from

$$U_{\infty,contraction} = \sqrt{\frac{2(p_1 - p_2)}{\rho\left(1 - \frac{A_2^2}{A_1^2}\right)}} \qquad (4.2)$$

In the present wind tunnel the area ratio square is

$$\frac{{A_1}^2}{{A_2}^2} = 4.36 \tag{4.3}$$

4.2.3 Reference Pitot tube

In order to be able to double check the velocity at the wind tunnel inlet a Pitot tube is installed at a height of about 300 mm above the wind tunnel floor and a distance of about 400 mm from the right wind tunnel wall.
It is possible to calculate the velocity $U_{\infty,pitot}$ from the pressure difference given by the Pitot tube.

$$U_{\infty,pitot} = \sqrt{\frac{2(p_{tot} - p_{stat})}{\rho}} \tag{4.4}$$

In contrast to the inlet speed acquired at the inlet contraction $U_{\infty,contraction}$, the velocity $U_{\infty,pitot}$ is only acquired in one defined position at the wind tunnel inlet.

4.2.4 Thermocouple

For acquiring the temperature in the wind tunnel a thermocouple is placed at the right wind tunnel wall. The voltage from the thermocouple is converted into a signal on a National Instruments NI 9211 thermocouple board and sent to the computer. The temperature in the wind tunnel is used to calculate the air density and for the temperature correction of the hot wire signal during the post-processing of the acquired data.

4.2.5 Traverse Pitot tube

The flow field in the wake behind the model turbines is traversed using another Pitot probe and a hot wire probe in a parallel setup as depicted in *Fig. 4.8*.

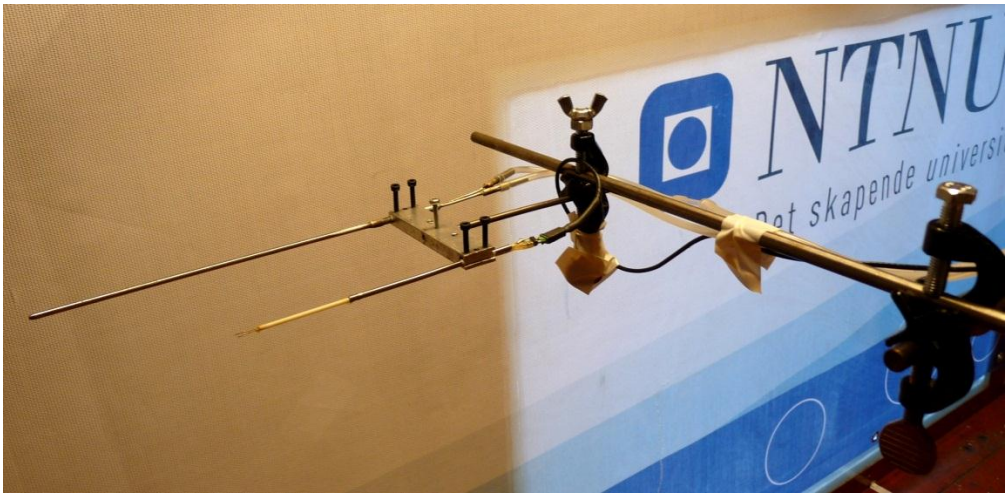

Fig. 4.8: *Parallel probe setup*

The velocity U_{Pitot} is again calculated from the pressure difference of the total and the static pressure measured with the Pitot tube.

$$U_{pitot} = \sqrt{\frac{2(p_{tot} - p_{stat})}{\rho}} \tag{4.5}$$

The hotwire probe has a much higher frequency response than a Pitot tube and therefore is much more appropriate for measurements in turbulent flow. The Pitot tube fixed right next to the hot wire probe is however essential for the calibration of the hot wire probe. It also can be used to double-check the velocity values acquired by the hot wire probe.

4.2.6 Hot wire probe

The main instrument for acquiring the velocity field in the wake behind the model turbines is a hot wire probe connected to a constant temperature anemometry (CTA) circuit. The probe head of a hot wire probe consists of a very thin tungsten wire in the range of μm in diameter connected to two prongs [31]. The resistance of the wire changes

with the wire Temperature T_W, which itself is a function of the flow velocity U because of the convective heat transfer $\dot{Q}$ from the wire.

Hot wire anemometry is an appropriate technique to measure velocity fluctuations in turbulent flow. Hot wires feature a high time resolution, which makes it possible to record fluctuations up to several hundred kHz [32]. For all measurements performed in the scope of this project a non-commercial in-house prepared single-wire probe is applied. A frequency response test performed according to Jørgensen [32] yielded a system bandwidth of $f_c = 21\ kHz$. A basic sketch of a hot wire probe is presented in *Fig. 4.9*.

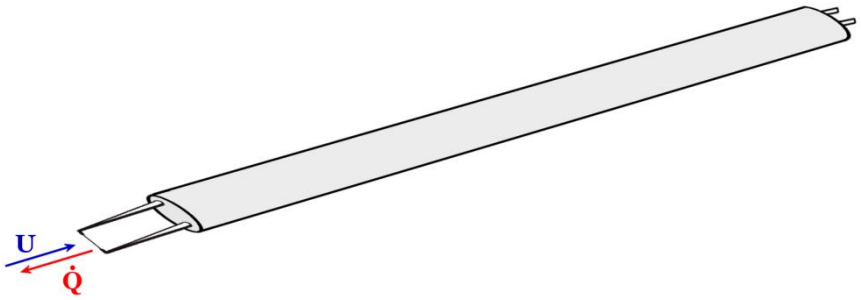

Fig. 4.9: *Hot wire probe*

The hot wire probe is connected to a CTA circuit which contains a Wheatstone bridge as depicted in *Fig. 4.10*. Therein, the probe is connected to one arm of the bridge and supplied with electrical current at exactly the same rate as heat is lost to the surrounding flow [32]. The variable resistor R_3 defines the operating resistance and the operating temperature of the hot wire. The bridge is balanced by a servo amplifier G, which keeps the wire resistance R_W constant. Thus, also the wire temperature remains constant independently of heat transfer rate to the surrounding fluid.

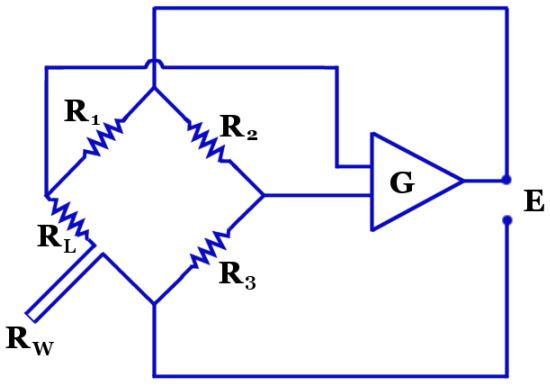

Fig. 4.10: *CTA circuit containing a Wheatstone bridge*

If the bridge is in balance there is no voltage difference E over the bridge. In case of an increase in flow velocity the wire resistance decreases. Thus, there will be a voltage difference at the input of the current regulating amplifier G, which then increases the current supplied to the hot wire. Accordingly, the wire resistance R_W increases until the Wheatstone bridge is balanced again. Therefore, the bridge voltage E is dependent on the convective heat transfer to the surrounding fluid [31].
A comprehensive and very useful practical guide for hot wire anemometry is written by Jørgensen [32].

4.2.7 RPM sensor

Moreover, the two model wind turbines are equipped with optical RPM sensors inside the hub casing. A metal disc with a small gap in one position is fixed to the rotor axis inside the casing. When the gap is passing the optical sensor, it gives a signal.
Fig. 4.11 shows the position of the optical rpm sensor inside the hub casing of the second turbine.

4.2.8 Torque transducer

Both model wind turbines are equipped with torque transducers connected to the rotor shaft. The location of the torque sensor inside the second model wind turbine (Tu2) is shown in *Fig. 4.11*.

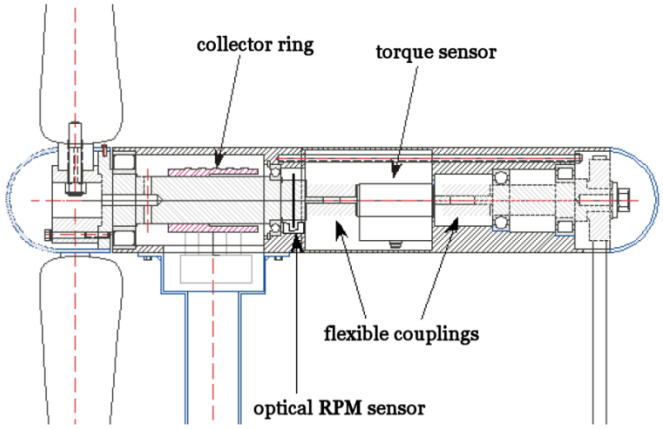

Fig. 4.11: *Cross section of the hub of the second turbine [27]*

A torque transducer of the type T20W N/2 Nm sold by HBM is installed. After being calibrated, the torque transducers make it possible to obtain the torque by the wind onto the turbine rotor.

4.2.9 Force balance

The wind tunnel at NTNU is equipped with a six-component force balance produced by Carl Schenck AG, which makes it possible to acquire the thrust force from the wind onto the turbine mounted on it. However, just one turbine can be fixed on the balance. It is possible to rotate the force balance 360° which could be useful for wake measurements in yawed conditions.

4.3 Instrument calibrations

4.3.1 Pressure transducer calibration

Before starting with the actual velocity measurements the three pressure transducers connected to Inlet Contraction pressure holes, the Reference Pitot tube and the Traverse Pitot tube have to be calibrated. The pressure transducers convert a pressure difference [Pa] into an electrical signal [Volt].

For the calibration procedure the pressure transducers are connected in parallel to a manual Lambrecht manometer. Thereafter, the wind tunnel speed is increased in defined steps yielding an increase in the alcohol column of the Lambrecht manometer and an electrical signal from the pressure transducer.

Fig. 4.12 shows an example of a calibration curve for one of the pressure transducers.

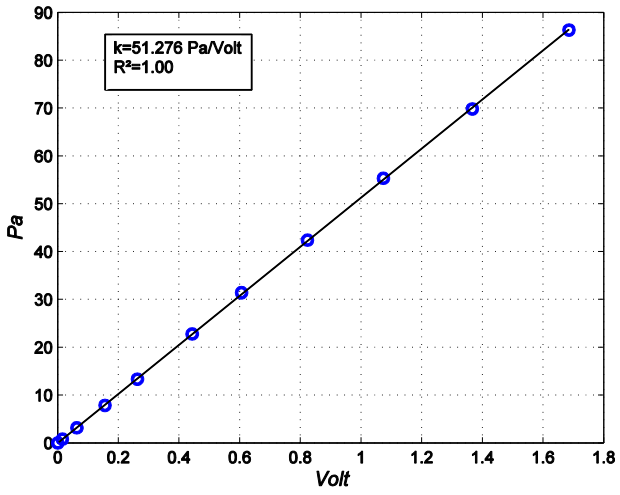

Fig. 4.12: *Calibration curve of a pressure transducer*

Knowing the density of the methylated alcohol, the alcohol column at the Lambrecht manometer can be recalculated into a pressure difference in [Pa]. Plotting the pressure difference in [Pa] versus the electrical signal in [Volt] a linear dependency can be derived. By fitting a straight line to the measured values the calibration coefficient k in [Pa/Volt] can be found.

4.3.2 Hot wire calibration

As explained in *chapter 4.2.6* the electrical signal at the output of the CTA circuit is the bridge voltage E [Volt]. This signal is calibrated versus the velocity U_{Pitot} [m/s] acquired from the Traverse Pitot tube, which is positioned right next to the hot wire probe (*Fig. 4.8*). As shown in an exemplary calibration curve in *Fig. 4.13* the dependency of the velocity on the hot wire voltage is not linear.

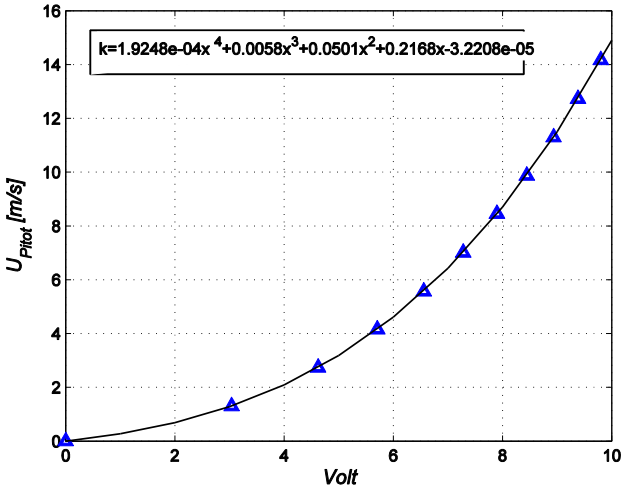

Fig. 4.13: *Calibration curve for the hot wire probe signal*

A higher grad polynomial fit must be applied in order to create a calibration curve. For this project a fourth grade polynomial fit function is applied yielding five calibration coefficients.

4.3.3 Torque sensor calibration

Moreover, the torque sensors connected to the turbine shafts have to be calibrated. This is done by blocking the rear part of the rotor shaft and creating a defined torque on the frontal part of the shaft. Step by step defined weights are put onto a hanging device, which is connected to a rotor blade in a certain distance. The torque sensor is subjected to defined values of torque in [Nm] simultaneously yielding an electrical signal in [Volt]. A linear dependency between the torque [Nm] and the signal [Volt] is found yielding one calibration coefficient *k* in [Nm/Volt].

4.3.4 Force balance calibration

One of the two model turbines is mounted on the six-component force balance making it possible to acquire the thrust force onto the rotor. In the scope of this project all experiments are performed with a rotor yaw angle of zero degrees. Thus, only one component of the force balance in axial direction, the R6 component, has to be calibrated. Similar to the torque sensor calibration, defined weights are successively put onto a hanging device creating defined force values [N] onto the R6 force transducer. Also for the force balance a linear dependency between the force [N] and the electrical signal [Volt] from the force transducer is found. One calibration coefficient k in [N/Volt] is derived by a linear regression.

4.4 Control System

The signals of the pressure transducers, the CTA circuit, the torque sensors and the force balance are first amplified and then digitalized by a National Instruments BNC-2110 data acquisition board. An in-house designed LabVIEW interface is used to control the acquired values. The LabVIEW routine features a window for real time signal monitoring as well as acquisition window, which makes it possible to log the acquired data into ASCII-formatted file text files.

By controlling the sampling frequency and the number of samples attained per measurement point it is possible to set the sampling time. For thrust force and torque measurements $600\ samples$ with a sampling frequency of $30\ Hz$ are taken resulting in $20\ seconds$ of sampling time per measurement point. The mean averages of the measured thrust forces and torques are taken over the sampling time of $20\ seconds$. For Pitot tube and Inlet contraction measurements the same settings are sufficient.

When sampling the signal from the hot wire probe, however, a much higher sampling frequency must be used as it is desired to record a high frequency signal of a turbulent flow. Hence, a sampling frequency of $20000\ Hz$ and $1.2\ million\ samples$ yielding a sampling time of $60\ seconds$ is used for hot wire measurements. The time series of all the single measurement points must be recorded in order to be able to reconstruct the signal with all its turbulent fluctuations properly. The mean average of the velocity and turbulence properties can thereafter be derived from the recorded time series samples over a time span of $60\ seconds$.

5 MEASUREMENT CAMPAIGN & DATA EVALUATION

5.1 Measurement Campaign

Within the scope of this project a number of test runs on the described experimental setup comprising the two model turbines in the wind tunnel are performed. An overview of all measurements and experimental setups is presented in *Table 5.1*.

In a first step the flow field at the wind tunnel inlet is scanned using the hot wire probe in exactly the same cross sectional area in which later full area wake measurements are performed. This is done to show that there is a rather uniform laminar inflow with low turbulence intensities to the first wind turbine. As the flow field is expected to be quite uniform, this first traverse matrix only contains 117 measuring points.

Thereafter, C_P and C_T curves are recorded independently for both model turbines. This is done for a number of different wind tunnel inlet speeds. In addition to the speed U_∞ at the inlet contraction, the torque T at the rotor shaft and the thrust force F_T from the wind onto the rotor are logged for varying rotational speeds ω of the turbines. This is done to ensure that the wind turbines have regular operating characteristics and to work out the maximum power point of the turbines.

Although the focus of this investigation is on the wake behind an array of two model turbines, a number of wake measurements behind one model turbine are performed, which is referred to as Arrangement (A). This is done in order to generate some data for comparison with the wake behind two turbines. Measurements of the velocity field in the wake of one turbine have already been carried out by Adaramola and Krogstad [33]. Additional data for more axial measurement stations and for turbulence intensity are needed, so that a number of new wake measurements are performed.

The flow field in the wake is scanned in a horizontal line at hub height ($h = 950\ mm$) behind one model wind turbine (Tu2) at three axial stations 1D, 3D and 5D downstream of the turbine rotor. For each measurement station the flow field is sampled in 27 measuring points, from $z = -975\ mm$ to $z = +975\ mm$. A sketch of the measurement grid for those Horizontal Line Wake measurements is presented in *Fig. 5.1*. The black frame in the sketch represents the wind tunnel boundaries.

Type and location of measurement	Resultant parameters	Method / Instruments	Measurement points
1. Empty wind tunnel			
Area traverse of the wind tunnel inlet	U_m, TI	HW CTA	117
2. Arrangement (A): One turbine in the wind tunnel			
C_P and C_T curves of the unobstructed first model turbine (Tu1)at three different inlet wind speeds	C_P, C_T, λ	RPM sensor, Torque sensor, Balance	20 - 25
C_P and C_T curves of the unobstructed second model turbine (Tu2)at five different inlet wind speeds	C_P, C_T, λ	RPM sensor, Torque sensor, Balance	20 - 25
Line Wake at 1D, 3D & 5D downstream of an unobstructed turbine (Tu2)	U_m, TI	HW CTA	27 per wake
3. Arrangement (B): Two turbines separated x/D=3 rotor diameters			
C_P curve of the second turbine operating in the wake of the first turbine (x/D=3)	C_P, λ	RPM sensor, Torque sensor	20 - 25
Line Wake at 1D, 3D and 5D downstream of the second turbine	U_m, TI	HW CTA	27 per wake
Full Area Wake at 1D, 3D and 5D downstream of the second turbine	U_m, TI	HW CTA	425 per wake
4. Arrangement (C): Two turbines separated x/D=5 rotor diameters			
C_P curve of the second turbine operating in the wake of the first turbine (x/D=5)	C_P, λ	RPM sensor, Torque sensor	20 - 25
Line Wake at 1D and 3D downstream of the second turbine	U_m, TI	HW CTA	27 per wake
Full Area Wake at 1D and 3D downstream of the second turbine	U_m, TI	HW CTA	425 per wake
5. Tip speed ratio variations: Two turbines separated x/D= 3 rotor diameters			
C_P curves of the second turbine for a low TSR (λ=3), the optimum TSR (λ=5,5) and a high TSR (λ=9) of the first turbine	C_P, λ	RPM sensor, Torque sensor	20 - 25
Line Wake at 3D downstream of the second turbine for 9 different TSR combinations	U_m, TI	HW CTA	27 per wake

Table 5.1: *Measurement campaign*

In a second experimental setup, Arrangement (B), both model wind turbines are installed in the wind tunnel with a separation distance of $x/D = 3$ rotor diameters between the turbines. The first turbine (Tu1) is mounted to the force balance and the second turbine (Tu2) to the wind tunnel floor. In this setup the power coefficient C_P of the second turbine operating in the wake of the first is recorded for varying tip speed ratios λ. However, it is not possible to measure the thrust coefficient C_T of the second turbine as it is not fixed to a force balance. Having acquired the C_P curves both turbines are operated at a tip speed ratio λ at their maximum power point for this experimental setup.

The wake behind the array of two turbines is thereafter traversed in a horizontal line at three axial stations 1D, 3D and 5D downstream of the second turbine rotor. The flow field is scanned in 27 points in same measurement locations as before (*Fig. 5.1*). This line traverse yields values for the mean velocity deficit U_m/U_∞ and the turbulence intensities u'/U_m in the locations of the measuring points.

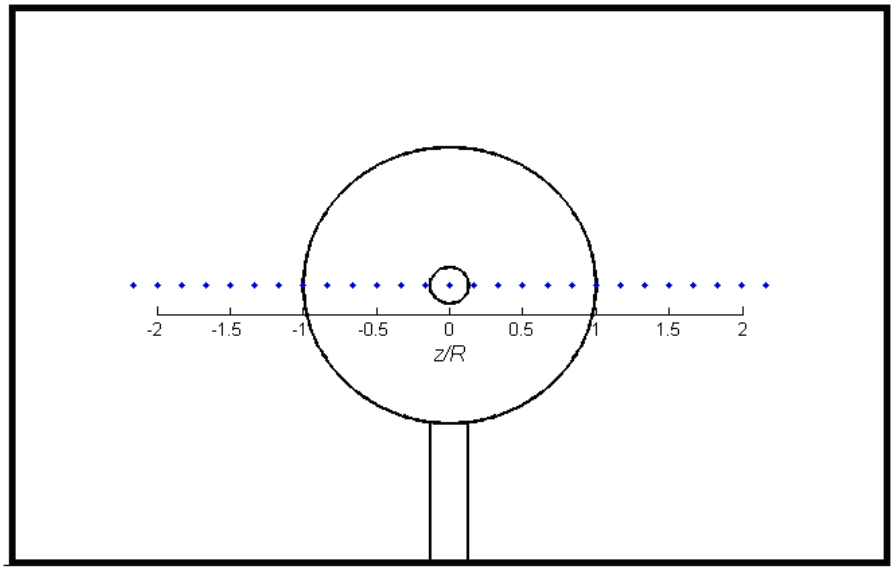

Fig. 5.1: *Location of measurement points for the Horizontal Line Wake measurements*

Furthermore, full area wake measurements are carried out at the same axial stations 1D, 3D and 5D downstream of the second turbine. For each axial measurement station, the flow field is scanned in a rectangular cross section from $y = -600\,mm$ to $y = +600\,mm$ and $z = -900\,mm$ to $z = +900\,mm$ respectively to the center of the rotor hub. The hot wire probe is traversed in steps of $\Delta z = \Delta y = 75\,mm$ in vertical and horizontal direction

resulting in a measurement grid of 425 measuring point per axial station. The measurement grid used for the full area wake measurements is depicted in *Fig. 5.2*.

In a third experimental setup, Arrangement (C), the distance between the turbines is increased to $x/D = 5$ rotor diameters. Firstly, a new C_P curve of the second turbine operating in the wake 5D downstream of the first is recorded. Again, horizontal line wake and full area wake measurement are performed in the axial locations 1D and 3D downstream of the second turbine on the measurement grids shown in *Fig. 5.1* respectively *Fig. 5.2*. Due to length limitations of the wind tunnel, it is not possible to measure the wake 5D downstream of the second turbine in this experimental setup.

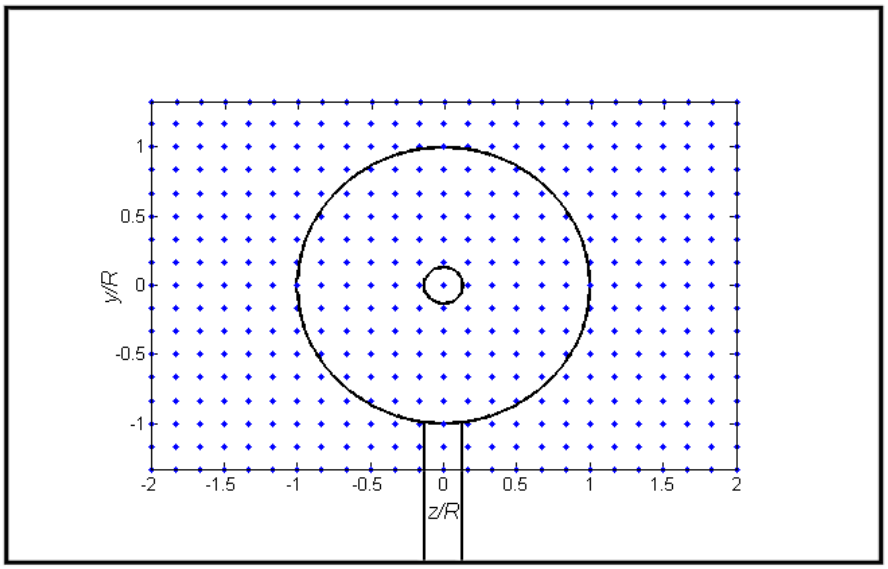

Fig. 5.2: *Location of measurement points for the Full Area Wake measurements*

In a final test series of this project the influence of variations in the tip speed ratio λ of both turbines on the flow field in the wake is analyzed. For this investigation the separation distance between the two turbines is reduced to $x/D = 3$ rotor diameters again.

Three C_P curves of the second turbine are recorded for three different operating points of the first turbine. The first curve is again logged for the optimum operation point of the first turbine ($\lambda = 5.5$), which has been done in the second experimental setup already. Thereafter, C_P curves for a low rotational speed ($\lambda = 3.0$) and a high rotational speed ($\lambda = 9.0$) are recorded. Adaramola and Krogstad [14] extensively studied the effect on the power output of the second turbine when the first turbine is operated at different tip speed

ratios. However, the first turbine was equipped with a different set of blades during their experiments.

Finally, the velocity deficit and the turbulence intensities in the wake are measured in a horizontal line 3D downstream of the second turbine for nine different combinations of tip speed ratios of the two turbines. At first, the tip speed ratio of the first turbine is kept constant while the tip speed ratio of the second turbine is varied to three different operating points. Similarly, three different tip speed ratios of the first turbine are set while the rotational speed of the second turbine is kept constant. Consequently, nine horizontal line wake measurements are performed as shown in *Table 6.1*.

5.2 Data Evaluation

5.2.1 Evaluation of Power and Thrust Curves

As previously mentioned, wind turbine performance curves are usually depicted as functions of the power coefficient C_P and the thrust coefficient C_T over the rotor tip speed ratio λ. In order to record these curves, the rotational speed ω, the torque T and the thrust force F_T onto the rotor are sampled at different inflow velocities U_∞ as schematically shown in *Fig. 5.3*.

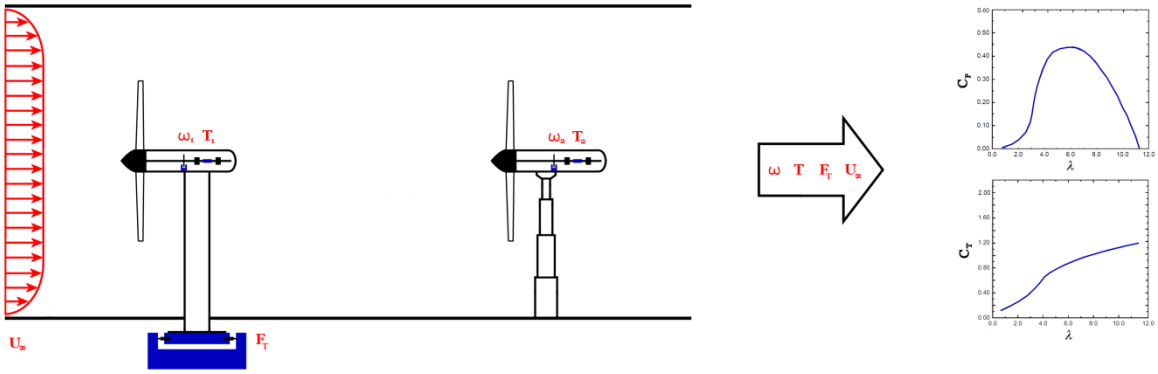

Fig. 5.3: *Data acquisition and evaluation for C_P and C_T curves*

As previously shown in equation (1.6), the tip speed ratio λ is defined as the rotor tip speed divided by the approaching wind speed.

$$\lambda = \frac{\omega R}{U_\infty} \tag{5.1}$$

The power coefficient C_P is calculated as the ratio of the power gained from the wind turbine and the power available from the kinetic energy from the wind through the rotor area as previously shown in equation (1.3). As the power onto the wind turbine shaft is defined as $P = \omega T$, the power coefficient can be directly calculated from equation (5.2).

$$C_P = \frac{\omega T}{\frac{1}{2}\rho\pi R^2 {U_\infty}^3} \tag{5.2}$$

The thrust coefficient C_T is defined as the total axial thrust force F_T onto the rotor divided by a dynamic reference force from the wind onto the rotor area as previously shown in equation (1.5).

$$C_T = \frac{F_T}{\frac{1}{2}\rho\pi R^2 {U_\infty}^2} \tag{5.3}$$

5.2.2 Evaluation of Wake Velocity Field

The flow field in the wake behind the array of the two model wind turbines is traversed with a parallel setup of a Pitot tube and a hot wire probe. The Pitot tube is only used for the calibration of the hot wire circuit and to double check the acquired data from the hot wire signal. Sampling the time series of the hot wire exposed to highly turbulent flow in the turbine wake, a signal of high frequency is recorded. The signal is evaluated regarding the mean velocity deficit U_m/U_∞ [-] and the turbulence intensity u'/U_m [%] in the wake. For temperature correction and statistical evaluation of the hot wire signal, in-house designed FORTRAN routines are used. The results are plotted using the evaluation software MATLAB.

5.2.2.1 Velocity Deficit

Hot wire measurements are very temperature-sensitive as the bridge voltage E is dependent on the fluid velocity and temperature. A temperature change of $1K$ yields a velocity error of approximately 2% [31]. During longer hot wire measurements the fluid temperature is observed to rise between 5 and 8 K. Therefore, a temperature correction is essential.

The bridge voltage E at the output of the CTA is temperature corrected according to

$$E_{corr} = E\left(\frac{T_w - T_0}{T_w - T}\right)^{0.5} \tag{5.4}$$

For a discrete number of N measuring samples the mean velocity U_m is averaged as follows:

$$U_m = \frac{1}{N}\sum_1^N U_i \tag{5.5}$$

The velocity deficit is defined as the ratio of mean velocity U_m and freestream velocity U_∞:

$$Velocity\ Deficit = \frac{U_m}{U_\infty} \tag{5.6}$$

The velocity deficit U_m/U_∞ is a non-dimensional parameter [-].

5.2.2.2 Turbulence Intensity

In *chapter 1.2.3* it is explained how the rotor of a wind turbine induces turbulences to the flow in the wake. Turbulent flow is characterized as a three-dimensional, non-stationary flow and strongly rotational flow [34]. The sequence of the measured flow parameters is seemingly influenced by random. Therefore, it must be described statistically. *Fig. 5.4* shows an example of a velocity signal acquire from an aerodynamic measurement in a turbulent flow.

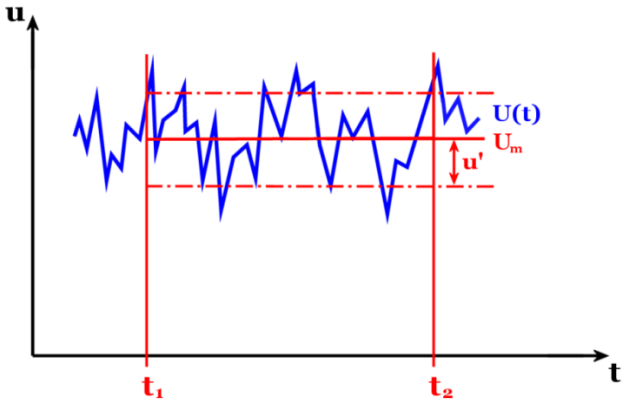

Fig. 5.4: *Velocity signal in a turbulent flow*

The actual velocity U_i at a certain point of time can be split up into two parts, the mean velocity U_m and the velocity fluctuation u_i' in that specific point of time:

$$U_i = U_m + u_i' \tag{5.7}$$

The turbulent fluctuation u' is defined as the standard deviation from the mean. With $u_i' = U_i - U_m$ being the deviation of one certain measuring point from the mean, the standard deviation can be calculated.

$$u' = \sqrt{\frac{1}{N}\sum_1^N (u_i')^2} \tag{5.9}$$

The turbulence intensity is defined as the ratio of the standard deviation u' and the mean velocity U_m.

$$Turbulence\ Intensity = \frac{u'}{U_m} \tag{5.10}$$

Typically, the turbulence intensity u'/U_m is given in percentages [%].

5.3 Measurement Uncertainty

If the flow parameters of an air flow during an experiment change, it is possible that the measurements performed with a hot wire probe are distorted. Apart from the flow conditions, there are several effects in the chain of instruments that can influence the accuracy of the hot wire signal. That includes the hot wire probe, the anemometer circuit and the data acquisition board. Additionally, inaccuracies in the instruments used for calibration have to be taken into account.

The most important source of errors in hot wire measurements are temperature variations in the flow. According to Jørgensen, a change in temperature of $1K$ can evoke an error in measured velocity of about 2% [32]. The voltage signals of all hot wire measurements performed in the scope of this project are temperature corrected according to equation (5.4). Also, variations of the flow pressure, which are directly influenced by the ambient pressure, can influence the heat transfer at the hot wire. As the pressure difference from the calibration procedure to the actual measurement is usually small, the influence of pressure variations is usually neglected. Furthermore, the humidity of the air has an influence on the heat transfer at the hot wire. However, Jørgensen evaluates this influence to be very small and thereby negligible [32].

The measurement chain begins at the hot wire probe. A misalignment of the probe head is a possible source of error. However, this influence can normally be neglected, if the probe head is aligned in the same way during the calibration procedure and the experiment itself. The hot wire voltage is balanced by a CTA circuit in the anemometer. Drift, noise and the frequency response of the anemometer can pose a possible source of error. Also these influences are estimated to be of minor importance as commercial anemometers feature low drift, low noise and good frequency characteristics when justified in the right way. Dependent on the resolution of the data acquisition board, the conversion of the signal from analog to digital can be a possible source of error. For sufficiently high resolutions, the influence of the data acquisition board onto the overall measurement uncertainly is estimated to be very low [32].

A major source of uncertainty in hot wire measurements, however, is assumed to stem from the probe calibration process. The hot wire signal is calibrated against a Pitot tube as a reference. The Pitot signal acquired through a pressure transducer is calibrated against a manual manometer. In this procedure, the flow velocity is calculated from a manual

reading of the alcohol column on the manometer. Each of these steps can contain inaccuracies and therefore must be regarded as a significant source of uncertainty.

As presented in *chapter 4.3.2* the dependency of the flow velocity U on the hot wire voltage E is not linear. A higher grade polynomial curve is fitted to the single calibration points, which involves certain curve fitting errors. This curve fitting process can be a significant source of uncertainties [32].

To sum up, it can be concluded that the major influences on the uncertainty of a hot wire measurement can be ascribed to inaccuracies during the instrument calibration process, the curve fitting errors during the hot wire calibration and temperature variations in the flow (if not corrected).

6 RESULTS & DISCUSSION

6.1 Inlet Flow Field

Initially, the flow field at the wind tunnel inlet is scanned in the same cross sectional area of the subsequent full area wake measurements. The hot wire probe is traversed applying the automatic traverse, which is positioned on rails right underneath the wind tunnel roof. No turbines are installed in the wind tunnel during this inlet traverse, which means there is no blockage effect due to downstream wind turbines. The wind tunnel fan is driven at $450\,rpm$, which yields an average inflow wind speed of about $U_\infty = 11.0\,m/s$ when the wind tunnel is empty. If the model wind turbines were installed in the wind tunnel, the blockage due to the wind turbines would causes an increase in average inflow wind velocity up to around $U_\infty = 11.5\,m/s$.

The inlet is traversed at 117 measuring points in an area from $y = -600\,mm$ to $y = +600\,mm$ and $z = -900\,mm$ to $z = +900\,mm$ with respect to the center of the later installed turbine rotor. *Fig. 6.1* shows the results for the mean velocity U_m [m/s] and the turbulence intensity u'/U_m [%] at the wind tunnel inlet.

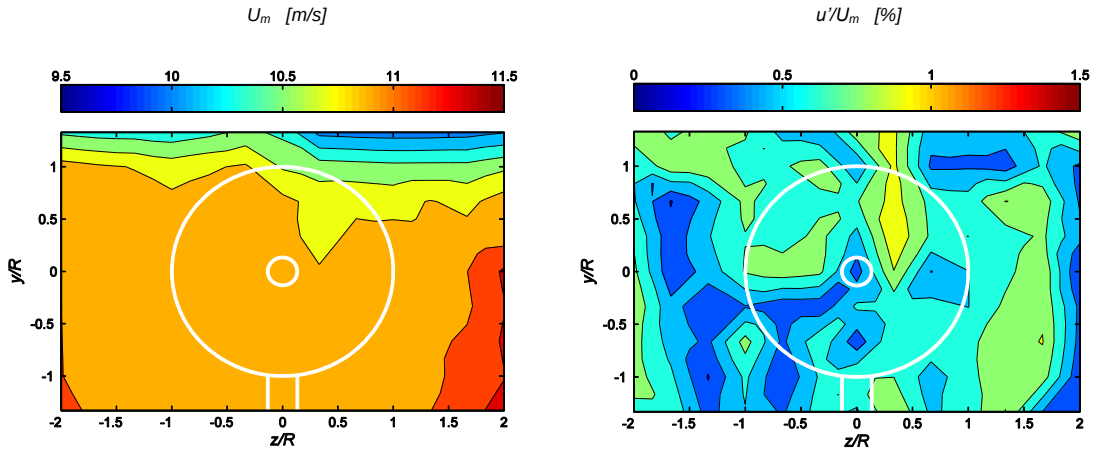

Fig. 6.1: *Mean velocity (U_m) and turbulence intensity (u'/U_m) at the wind tunnel inlet*

The velocity distribution in the inlet flow field is quite uniform except for locally slower velocities near the wind tunnel roof and a slight speed-up near the right wind tunnel endwall. Mean velocities between $U_\infty = 10.00\,m/s$ near the upper wind tunnel endwall and $U_\infty = 11.35\,m/s$ near the right endwall are measured. The region of slightly higher wind speeds is outside the rotor area and therefore not a main concern. The slower wind

velocities near the wind tunnel roof, however, have a significant influence on the inflow to the rotor. The slower wind speeds in this region can be ascribed to a blockage effect of the traverse system, which is installed on rails right underneath the wind tunnel roof. The blockage causes a local increase in static pressure and therefore a decrease in flow velocity. As the wind tunnel roof is located only $y/D = 1.2$ rotor diameters above the wind turbine center, this phenomenon was also previously discovered by Adaramola and Krogstad [14]. The blockage effect of the traverse system can also be seen in the full area mapping of the wake development behind the model turbines.

Although the turbulence intensities seem to be vary a little as plotted in *Fig. 6.1*, they are actually quite uniformly distributed and at a very low turbulence level. The turbulence intensities at the inlet of the wind tunnel range between $u'/U_m = 0.30\%$ and $u'/U_m = 1.00\%$. Although these values are slightly higher than a maximum freestream turbulence intensity of $u'/U_m = 0.20\%$ measured by Adaramola and Krogstad [33] in the same wind tunnel, they still can be considered as a very low turbulence levels.

In *Fig. 6.2* exactly the same data as plotted in *Fig 6.1* is presented. However, in *Fig. 6.2* the same scale for the colour coding as for the full area wake plots is used. The uniformity in mean velocity (depicted as velocity deficit U_m/U_∞ here) and turbulence intensity becomes even more obvious in these plots. Likewise, the slower velocities near the wind tunnel roof can be observed.

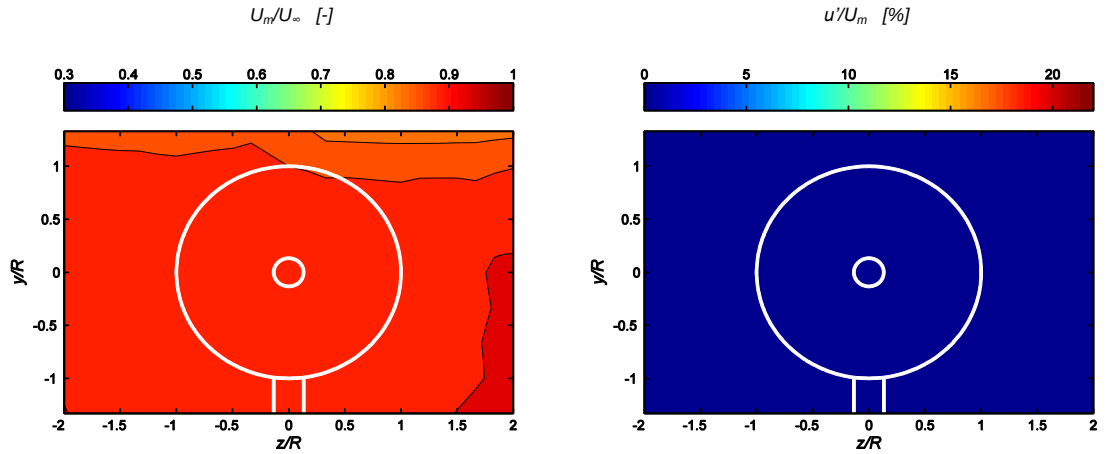

Fig. 6.2: *Velocity deficit (U_m/U_∞) and turbulence intensity (u'/U_m) at the wind tunnel inlet*

It can be concluded, that, except for a local slow-down in mean velocity near the wind tunnel roof, the inflow to the first wind turbine is quite uniform and has very low turbulence intensities.

6.2 Turbine Arrangement (A): Single Turbine Measurements

The experimental investigation of the wake behind one single turbine is not a main focus in the scope of this work. A comprehensive study of the turbine performance and the wake behind one single turbine was already conducted by Adaramola and Krogstad [28], [33] at NTNU's wind tunnel laboratory. However, their studies were not performed under exactly the same boundary conditions. Therefore, some basic performance and wake measurements are performed again in order to create data for comparison to the wake behind an array of two wind turbines. The experimental setup and the axial stations for the hot wire probe measurements are sketched in *Fig. 6.3*.

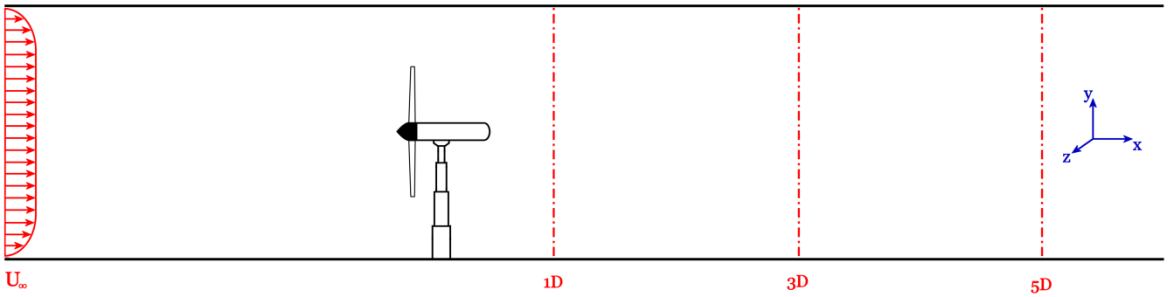

Fig. 6.3: *Experimental setup and axial probe measurement stations for turbine arrangement (A): the single turbine measurements*

At first, C_P and C_T curves for the first model wind turbine (Tu1) are recorded at different inflow wind speeds. Thereafter, the second turbine (Tu2) is set up alone in the wind tunnel. After some C_P and C_T curves are recorded for the second turbine at a number of different inlet wind speeds, wake measurements are performed in a horizontal line in 1D, 3D and 5D downstream of the turbine rotor.

6.2.1 Turbine Performance Curves

6.2.1.1 First Turbine Performance

The power coefficient and the thrust coefficient of the first turbine (Tu1) are presented in *Fig. 6.4*. The curves are recorded for three different inflow wind speeds, $U_\infty = 10.0\,m/s$, $U_\infty = 11.5\,m/s$ and $U_\infty = 13.0\,m/s$.

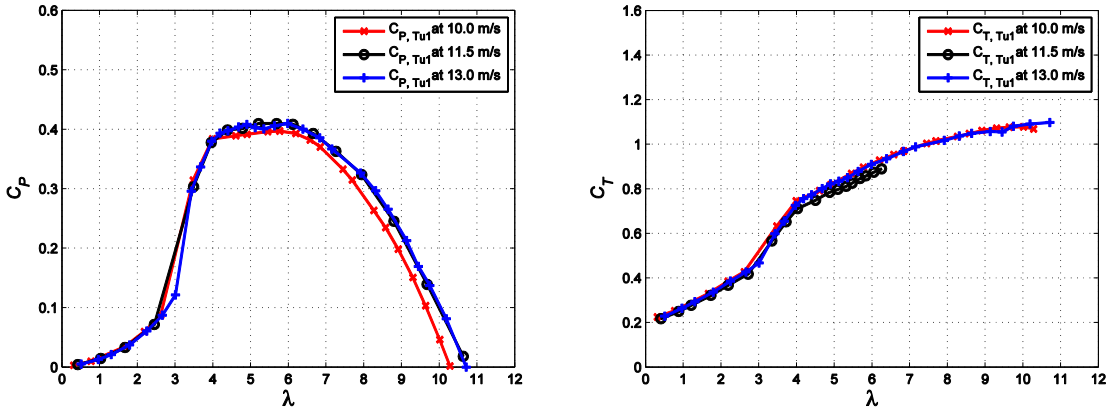

Fig. 6.4: *Performance curves of the first turbine (Tu1) at different inflow wind speeds: (a) power coefficient C_P and (b) thrust coefficient C_T*

Analyzing the power coefficient it becomes obvious that the curves for $U_\infty = 11.5\,m/s$ and $U_\infty = 13.0\,m/s$ are almost identical. A slight bump at $\lambda = 4.8$ for the $U_\infty = 11.5\,m/s$ curve respectively at $\lambda = 5.3$ for $U_\infty = 13.0\,m/s$ can be identified. As these bumps are not very distinct, they have not been further investigated. The run-away point of the power curve for $10\,m/s$ is at about $\lambda = 10.2$ and hence slightly below the run-away point of the curves for higher inflow velocities. Also the maximum power point at $C_P = 0.40$ is slightly lower for the $10\,m/s$ curve. As the shape for $U_\infty = 11.5\,m/s$ and $U_\infty = 13.0\,m/s$ are more or less identical, it can be claimed that a Reynolds-independent curve is reached at $U_\infty = 11.5\,m/s$. Therefore, $U_\infty = 11.5\,m/s$ has been chosen as the design inflow velocity for all succeeding experiments. The maximum power point can be identified for about $\lambda = 5.5$ and amounts a maximum power of about $C_P = 0.42$.

The thrust coefficients C_T for the three different inlet speeds are nearly congruent. The thrust continuously increases with growing tip speed ratios λ reaching a maximum value of $C_T = 1.1$. Between $\lambda = 3.0$ and $\lambda = 4.0$ a steeper increase in thrust can be observed. In

this region a transition from stalled conditions to optimal operating conditions takes place, which also can be observed in the C_P curve.

6.2.1.2 Second Turbine Performance

The power coefficient and the thrust coefficient of the unobstructed second turbine (Tu2) are presented in *Fig. 6.5*. Power and thrust curves for the second turbine were already recorded by Karlsen [16], Loland [35] as well as Adaramola and Krogstad [28] for the same turbine. A comparison between Adaramola and Krogstad's results and the re-recorded performance curves recorded at five different inlet wind speeds is presented in the *Appendix*. The curves are recorded for five different inflow wind speeds, of which three curves for $U_\infty = 8.5\ m/s$, $U_\infty = 9.7\ m/s$ and $U_\infty = 11.5\ m/s$ are shown in *Fig. 6.5*.

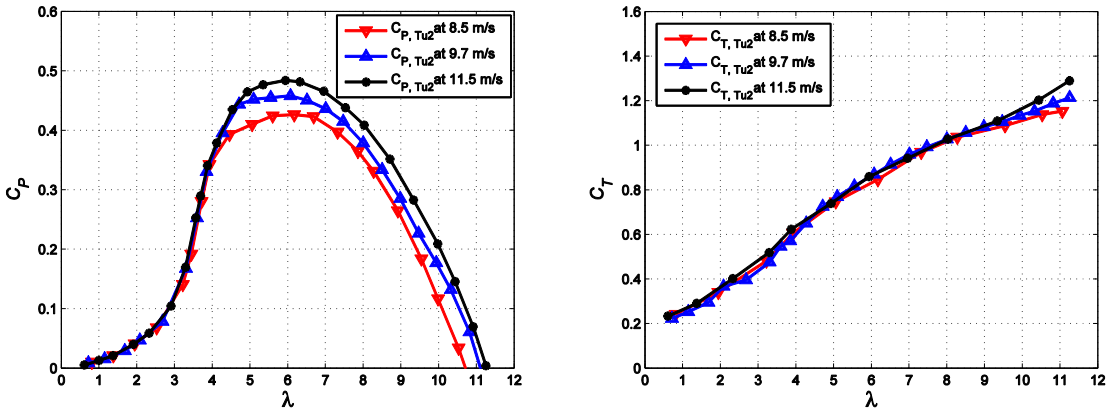

Fig. 6.5: *Performance curves of the unobstructed second turbine (Tu2) at different inflow wind speeds: (a) power coefficient C_P and (b) thrust coefficient C_T*

Above $U_\infty = 8.5\ m/s$ inlet speed the power and thrust curves are fully developed and therefore smoothly shaped. The power curves for $U_\infty = 9.7\ m/s$ and $U_\infty = 11.5\ m/s$ are almost identical. However, the maximum power point of the $U_\infty = 9.7\ m/s$ curve still is slightly below the $U_\infty = 11.5\ m/s$ curve. The power curve for the second turbine at design inflow speed $U_\infty = 11.5\ m/s$ has its maximum power point $C_P = 0.47$ at a tip speed ratio of $\lambda = 6.0$. The run-away point can be found at $\lambda = 11.2$.

The thrust curves for the three different inlet speeds are almost congruent. Insignificant deviations can be found at high tip speed ratios between $\lambda = 10.0$ and $\lambda = 11.0$. The Reynolds number does not have hardly any influence on the thrust curves.

The power curve at design inflow speed $U_\infty = 11.5\ m/s$ matches very good with the curves found by Karlsen [16], Loland [35] as well as Adaramola and Krogstad [28] for the same turbine. However, Adaramola and Krogstad found a Reynolds-independent curve already at a little lower wind tunnel inflow speed U_∞ (see *Appendix*).

Furthermore, the thrust curves are in good agreement with the results found previously by Adaramola and Krogstad. The thrust curves as shown in *Fig. 6.5*, however, reach slightly higher thrust values of about $C_T = 1.3$ than Adaramola and Krogstad's curve, which features a maximum thrust of approximately $C_T = 1.2$ (see *Appendix*).

According to the Betz theory [12], the thrust coefficient is below one for full size wind turbines. As the model wind turbines are installed in a closed wind tunnel, the blockage of the wind tunnel endwalls causes an increased local velocity in front of the rotor, resulting in a higher thrust force onto the rotor [35].

6.2.2 Downstream Flow Field

In *Fig. 6.6* the mean velocity deficit U_m/U_∞ [-] and the turbulence intensity u'/U_m [%] are shown for three axial downstream positions. Horizontal line wake measurements in hub height are presented for the axial measurement stations 1D, 3D and 5D downstream of the unobstructed second turbine (Tu2). At a wind tunnel inflow speed of $U_\infty = 11.5\ m/s$, the second turbine is run at a tip speed ratio of $\lambda = 6.0$ corresponding to its maximum power point at $C_P = 0.47$.

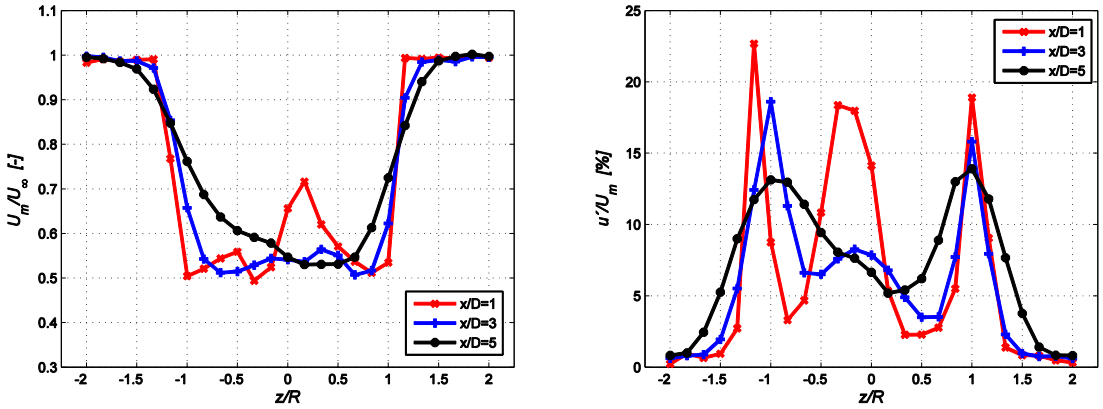

Fig. 6.6: *Velocity deficit (U_m/U_∞) and turbulence intensity (u'/U_m) in the wake 1D, 3D and 5D downstream of the unobstructed turbine*

Velocity deficit

Analyzing the axial development of the velocity deficit in the wake behind one single turbine, it can be observed that the velocity deficit recovers moving downstream. At 1D downstream a minimum mean velocity of $U_m = 5.9\ m/s$ (corresponds to $U_m/U_\infty = 0.49$) is measured. At 3D downstream the minimum velocity amounts $U_m = 6.1\ m/s$, which corresponds to a velocity deficit of $U_m/U_\infty = 0.51$. At 5D the mean velocity has recovered to $U_m = 6.4\ m/s$ respectively $U_m/U_\infty = 0.53$.

Wake dimensions

Furthermore, it can be observed that the wake becomes broader moving downstream due to turbulent diffusion from the surrounding flow. The 1D wake is characterized by strong velocity gradients behind the rotor tips at $z/R = -1$ and $z/R = 1$ and the wake width

amounts approximately $\Delta z/R = 2.5$ rotor radii. The velocity gradients of the 3D and 5D wake are significantly weaker yielding a smoother velocity profile and a slightly broader wake. The 5D wake features a wake width of approximately $\Delta z/R = 3.0$ rotor radii.

Wake asymmetries

Focusing on the center of the wake, it can be observed that the 1D wake is characterized by a very asymmetrical velocity field with high variations in mean velocity deficit. Moving further downstream, the wake profile becomes more symmetrical and the variations gradually even out. The near wake at 1D is dominated by distinct single root and tip vortices, whereas these single vortices mix to a more uniform structure due to turbulent diffusion when moving downstream. The asymmetries in the horizontally measured velocity profile can be traced back to the influence of the wake of the wind turbine tower. The flow exiting from the rotor is in a swirling motion that is counter-rotating to the rotor as explained in *chapter 1.2.3*. This rotating flow in the rotor wake is hitting the tower at a certain angle and moving into the lower-pressure region in the tower wake yielding an asymmetrical velocity distribution [23]. These asymmetries are dominating the shape of the velocity and turbulence intensity profile in the 1D wake. This idea is confirmed by results found by Nygard [36], who performed a comprehensive study about the deflection of the tower wake due to wake rotation on the first wind turbine (Tu1) at NTNU's wind tunnel laboratory.

Turbulence intensities

The turbulence intensity gradually goes back moving downstream in the wake. For the 1D wake a maximum turbulence intensity of $u'/U_m = 22.7\%$ could be found, which reduces to a maximum of $u'/U_m = 13.9\%$ in the 5D wake.

Likewise to the velocity profiles, it can be observed that the turbulence profiles in the wake become broader moving downstream. Due to turbulent diffusion from the surrounding flow, the circular turbulent shear layer slowly increases in diameter.

The 1D wake is characterized by three distinct peaks with very high turbulences levels. It can be observed that peaks in the turbulence intensity profile occur at positions with high

velocity gradients in the velocity profile. The peaks at $z/R = -1$ and $z/R = 1$ can clearly be ascribed to the tip vortices, whereas the peak in the center is assumed to occur due to a combination of the root vortices and turbulent structures behind the turbine nacelle. Moving downstream, these peaks in turbulence intensity gradually reduce. The turbulent peak, which can be ascribed to the root vortices, goes back at a higher rate than the tip vortex peaks. The profiles become more even and smoother due to diffusion processes moving downstream from the rotor. Distinct maxima in the tip vortex region at $z/R = -1$ and $z/R = 1$ still can be found in the 5D wake. The maximum in the wake center induced by the root vortices cannot be found in the 5D wake profile anymore.

Distinct asymmetries are also evident in the turbulence intensity profiles, especially in the 1D profile. Again, the tower wake influence transported by the swirling motion in the wake is assumed to be the reason for these asymmetries.

Classification of results

In the past, Adaramola and Krogstad performed a number of wake measurements using a Pitot tube [33] respectively a LDA system [37] on the same experimental setup. Furthermore, some velocity profiles in the wake behind the single model wind turbine (Tu2) were recorded by Loland [35] using a Pitot tube.

The velocity deficit profile measured at 1D downstream matches almost exactly with the Pitot measurement performed in [33]. A very good agreement can also be found with the 1D profile measured in [35], although the curve is slightly above the newly measured profile. A different reference velocity U_∞ is assumed to be the reason for this displacement. Moreover, the velocity profiles measured at 4D and 7D in [35] fit well into the axial development of the wake as measured in the present project.

The shape of turbulence intensity profile measured at 3D downstream gives good agreement with the turbulence profile measured in [37]. Notice that Adaramola and Krogstad refer the standard deviation u' to the inflow velocity U_∞ in their paper [37], whereas in this work the turbulence intensity is defined as u'/U_m.

Evident asymmetries in velocity profiles are, among others, also found by Barber et al. [23] and Smith [38].

6.3 Turbine Arrangement (B): Turbine distance x/D=3

The main focus in this project is the investigation of the development of the wake behind an array of two model wind turbines. In a first experimental setup, the second model turbine is installed $x/D = 3$ rotor diameters downstream of the first model turbine. The experimental setup and the axial stations for the hot wire probe measurements are sketched in *Fig. 6.7*.

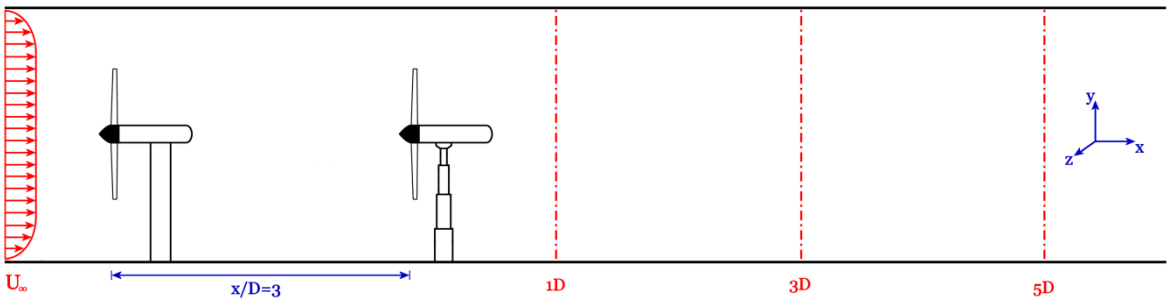

Fig. 6.7: *Experimental setup and axial measurement stations for turbine arrangement (B)*

The first model turbine is mounted on the force balance, whereas the second turbine is fixed to the wind tunnel floor. The first wind turbine is operated at a tip speed ratio of about $\lambda = 5.5$, which corresponds to the optimal operating point at a maximum power output $C_{P,max,Tu1} = 0.42$. A power curve of the second turbine operating in the wake of the first turbine is recorded yielding the optimal operating point for the second turbine. As the second turbine is not mounted to the force balance, no thrust curve is acquired in this setup. At three axial measurement stations 1D, 3D and 5D downstream of the second model turbine, wake measurements are performed. The velocity deficit and the turbulence intensity are measured in a horizontal line at hub height at the three measurement stations, followed by full area wake measurements at the exact same downstream positions.

6.3.1 Turbine Performance Curves

A comparison of the C_P curve of the second turbine operating unobstructed and in the wake 3D downstream of an upstream turbine is presented in *Fig. 6.8*. The upstream turbine is operating at maximum C_P. The two graphs in *Fig. 6.8 (a)* and *(b)* actually show the same data, but the data in the second picture is referred to a different reference velocity.

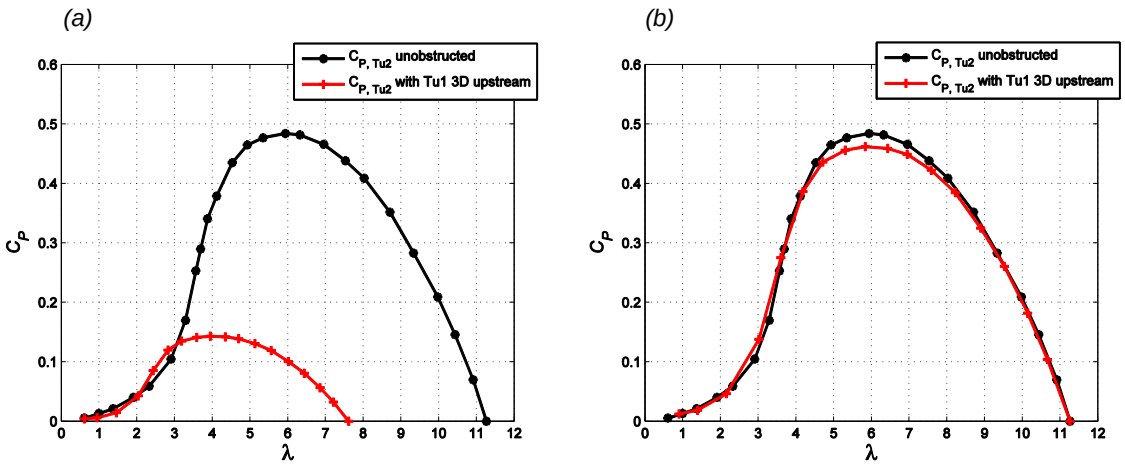

Fig. 6.8: *C_P curve of the second turbine (red) operating 3D downstream of the first turbine: (a) reference velocity U_∞=11.5 m/s (b) reference velocity $U_{ref,3D}$=7.8 m/s*

In *Fig. 6.8 (a)* both power curves are referred to the wind tunnel inflow velocity U_∞. It can be observed that the second turbine reaches a maximum power of $C_P = 0.15$ when operating in the wake 3D downstream. This corresponds to about 31% of the power extracted from the wind of the unobstructed turbine. Being exposed to a considerably lower velocity in the wake of the first turbine, the run-away point goes back to a tip speed ratio of $\lambda = 7.6$.

In order to compare the performance of the second turbine operating in the wake, the power curve is referred to a lower reference velocity $U_{ref,3D}$ as depicted in *Fig. 6.8 (b)*. When the second turbine is operated in the wake of the first turbine, it is subjected to a completely different inflow field. This flow field can be characterized by a non-uniform velocity distribution and very high, unevenly distributed turbulent flow structures. As no data of the velocity deficit in the wake of the first turbine are available, the power curve is stretched to the run-away tip speed ratio of the unobstructed second turbine.

Although the power curve of the second turbine does not necessarily have to have the same run-away tip speed ratio when operating in the wake, the reference velocity $U_{ref,3D} = 7.6\ m/s$ is chosen here to simplify the comparison with the unobstructed setup.
It can be observed that the power curve matches almost perfectly with the curve of the unobstructed turbine. It reaches a maximum $C_P = 0.46$, which is just slightly lower than the maximum C_P of the unobstructed turbine.
Comparing this power curve at a reference velocity of $U_{ref,3D} = 7.6\ m/s$ to the power curve of the second turbine operating unobstructed at an inlet speed of $U_\infty = 7.2\ m/s$ as shown in *Fig. A.1* (*Appendix*), it can be seen that the power curve of the turbine operating in the turbulent wake is fully developed. At a rather laminar inflow field of $U_\infty = 7.2\ m/s$, however, the power curve features a distinct bump at design tip speed ratios. This can be ascribed to a Reynolds number effect, which is described in detail in *Appendix*.
Thus, it can be concluded that the second wind turbine operating in a highly turbulent flow in the wake of an upstream turbine has a fully developed power curve and reaches similar efficiency as the unobstructed turbine.

6.3.2 Downstream Flow Field

6.3.2.1 Horizontal Line Wake Measurements

In *Fig. 6.9* the axial development of the velocity deficit U_m/U_∞ [-] and the turbulence intensity u'/U_m [%] is shown for three axial positions. Horizontal line wake measurements in hub height are presented for the axial measurement stations 1D, 3D and 5D downstream of the second turbine operating 3D downstream of the first turbine. At a wind tunnel inflow speed of $U_\infty = 11.5\,m/s$, both turbines are operated at their maximum power point at $C_{P,max,Tu1} = 0.42$ respectively $C_{P,max,Tu2} = 0.15$.

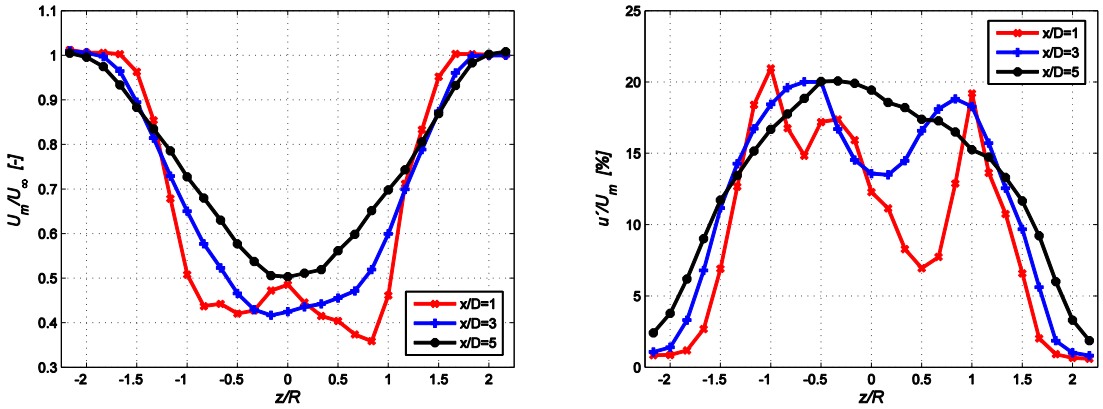

Fig. 6.9: *Velocity deficit (U_m/U_∞) and turbulence intensity (u'/U_m) in the wake 1D, 3D and 5D downstream of the second turbine operating 3D downstream of the first turbine*

Velocity deficit

Similar to the wake behind a single turbine the velocity deficit in the wake behind an array of two turbines recovers when moving downstream. At 1D downstream a minimum mean velocity of $U_m = 4.3\,m/s$ is measured, which corresponds to a velocity deficit of $U_m/U_\infty = 0.36$. Moving to 3D downstream, the minimum mean velocity amounts $U_m = 5.0\,m/s$ $(U_m/U_\infty = 0.42)$ and at 5D downstream the minimum velocity recovers to $U_m = 6.0\,m/s$ $(U_m/U_\infty = 0.50)$.

Wake dimensions

Likewise to the wake behind the single turbine, the wake becomes broader moving downstream. The 1D wake is nearly $z/R = 3$ rotor radii broad, whereas the 5D wake has a

wake width of almost $z/R = 4$ rotor radii. This corresponds to a growth rate of approximately $\Delta z/\Delta x = 12.5\%$ in horizontal direction. Turbulent diffusion from the surrounding flow causes this phenomenon, but also the influence of the wake of the first turbine must be taken into account when judging the wake width. An in-depth investigation of what phenomena can actually be ascribed to the first turbine wake is found in *chapter 6.5*. The 1D wake features significantly stronger velocity gradients in the turbulent shear layer than the 3D and 5D wake.

Wake asymmetries

The wake measurements in a horizontal line show obvious asymmetries at 1D downstream. These can be explained by the influence of the tower wake being deflected by the rotating motion in wake of the turbine rotor. The 1D wake is characterized by significant variations in mean velocity in the center of the wake. Two distinct minima, which be ascribed to the shear layer created by the tip vortex rotation, can be made out. The 3D and 5D wake, however, are characterized by an almost symmetrical shape featuring only one distinct minimum in mean velocity.

Turbulence intensities

Analyzing the axial development of the turbulence intensity profiles, an increase in width can be observed moving axially downstream. The turbulent shear layer induced by the tip vortices gradually diffuses into the surrounding flow.

The 1D profile features three distinct maxima that can be ascribed to the tip and root vortices. The highly asymmetrical profile has a maximum turbulence intensity of $u'/U_m = 21.0\%$.

The profile in the wake 3D downstream of the second turbine is characterized by two distinct peaks, which slightly moved towards the center of the wake. The peak in the center of the wake disappeared completely. The profile has a maximum turbulence intensity of $u'/U_m = 20.0\%$ and can be characterized by much smoother and more symmetrical shape than the 1D profile.

No more distinct vortex structures can be identified in the turbulence intensity profile 5D downstream of the second turbine. The vortices have mixed into one single peak due to turbulent diffusion processes. This fully developed turbulence profile has a maximum intensity of $u'/U_m = 20.1\%$.

6.3.2.2 Full Area Wake Measurements

At the same three axial positions, the flow field is traversed in a rectangular including a total of 425 measuring points. The mean velocity deficit U_m/U_∞ [-] and the turbulence intensity u'/U_m [%] are depicted in colour coded contour plots in *Fig. 6.10*, *Fig. 6.11* and *Fig. 6.12* for the axial positions 1D, 3D respectively 5D downstream of the second turbine, which is operating 3D downstream of the first turbine.

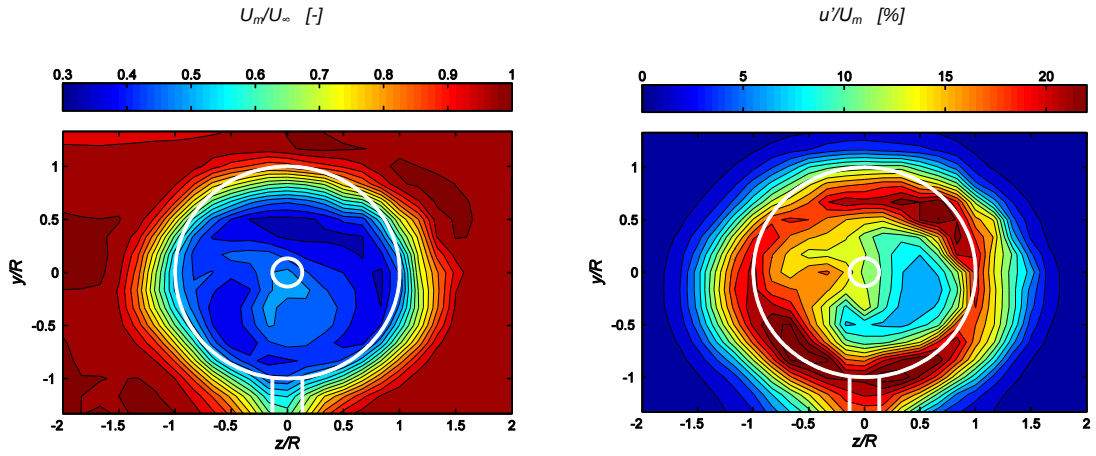

Fig. 6.10: *Velocity deficit (U_m/U_∞) and turbulence intensity (u'/U_m) in the wake 1D downstream of the second turbine operating 3D downstream of the first turbine*

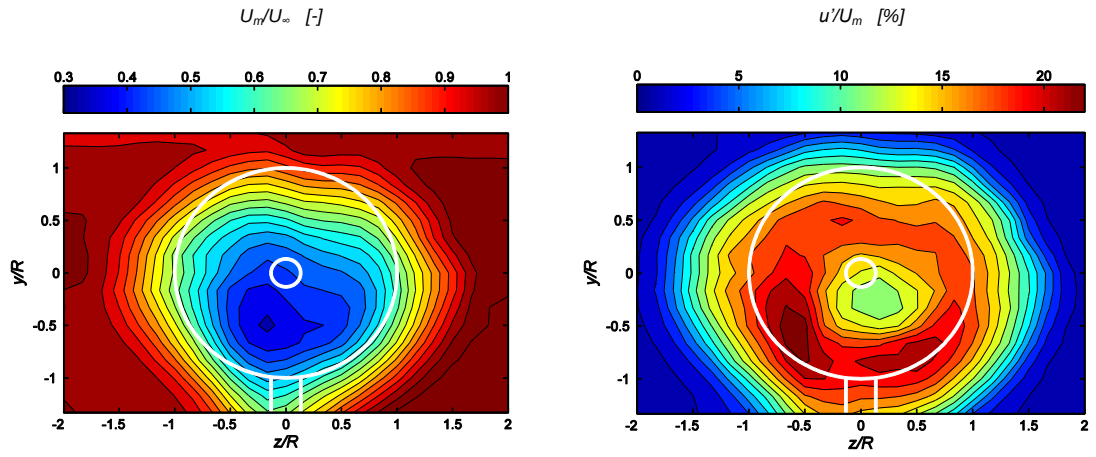

Fig. 6.11: *Velocity deficit (U_m/U_∞) and turbulence intensity (u'/U_m) in the wake 3D downstream of the second turbine operating 3D downstream of the first turbine*

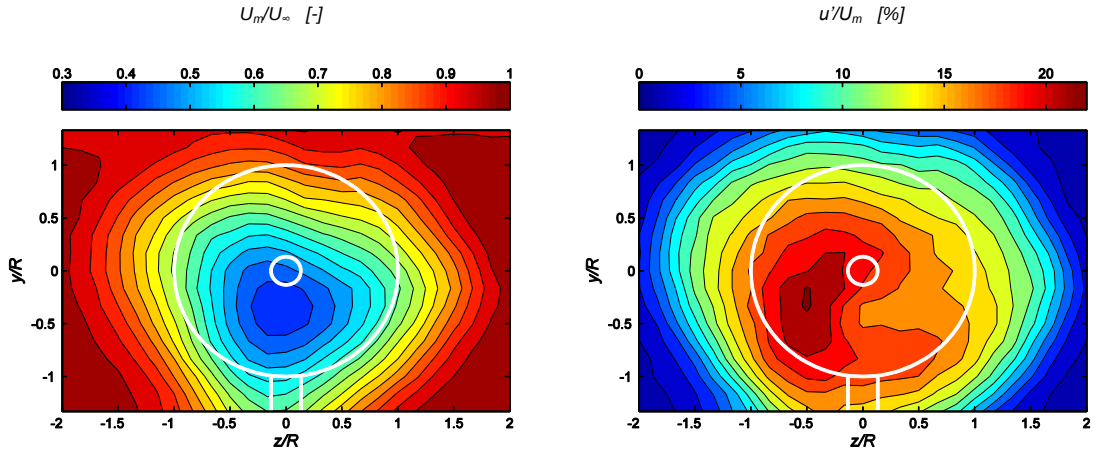

Fig. 6.12: *Velocity deficit (U_m/U_∞) and turbulence intensity (u'/U_m) in the wake 5D downstream of the second turbine operating 3D downstream of the first turbine*

Velocity deficit

As observed in the horizontal line profiles, the 1D wake features strong velocity gradients right outside the rotor swept area as shown in *Fig 6.10*. The highest velocity deficits of about $U_m/U_\infty = 0.35$ can be found above the center of the rotor and right to the center in the region near the blade tips. Further downstream the velocity deficit decreases visibly and the highest deficits are located slightly underneath the center of the turbine rotor. The minimum velocity found in the 3D wake amounts $U_m/U_\infty = 0.36$, whereas the 5D wake features a minimum velocity of $U_m/U_\infty = 0.42$.

Wake dimensions

The 1D wake has a horizontal expansion from $z/R = -1.5$ to $z/R = 1.5$, whereas in vertical direction it only grows until $y/R = 1.2$ referring to the wake's velocity profile.
The upper half of the wake is thus not entirely circular, which can be ascribed to a blockage effect of the traverse system on the wind tunnel roof. The same phenomenon was found by Adaramola and Krogstad, who claim that the vertical growth rate near the roof is only about 85% of the growth rate in horizontal direction [33]. The blockage effect of the traverse system is also found in the mapping of the wind tunnel inflow velocity as described in *chapter 6.1*.
Moving further downstream, it can be observed that the wake expands in all directions. As seen before, the horizontal expansion is much more distinct in comparison to the vertical expansion. 5D downstream of the second turbine rotor, the wake is almost $\Delta z/R = 4$ rotor radii broad. The velocity gradients become weaker when the wake is moving downstream. Fluid of higher kinetic energy is slowly transported into the center of the wake due to turbulent diffusion. Hence, the area of high velocity deficit shrinks moving downstream in the wake.
It can be clearly observed that the center of the maximum velocity deficit is located slightly underneath the center of the rotor in the 3D and 5D wake. A certain downshift of the highest velocity deficit is also found in experiments featuring a simulated atmospheric boundary layer by Talmon [39], [40]. Referring to a computational study by Crespo et al.

[41] validating Talmon's results, Vermeer et al. conclude that "this downshift is mainly due to the shear of the incoming flow and the presence of the ground" [10].
In the present experiments, however, there is no shear in the inlet flow field. Thus, it is assumed that the blockage due to the traverse system near the wind tunnel roof is responsible for this displacement. Furthermore, a lower-pressure region in the tower wake could possibly cause a certain downshift in the wake. In order to assess the influence of the traverse mechanism respectively the tower, a vertical traverse of the flow field using a manual traverse mechanism is recommended.

Wake asymmetries

The center of the 1D wake is characterized by high velocity deficits behind the rotor swept area. It can be observed that there are some centers of extra high velocity deficits in the upper and right half of the velocity field, which are not evenly distributed around the circumference. The flow field is not rotationally symmetric. It is assumed that these asymmetries stem from the influence of the turbine tower. The flow exiting from the rotor blades is rotating and hitting the turbine tower resulting in a non-uniform velocity distribution in the center of the wake. Barber et al. [23] observed a similar phenomenon while mapping the full area wake behind a single turbine. They assume that the rotating flow in the rotor wake is hitting the tower at a certain angle and moving into the lower-pressure region in the tower wake yielding an asymmetrical velocity distribution [23]. These asymmetries are dominating the shape of the velocity and turbulence intensity profile in the 1D wake. Moving further downstream, the profiles become more symmetrical due to turbulent mixing processes.

Turbine tower influence

Analyzing the lower half of the velocity field, the influence of the turbine tower can be clearly seen. The presence of the tower causes a bluff body wake characterized by an additional velocity deficit. At the lower edge of the scanned velocity field it can be seen that the wake around the turbine tower is slightly shifted towards the left hand side. Looking in downstream direction, the turbine rotor is rotating counter-clockwise. Thus,

the flow in the wake is rotating in clockwise direction shifting the flow field around the tower a little bit to the left.

The same phenomenon becomes even more obvious in the velocity distributions shown in *Fig. 6.11* and *Fig. 6.12*. In the 3D and 5D measurements, the flow around the tower is shifted even more to the left hand side. These findings are in accordance with investigations made by Nygard [36] on the first wind turbine. He states that "as the wake propagates downstream, the tower wake is displaced due to the clockwise rotation of the wake" [36].

Turbulence intensities

Investigating the turbulence intensity profile in the 1D wake as depicted in *Fig. 6.10*, it can be observed that the highest turbulences are in a distinct ring behind the rotor blade tips. This is obviously due to the very turbulent shear layer formed by the blade tip vortices. Three independent cores of very high turbulence intensity levels above $u'/U_m = 20\%$ can be found. However, these cores are not distributed uniformly around the circumference. The center of the wake can be characterized by a very non-uniform turbulence distribution. Both cores of rather high and relatively low turbulence intensities coexist. Slightly to the right of the rotor center a core of comparatively low turbulence of about $u'/U_m = 7\%$ can be found.

In the 3D wake as shown in *Fig. 6.11* only two cores of very high turbulences above $u'/U_m = 20\%$ are found in the lower half of the flow field. The turbulence level in the center of the wake is increased to about $u'/U_m = 12\%$. Likewise the velocity profiles, the wake becomes broader and the gradients of turbulence intensity are reduced.

The turbulence intensity profile of the 5D wake as presented in *Fig. 6.12* still is quite asymmetrical. Only one core of very high turbulences can be found in the right half of the flow field. Turbulent diffusion causes a further increase in the wake extensions and smoother gradients in turbulence intensity.

6.4 Turbine Arrangement (C): Turbine distance x/D=5

In a second experimental setup, the separation distance between the two model turbines is increased to $x/D = 5$ rotor diameters. As shown in *Fig. 6.13*, hot wire probe measurements are performed 1D and 3D downstream of the second turbine. Due to a limited length of the wind tunnel, wake measurements 5D downstream of the second turbine are unfortunately not possible in this experimental setup.

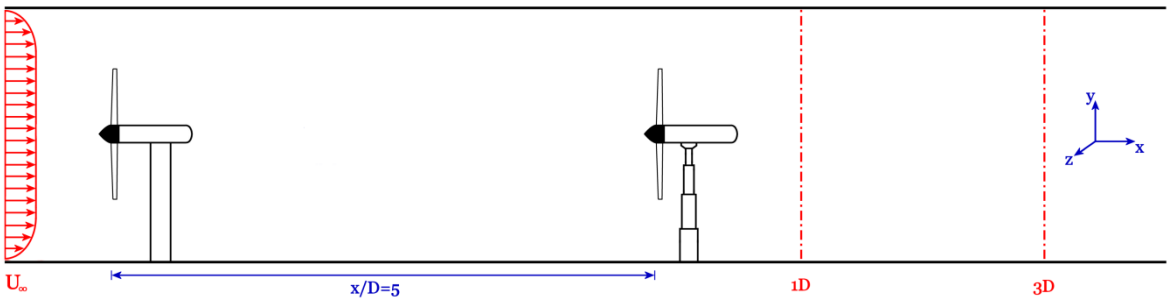

Fig. 6.13: *Experimental setup and axial measurement stations for turbine arrangement (C)*

Likewise in the initial setup, the first turbine is mounted on the force balance whereas the second turbine is fixed to the wind tunnel floor. The first wind turbine is operated at the same tip speed ratio of about $\lambda = 5.5$, corresponding to the optimal operating point at a maximum power output $C_{P,max,Tu1} = 0.42$. As the separation distance is increased, a new power curve of the second turbine operating in the wake 5D downstream is recorded yielding the optimal operating point for the second turbine in this setup. With the second turbine being operated at the optimal power point, the wake is recorded at two axial stations 1D and 3D downstream of the second turbine. Wake measurements yielding the velocity deficit and the turbulence intensity are again performed in a horizontal line at hub height and a full area grid behind the turbines at the two axial measurement stations.

6.4.1 Turbine Performance Curves

Fig. 6.14 shows a comparison of the C_P curve of the second turbine operating unobstructed and 5D downstream of the first turbine. The upstream turbine (Tu1) is operated at its maximum power point at about $\lambda = 5.5$. The same data is presented in *Fig 6.14 (a)* and *(b)* the only difference being a different reference velocity.

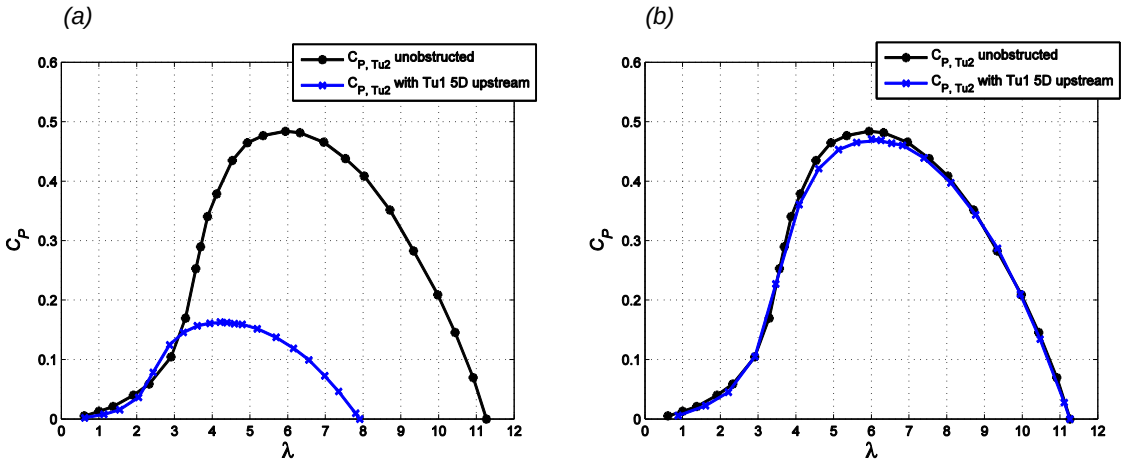

Fig. 6.14: *C_P curve of the second turbine operating 5D downstream of the first turbine: (a) reference velocity U_∞=11.5 m/s (b) reference velocity $U_{ref,5D}$=8.1 m/s*

Both power curves are referred to the wind tunnel inflow velocity U_∞ in *Fig. 6.14(a)*. Operating 5D downstream of the first turbine, the second turbine reaches a maximum power of $C_P = 0.16$, which corresponds to about 33% of the power the unobstructed turbine extracts from the wind.

For a better comparison, the C_P curve is referred to a lower reference velocity $U_{ref,5D}$ as presented in *Fig. 6.8 (b)*. In the same way as before, the power curve is stretched to the run-away tip speed ratio of the unobstructed second turbine. It can be observed that the power curve matches almost perfectly with the curve of the unobstructed turbine. The maximum power coefficient of $C_P = 0.47$ is just slightly lower than the maximum C_P of the unobstructed turbine.

Again, it can be seen that the second wind turbine operating in a turbulent flow in the wake of an upstream turbine has similar operating characteristics as the unobstructed turbine.

6.4.2 Downstream Flow Field

6.4.2.1 Horizontal Line Wake Measurements

The velocity deficit U_m/U_∞ [-] and the turbulence intensity u'/U_m [%] for the two axial measurement stations 1D and 3D downstream of the second turbine operating 5D downstream of the first turbine are presented in *Fig. 6.15*. Both model wind turbines are operated at their maximum power point at $C_{P,max,Tu1} = 0.42$ respectively $C_{P,max,Tu2} = 0.16$.

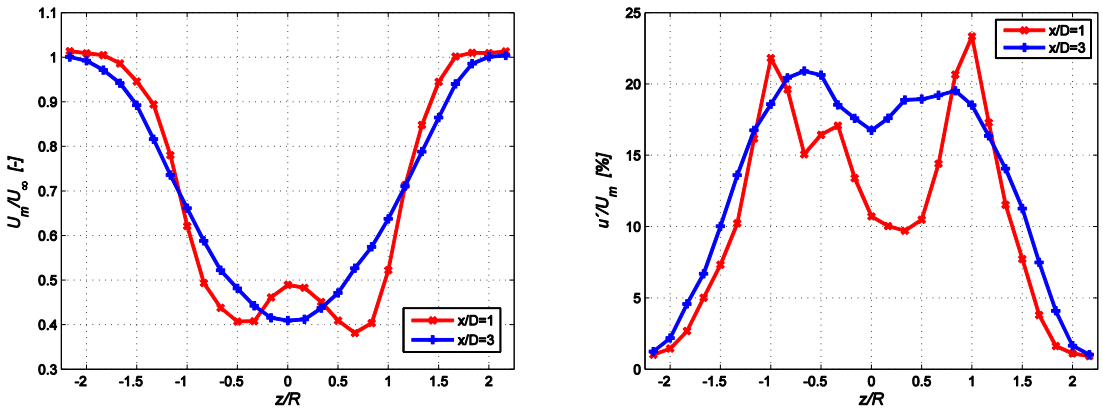

Fig. 6.15: *Velocity deficit (U_m/U_∞) and turbulence intensity (u'/U_m) in the wake 1D, 3D downstream of the second turbine operating 5D downstream of the first turbine*

Velocity deficit

As observed before, the velocity deficit in the wake behind an array of two turbines recovers when moving downstream. A minimum mean velocity of $U_m = 4.6\, m/s$ corresponding to a velocity deficit of $U_m/U_\infty = 0.38$ is measured at 1D downstream. Moving to 3D downstream, the minimum mean velocity recovers to $U_m = 4.9\, m/s$ corresponding to a velocity deficit of $U_m/U_\infty = 0.41$.

Wake dimensions

A broadening of the wake can also be observed in this setup when moving downstream. The 1D wake is approximately $z/R = 3.5$ rotor radii broad, whereas the 3D wake has a wake width of about $z/R = 4$ rotor radii. Similar to the first setup, this corresponds to a growth rate of about $\Delta z/\Delta x = 12.5\%$ in horizontal direction.

Wake asymmetries

The velocity deficit profiles acquired from the horizontal line wake measurements are almost symmetrical in this setup. The 1D profile features two distinct minima, of which the right one is slightly lower. The 3D velocity profile is nearly symmetrical for this setup. Obvious asymmetries can be observed in the turbulence intensity profiles, especially for the 1D profile. The influence of the tower wake being deflected by the rotating motion in wake of the turbine rotor and thereby deflecting turbulent structures, such as the root vortices is assumed to cause these asymmetries.

Turbulence intensities

An increase in wake width can also be observed when analyzing the axial development of the turbulence intensity profiles. The 1D profile is characterized by three distinct maxima, which can be ascribed to the tip and root vortices. A maximum turbulence intensity of $u'/U_m = 23.3\%$ can be found in the highly asymmetrical profile.

The turbulence intensity profile in the 3D wake features two distinct peaks, which moved towards the center of the wake. The peak in the center of the wake disappeared completely at 3D. The profile has a much smoother and more symmetrical shape than the 1D profile and features a maximum turbulence intensity of $u'/U_m = 20.9\%$.

6.4.2.2 Full Area Wake Measurements

For the two axial positions 1D and 3D downstream of the second turbine, the flow field is traversed in a rectangular measurement grid consisting of 425 measuring points. For the second turbine operating 5D downstream of the first turbine, the mean velocity deficit U_m/U_∞ [-] and the turbulence intensity u'/U_m [%] are presented in colour coded contour plots in *Fig. 6.16* and *Fig. 6.17.*

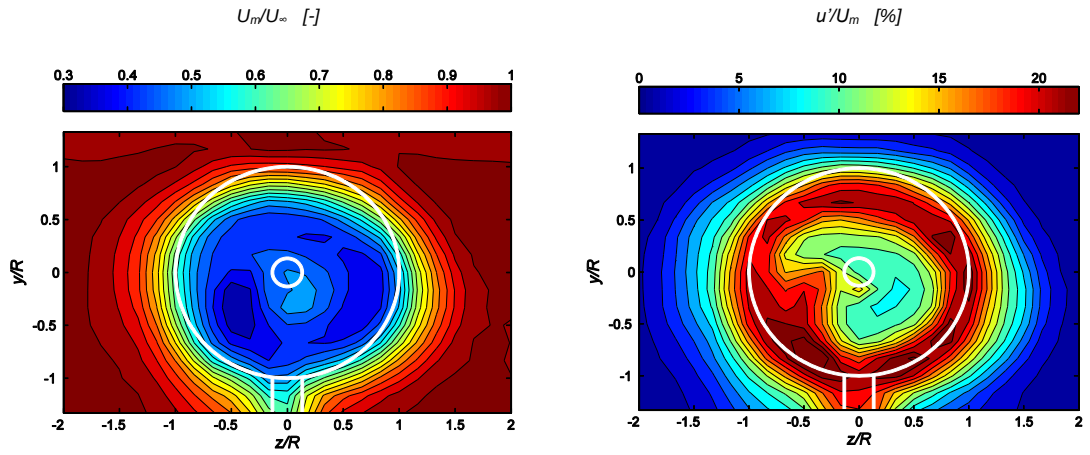

Fig. 6.16: *Velocity deficit (U_m/U_∞) and turbulence intensity (u'/U_m) in the wake 1D downstream of the second turbine operating 5D downstream of the first turbine*

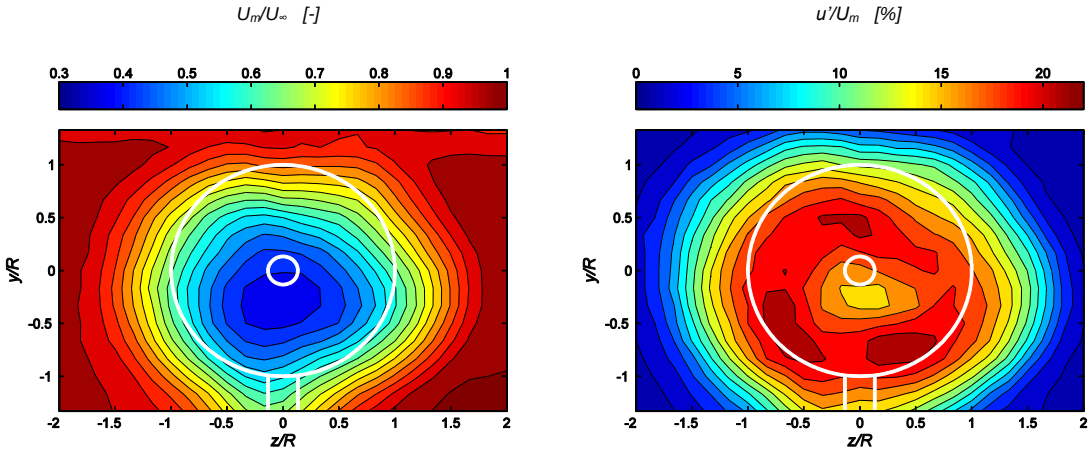

Fig. 6.17: *Velocity deficit (U_m/U_∞) and turbulence intensity (u'/U_m) in the wake 3D downstream of the second turbine operating 5D downstream of the first turbine*

Velocity deficit

Analyzing the velocity deficit in the 1D wake as depicted in *Fig 6.16*, it can be observed that the highest velocity deficit of about $U_m/U_\infty = 0.33$ can be found left underneath the center of the rotor. Behind the nacelle and the center of the rotor and the velocity deficit is only about $U_m/U_\infty = 0.50$. Further downstream in the 3D wake, the velocity deficit decreases to a minimum of $U_m/U_\infty = 0.38$. The area of the highest velocity deficit is located a little underneath the center of the rotor.

Wake dimensions

Discussing the wake velocity profile, the 1D wake has a horizontal expansion from $z/R = -1.75$ to $z/R = 1.75$ while in vertical direction it only extends about $y/R = 1.2$. As observed before, the blockage effect of the traverse system on the wind tunnel roof prevents the wake from spreading in vertical direction at the same rate as in horizontal direction. Moving downstream to 3D, the wake expands, especially in horizontal direction. Much weaker velocity gradients can be found in the 3D wake. Fluid of higher kinetic energy slowly diffuses towards the center of the wake. Thus, the area affected by a high velocity deficit diminishes moving downstream in the wake.

In this case the vertical growth rate is only about 70% of the growth rate in horizontal direction, which is even less as the 85% found by Adaramola and Krogstad [33]. The minor velocity deficit near the wind tunnel roof due to the blockage effect of the traverse system has already been observed in the mapping of the wind tunnel inflow velocity as described in *chapter 6.1*.

Again, a certain downshift of the center of highest velocity deficit is found in the 3D wake. As explained before, the blockage due to the traverse system is assumed to cause this displacement.

Wake asymmetries

High velocity deficits are dominating the area behind the rotor swept area in the 1D wake. In the center of the wake the areas of high velocity deficit are not evenly distributed around the circumference. The highest velocity deficit is found left underneath the center

of the wake. As clarified before, these asymmetries are assumed to stem from the influence of the turbine tower. Analyzing the 3D wake, the velocity distribution in center of the wake becomes more symmetrical due to diffusion processes.

Turbine tower influence

The counter-clockwise rotating turbine rotor is inducing a clockwise rotation of the flow in the wake behind the rotor. Due to the clockwise rotation of the wake, the flow is hitting the tower at a certain angle, deflecting the flow field behind the tower a little bit to the left. This phenomenon can be clearly seen at the lower edge of the velocity field in the 1D as well as the 3D wake. Besides an asymmetrical wake width at the lower edge of the 1D and 3D wake, a clear deflection of the tower wake around $z/R = 0$ can be observed. As stated before, this conclusion is in accordance with Nygard's [36] findings.

Turbulence intensities

The turbulent shear layer, which is formed by the blade tip vortices, becomes visible in a distinct ring of high turbulences of approximately $u'/U_m = 20\%$ in the 1D wake as shown in *Fig. 6.16*. Around six to seven cores very high turbulence intensities can be found unevenly distributed around the circumference. In the center of the wake both cores of rather high and relatively low turbulence intensities can be found resulting in a very non-uniform turbulence distribution. There is a core of comparatively low turbulence of about $u'/U_m = 7\%$ on the right of the rotor center. A little left of the rotor center, however, higher turbulence intensities of about $u'/U_m = 17\%$ can be found.

The 3D wake as shown in *Fig. 6.17* can be characterized by only three cores of high turbulence intensities above $u'/U_m = 20\%$. The turbulence level in the center of the wake is increased to about $u'/U_m = 13\%$. The regions of high and low turbulence intensity have mixed into a more symmetrical wake. However, the wake is not yet fully developed at 3D, as the center of the wake still features lower turbulence intensity levels as the ring surrounding it. As observed in the velocity profiles, the gradients of the turbulence intensity become weaker and the wake becomes broader 3D downstream of the second turbine.

6.5 Comparison of Turbine Arrangements (A), (B) and (C)

In this chapter, the results attained from the different experimental setups, which have been presented in the previous chapters, are compared and discussed. As shown in *Fig. 6.18* the performance curves and the wakes 1D and 3D downstream of the second model wind turbine are compared, for three different experimental setups: (A) the unobstructed second turbine, (B) the second turbine operating 3D downstream of the first turbine and (C) the second turbine operating 5D downstream of the first turbine.

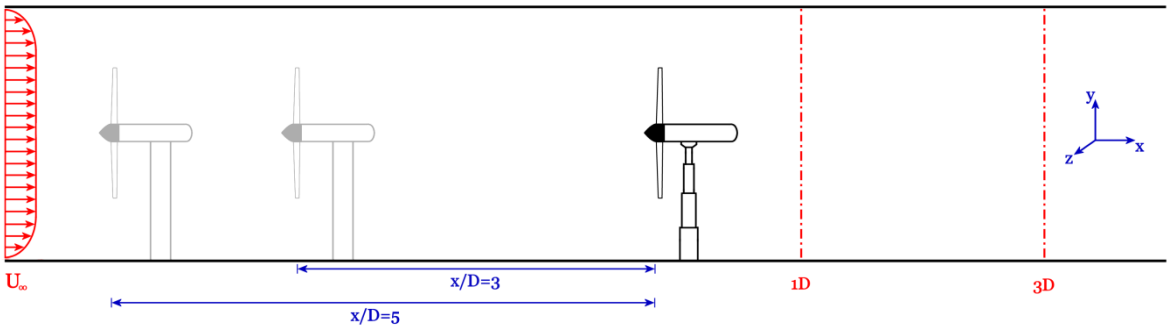

Fig. 6.18: *Comparison of the performance curves and the wakes 1D and 3D downstream of the second turbine, when the turbine is (A) unobstructed, (B) operating 3D downstream of the first turbine and (C) operating 5D downstream of the first turbine*

The second model wind turbine has different performance characteristics when operating unobstructed or in different separation distances x/D behind an upstream turbine. Thus, the power curve acquired for the unobstructed second turbine and the second turbine operating $x/D = 3$ respectively $x/D = 5$ rotor diameters downstream are different. The first turbine is operated at its maximum power point of $C_{P,max,Tu1} = 0.42$ at a tip speed ratio of $\lambda = 5.5$ for the turbine arrangements (B) and (C). Also, the second model wind turbine is operated at its maximum power point, which is different for each turbine arrangements (A), (B) and (C).

The 1D wake and the 3D wake of the turbine arrangements (A), (B) and (C) are discussed comparing the wake profiles measured in a horizontal line in hub height. These analyzes are complemented by a comparison of the full area wakes recorded for the turbine arrangements (B) and (C).

As it is not possible to record the 5D wake for turbine arrangement (C) due to space limitations, a comparison of the of the horizontal line wake measurements at 5D is only made for arrangements (A) and (B).

6.5.1 Turbine Performance Curves

A comparison of the C_P curve of the second turbine operating (A) unobstructed as well as (B) in the wake 3D and (C) 5D downstream of an upstream turbine is presented in *Fig. 6.19.* The upstream turbine (Tu1) is operating at its maximum C_P in all three cases. *Fig. 6.19 (a)* shows the C_P curves of all three turbine arrangements referred to the wind tunnel inflow speed U_∞ whereas *Fig. 6.19 (b)* relates the three C_P curves to different reference velocities.

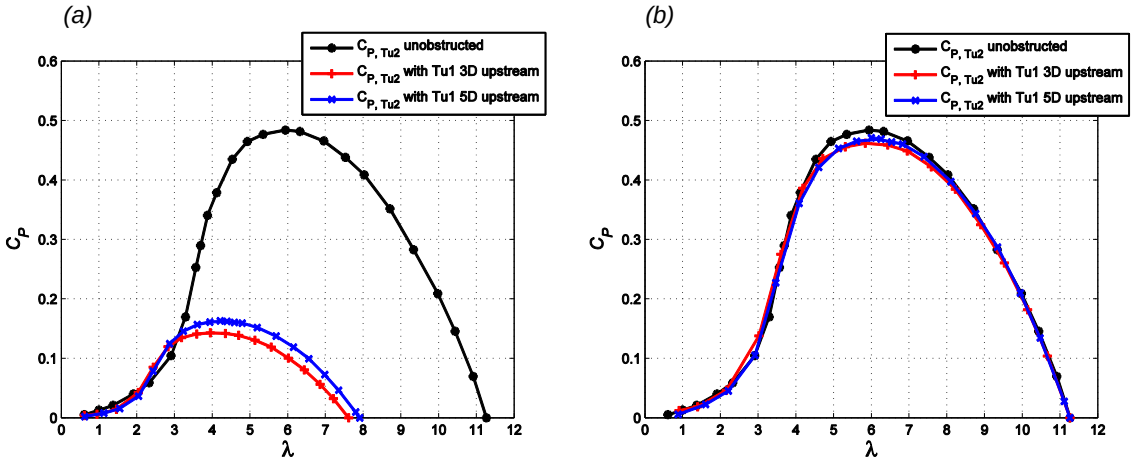

Fig. 6.19: *C_P curve of the second turbine operating (A) unobstructed, (B) 3D and (C) 5D downstream of the first turbine:*
(a) reference velocity U_∞=11.5 m/s (b) reference velocity $U_{ref,3D}$=7.8 m/s and $U_{ref,5D}$=8.1 m/s

In *Fig. 6.19 (a)* all three power curves are referred to the wind tunnel inflow velocity $U_\infty = 11.5\ m/s$. In case the second turbine is operated in the wake 3D downstream, it has a maximum power coefficient of $C_{P,max,3D} = 0.15$. That corresponds to about 31% of the power extracted of the unobstructed turbine.

When operated in the wake 5D downstream, the second turbine reaches a maximum power coefficient of $C_{P,max,5D} = 0.16$, which corresponds to about 33% of the power the unobstructed turbine extracts from the wind. The kinetic energy in the flow in the wake has consequently recovered from 3D to 5D, although the recovery rate is very small.

As the second turbine is subjected to a considerably lower kinetic energy when operating wake 3D respectively 5D downstream, the performance curves of the turbine operating in the wake are referred to lower reference velocity $U_{ref,3D}$ respectively $U_{ref,5D}$ as depicted in *Fig. 6.19 (b).* As explained before, the reference velocities are chosen that the 3D and 5D power curves are stretched to the run-away tip speed ratio of the unobstructed second

turbine. It can be observed, that the 3D and 5D power curves are fully developed and match very well with the curve of the unobstructed turbine. The maximum C_P values of the stretched curves are just insignificantly lower than the maximum C_P of the unobstructed turbine.

As stated before, it can be seen that second wind turbine operating in a turbulent flow in the wake of an upstream turbine has similar operating characteristics as the unobstructed turbine. Regardless of the downstream distance, the power curves are fully developed and reach a similar efficiency as the unobstructed turbine.

6.5.2 Downstream Flow Field

6.5.2.1 1D Wake

The velocity deficit U_m/U_∞ [-] and the turbulence intensity u'/U_m [%] in the wake 1D downstream of the second turbine are compared for the three different cases (A), (B) and (C) in *Fig. 6.20*. The second model wind turbine is operated at its maximum power point, which is different for each setup: $C_{P,max,A} = 0.47$, $C_{P,max,B} = 0.15$ and $C_{P,max,C} = 0.16$.

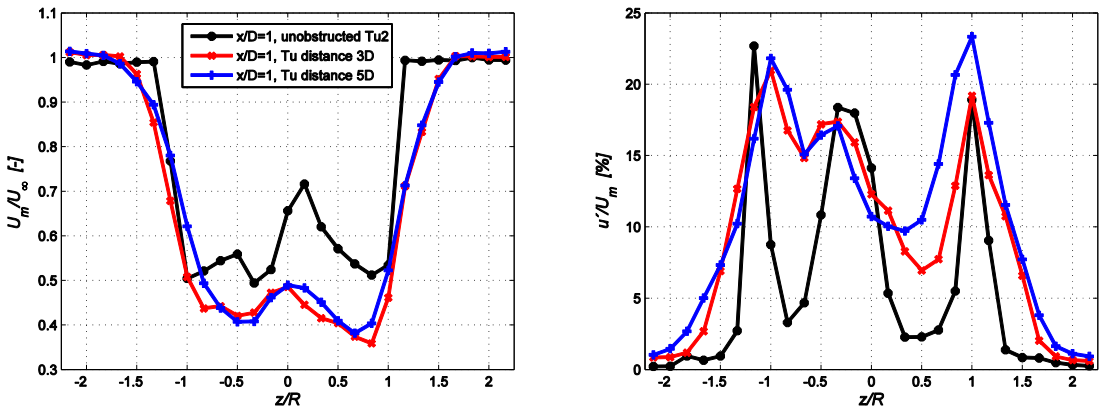

Fig. 6.20: *Velocity deficit (U_m/U_∞) and turbulence intensity (u'/U_m) in the wake 1D downstream of the second turbine operating (A) unobstructed, (B) 3D and (C) 5D downstream of the first turbine*

Velocity deficit

Comparing the velocity deficit of the three different configurations in the 1D wake, it can be observed that the velocity deficit behind two turbines is considerably higher than behind one unobstructed turbine. As the second turbine extracts additional kinetic energy from the fluid, the highest velocity deficit is found for configuration (B). A minimum mean velocity of $U_m = 4.3\ m/s$, corresponding to a velocity deficit of $U_m/U_\infty = 0.36$, is found at $z/R = 0.8$.

When operating 5D downstream of the first turbine (C) the minimum velocity deficit increases to $U_m/U_\infty = 0.38$ as more kinetic energy is recovered between the two turbines.

In the unobstructed case (A), the minimum velocity deficit amounts $U_m/U_\infty = 0.49$, which is significantly higher. Conversely, this means that the mean velocity U_m additionally decreases between 11% and 13% of the inflow velocity U_∞ when a second wind turbine is set up 5D respectively 3D behind the first turbine.

Wake dimensions

Analyzing the velocity profiles in the 1D wake of the three different configurations, it can be observed that all three profiles have approximately the same velocity deficit of $U_m/U_\infty = 0.50$ at $z/R = \pm 1$. The higher kinetic energy losses in the center of the wake for configurations (B) and (C) can be attributed to the presence of a second energy extracting turbine. Furthermore, it can be observed that the wake is significantly broader for configurations (B) and (C). The unobstructed configuration (A) can be characterized by sharp edges from $z/R = \pm 1$ to $z/R = \pm 1.2$, whereas the 1D wakes for configurations (B) and (C) feature a smoother shape outside the rotor swept area. The additional losses in kinetic energy between $z/R = \pm 1$ and $z/R = \pm 1.6$ can be ascribed to the influence of the wake of the first turbine (Tu1).

Wake asymmetries

Obvious asymmetries can be found in the 1D velocity deficit profile of the unobstructed turbine (A). Three distinct unevenly distributed minima and significant variations in velocity deficit can be observed in the center of the wake. Analyzing the velocity deficit

profiles of configuration (B) and (C) however, a much smoother and more symmetrical shape can be found. The center of the 1D wake can be characterized by only two minima and a local maximum at $z/R = 0$.
In the unobstructed configuration (A) a rather laminar inflow is hitting the rotor. Due to the rotating motion of the flow in the wake, the wake behind the turbine tower is deflected and causes significant asymmetries. In case the second turbine is operating in the wake of an upstream turbine however, it is subjected to a highly turbulent inflow. The increased turbulence levels accelerate the mixing process in the wake, which leads to a smoother and more symmetrical velocity distribution as found for cases (B) and (C).

Turbulence intensities

Comparing the turbulence intensity profiles in the 1D wake for the three different configurations, a number of similarities stick out. All three turbulence profiles are characterized by three distinct maxima, of which the ones at $z/R = \pm 1$ can be ascribed to the vortices shed at the blade tips. The central maximum is located at $z/R = -0.3$ and can be attributed to the root vortices interacting with the flow around the nacelle.
Analyzing the center of the wake, however, an overall increase in turbulence intensity for configurations (B) and (C) becomes apparent. Although the maxima feature similar turbulence intensity levels as in the unobstructed configuration, the space between the distinct vortex structures is characterized by higher turbulences. As the inflow to the rotor is already very turbulent in the arrangements (B) and (C), the turbulence intensities seem to add up in these regions.
As observed in the velocity profiles, the 1D turbulence intensity profiles are significantly broader for the configurations (B) and (C). Turbulent structures, which stem from the first turbine wake, are assumed to be responsible for this phenomenon.

The full area wake measurements of the 1D wake for the second wind turbine operating (B) 3D respectively (C) 5D downstream of the first turbine are compared in *Fig. 6.21* and *Fig. 6.22*.

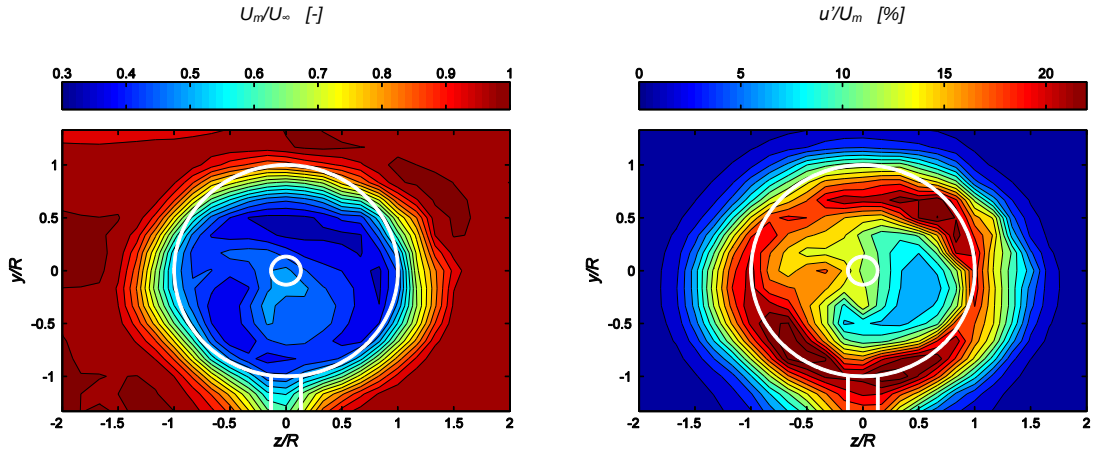

Fig. 6.21: *Velocity deficit (U_m/U_∞) and turbulence intensity (u'/U_m) in the wake 1D downstream of the second turbine operating 3D downstream of the first turbine (B)*

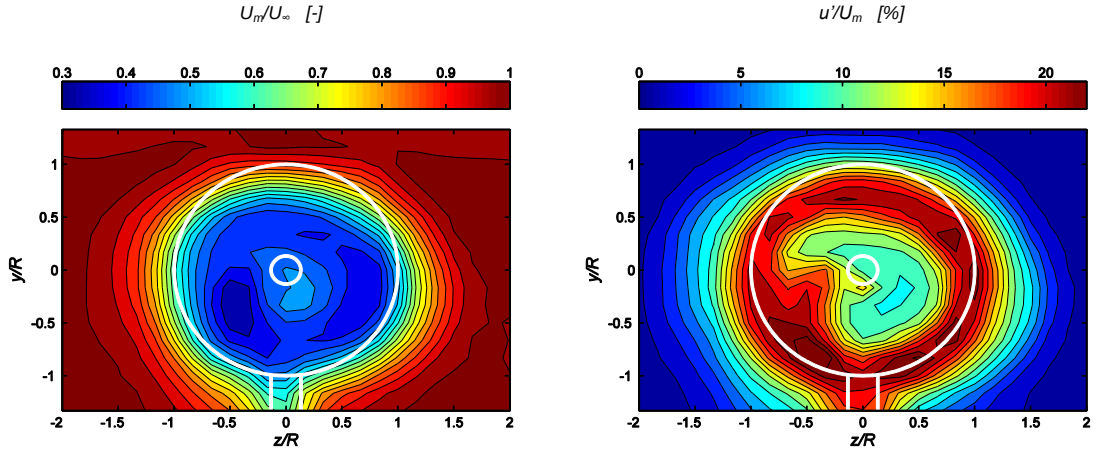

Fig. 6.22: *Velocity deficit (U_m/U_∞) and turbulence intensity (u'/U_m) in the wake 1D downstream of the second turbine operating 5D downstream of the first turbine (C)*

Inner wake

Comparing the velocity contour plots, very similar structures in the center of the wake are noticeable. A region of lower velocity deficits of approximately $U_m/U_\infty = 0.50$ can be found in the center of both wakes surrounded by some cores of higher velocity deficits down to $U_m/U_\infty = 0.35$. Remarkably, the locations of the cores of higher and lower velocity deficits match quite well for the two different wake recordings. The high deficit core in the left lower half of the rotor swept area as well as the tapering of the lower velocity core to left upper half can be found in both velocity plots.

A similar picture is given by the turbulence intensity plots. Obviously, the cores of very high turbulence intensities of more than $u'/U_m = 20\%$ can be found in almost the same

locations for both turbine separation distances. The cores of high turbulence intensity can be found in a ring behind the blade tips in the lower half and the right upper half of the rotor swept area. For both configurations (B) and (C) a similarly shaped core of comparatively low turbulence intensities is found in the center of the wake.
It is therefore assumed that the flow structures in the center of the wake (e.g. in the wake behind the rotor swept area) are predominately governed by the rotational motion of the second turbine rotor. The influence of the first turbine and the turbine separation distance is insignificant in the center of the wake.

Outer wake

When comparing the dimensions of the 1D wake outside the rotor swept area, however, the influence of the separation distance to the first wind turbine becomes evident. When the turbine separation distance is increased to 5D as done in configuration (C), the wake is visibly broader. This can be observed in the velocity deficit plots as well as the turbulence intensity plots. Referring to the turbulence intensity plots, the 1D wake is about $\Delta z/R = 3.5$ rotor diameters broad for a turbine separation distance of 3D (B) whereas it covers almost $\Delta z/R = 4.0$ rotor diameters for the 5D configuration (C). The radial widening of the first turbine wake with increasing axial downstream distance is assumed to be the cause for this phenomenon.

6.5.2.2 3D Wake

The results of the horizontal line measurements 3D downstream of the second turbine are compared for the three different cases (A), (B) and (C) in *Fig. 6.23*. In the same way as before, the second turbine is operated at its maximum power point.

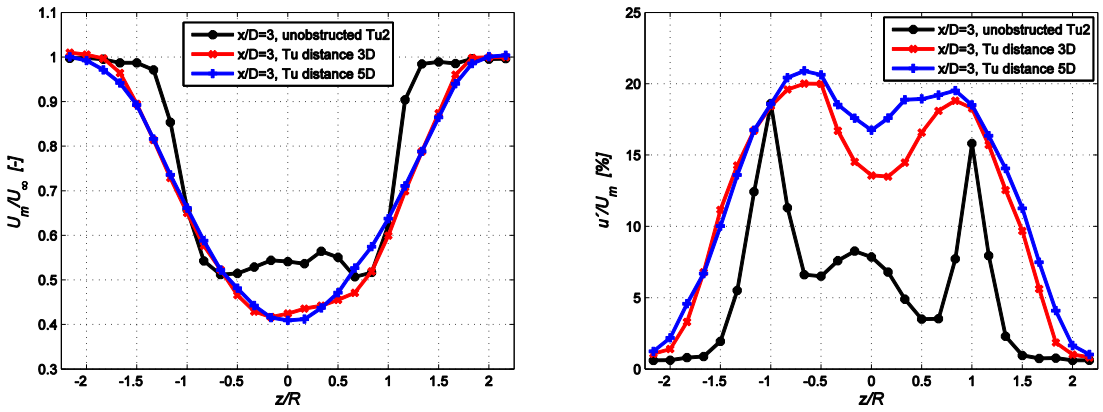

Fig. 6.23: *Velocity deficit (U_m/U_∞) and turbulence intensity (u'/U_m) in the wake 3D downstream of the second turbine operating (A) unobstructed, (B) 3D and (C) 5D downstream of the first turbine*

Velocity deficit

Similar to the findings made for the 1D wake, the velocity deficit in the 3D wake behind two turbines is found to be significantly higher than behind one unobstructed turbine. This is because the additional extraction of kinetic energy from the wind by the second turbine. The second turbine being located 3D downstream (B), a fully developed wake profile with a minimum velocity deficit of about $U_m/U_\infty = 0.42$ is found. For the 5D downstream configuration (C) the minimum velocity deficit amounts $U_m/U_\infty = 0.41$. In case the second turbine is operated unobstructed (A), the minimum velocity deficit amounts only about $U_m/U_\infty = 0.51$. Consequently, the presence of a second wind turbine causes an additional decrease in mean velocity U_m between 9% and 10% referred to the wind tunnel inflow speed U_∞.

Wake dimensions

As noticed before for the 1D wake, also the 3D wake profiles have approximately the same velocity deficit of $U_m/U_\infty = 0.65$ at $z/R = \pm 1$. Apart from the significantly higher velocity deficit behind the rotor for configurations (B) and (C), also the 3D wake is noticeably broader for these configurations. The presence of an upstream turbine is responsible for smoother velocity gradients outside the rotor area in contrast to the sharp velocity gradients of the unobstructed configuration (A). The additional losses in kinetic energy for configurations (B) and (C) between $z/R = \pm 1.0$ and $z/R = \pm 2.0$ can therefore be ascribed to a reduced inflow velocity that stems from the first turbine wake.

Wake asymmetries

The velocity profile in the 3D wake behind the single unobstructed turbine (A) can be characterized by obvious asymmetries behind the rotor swept area. For turbine arrangement (B) and especially for configuration (C) very smooth, almost symmetrical velocity profiles are found. When the second turbine is operated in the wake of an upstream turbine, the velocity profiles are fully developed at 3D downstream. Only one distinct minimum close to $z/R = 0$ is observed for configurations (B) and (C). Being subjected to a very turbulent inflow, the turbulent mixing processes in the wake behind the second turbine are accelerated that a Gaussian shaped profile is already developed in the 3D wake.

Turbulence intensities

Analyzing the turbulence intensity profiles of the different configurations in the 3D wake, the turbulence levels for the turbine arrangements (B) and (C) are significantly increased compared to the unobstructed configuration (A). Especially in the center behind the rotor swept area, the turbulence intensities are approximately double as high as for the unobstructed single turbine. As the inflow to the second rotor is already very turbulent in configurations (B) and (C), additional turbulence is added by the second turbine rotor.
The 3D turbulence profile of the unobstructed turbine (A) still can be characterized by two distinct peaks at $z/R = \pm 1$ that stem from the tip vortices. An additional peak in the center

of the wake caused by the root vortices can be found. In configurations (B) and (C), however, only two peaks are found at $z/R = \pm 0.75$. Due to the increased turbulence in these setups, the more intense diffusion processes have transported the peaks towards the center of the wake already at 3D downstream distance.

As observed in the 1D wake, the 3D turbulence intensity profiles for the configurations (B) and (C) are significantly broader than for the unobstructed arrangement (A). The turbulent shear layer in the wake of the first wind turbine mixes with the second turbine wake and thereby broadens the area of increased turbulent levels.

The results attained from the full area wake measurements of the 3D wake for the second wind turbine operating (B) 3D respectively (C) 5D downstream of the first turbine are compared in *Fig. 6.24* and *Fig. 6.25*.

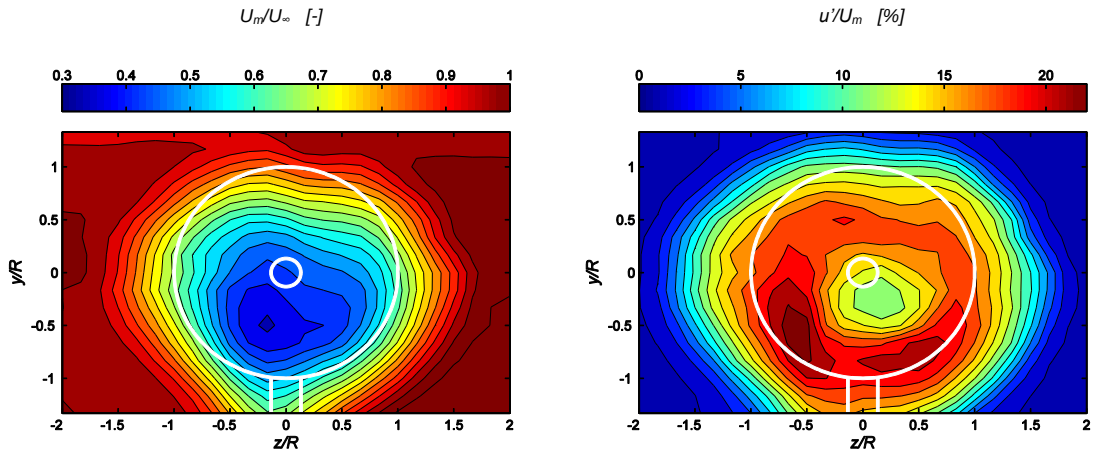

Fig. 6.24: *Velocity deficit (U_m/U_∞) and turbulence intensity (u'/U_m) in the wake 3D downstream of the second turbine operating 3D downstream of the first turbine (B)*

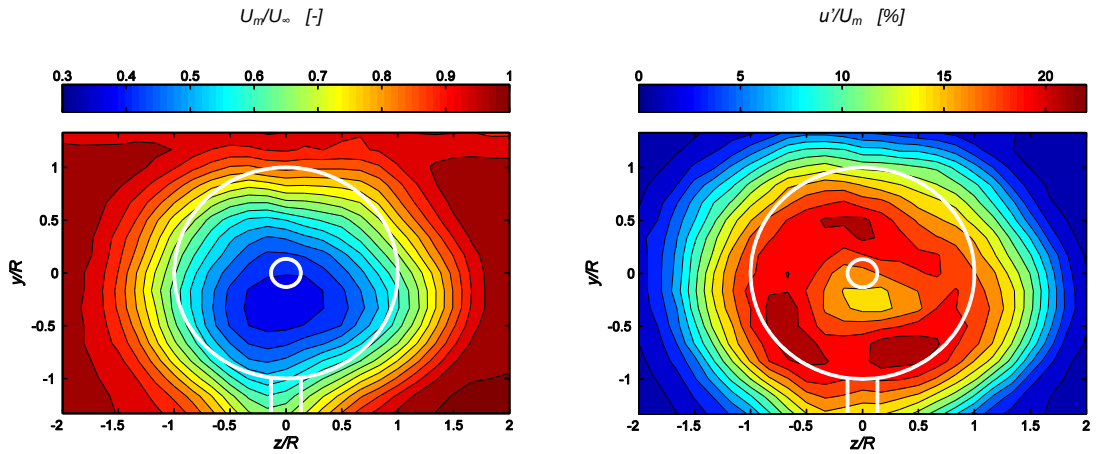

Fig. 6.25: *Velocity deficit (U_m/U_∞) and turbulence intensity (u'/U_m) in the wake 3D downstream of the second turbine operating 5D downstream of the first turbine (C)*

Inner wake

Comparing the 3D velocity contour plots of configurations (B) and (C), similar circular structures in the center of the wake are found. Although the center of the wake is slightly deflected to the left side in configuration (B), the general picture in both configurations is very similar. Both wakes are characterized by one single minimum and smooth velocity gradients.

Also, the turbulence intensity plots of the two different configurations show a very similar picture. Three cores of rather high turbulence intensity levels of more than $u'/U_m = 20\%$ are found for both turbine arrangements. Remarkably, the cores are located in approximately the same spots behind the rotor swept area for both configurations. The center of the wake is characterized by comparatively low turbulence intensities between $u'/U_m = 12\%$ and 14%.

Similarly to the 1D wake plots, the inner part of the 3D wake is predominately governed by the second turbine rotor. Hardly any influence of the turbine separation distance is found in the center of the wake.

Outer wake

As seen in the 1D wake, the influence of the separation distance to the first wind turbine becomes evident when comparing the dimensions of the 3D wake outside the rotor swept area. The dimensions of the 3D wake are visibly bigger, when the turbine separation distance is increased to 5D as done in configuration (C). A comparison of the two velocity deficit plots as well as the two turbulence intensity plots allows the same conclusion. In turbine configuration (B) the 3D wake is about $\Delta z/R = 4.0$ rotor diameters broad whereas it covers estimated $\Delta z/R = 4.5$ rotor diameters in configuration (C) when comparing the turbulence intensity plots.

As the first turbine wake is growing in radial direction with increasing downstream distance, these observations are assumed to be significantly influenced by the first turbine wake.

6.5.2.3 5D Wake

The velocity deficit U_m/U_∞ [-] and the turbulence intensity u'/U_m [%] in the wake 5D downstream of the second turbine are compared for the turbine configurations (A) and (B) in *Fig. 6.26*. For turbine arrangement (C) it is not possible to acquire any data for the 5D wake due to a limited length of the wind tunnel. The second model wind turbine is operated at its maximum power point for both configurations.

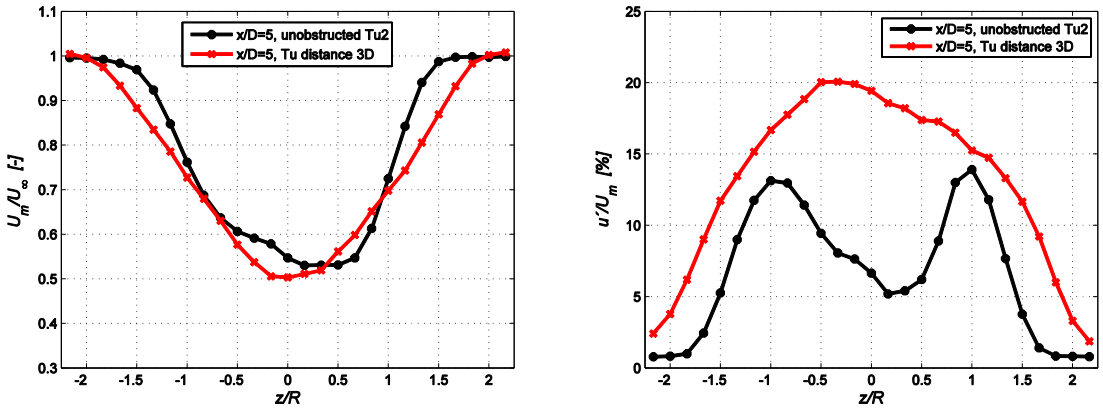

Fig. 6.26: *Velocity deficit (U_m/U_∞) and turbulence intensity (u'/U_m) in the wake 5D downstream of the second turbine operating (A) unobstructed and (B) 3D downstream of the first turbine*

Velocity deficit

Comparing the minimal velocity deficit of unobstructed second turbine (A) and the second turbine as operating in the 3D wake (B), only a rather minor difference can be found. The minimal velocity deficit of $U_m/U_\infty = 0.50$ for configuration (B) is only a slightly smaller than for the unobstructed configuration (A), in which a minimum velocity deficit of $U_m/U_\infty = 0.53$ can be found. Still, the extraction of additional kinetic energy from the wind of a second turbine is evident in the 5D wake. However, in the 5D wake the difference in mean velocity U_m between the two configurations reduces down to only 3% referred to the inflow speed U_∞. This is significantly less than a difference of 13% and 9% found in the 1D respectively the 3D wake.

Wake dimensions

Apart from the slightly higher velocity deficit behind the rotor in turbine configuration (B), also the 5D wake is significantly broader in this configuration. The wake of the upstream turbine causes the additional losses in kinetic energy for configuration (B) between $z/R = \pm 1.0$ and $z/R = \pm 2.0$. As observed for the 1D and 3D wake profiles, also the different 5D wake profiles have a similar values of velocity deficit at $z/R = \pm 1$.

Wake asymmetries

The velocity profile of the unobstructed turbine (A) still features evident asymmetries 5D behind the rotor swept area. The 5D wake profile for configuration (B), however, is almost perfectly symmetrical. A symmetrical shaped profile is fully developed at 5D due to the turbulent inflow accelerating the mixing processes in the wake.

Turbulence intensities

The turbulence intensity levels in turbine arrangement (B) are visibly increased in comparison to the unobstructed configuration (A). A maximum turbulence intensity of $u'/U_m = 20.0\%$ can be found for arrangement (B) compared to $u'/U_m = 13.9\%$ in arrangement (A). Especially in the center behind the rotor swept area, the turbulence intensities are more than double as high as for the unobstructed turbine. Additional turbulence is added by the second turbine rotor to the already very turbulent inflow in configuration (B).

The 5D turbulence profile of the unobstructed turbine (A) is characterized by two distinct peaks at $z/R = \pm 1$ that stem from the tip vortices. In configuration (B), however, only one peak in turbulence intensity is found in the center of the wake. Also the turbulence intensity profile is fully developed. As observed in the 1D and 3D wake, the 5D turbulence intensity profile for the configuration (B) is considerably broader as for the unobstructed arrangement (A). The broader wake in arrangement (B) can be ascribed to the turbulent shear layer in the wake of the first wind turbine mixing into the second turbine wake.

6.6 Variations in Tip Speed Ratio

In the final test series the influence of variations in the tip speed ratio λ of both turbines on the flow field in the wake is investigated. The separation distance between the two turbines is fixed to $x/D = 3$ rotor diameters for this test series. Turbine performance curves and wake profiles are recorded for different tip speed ratio combinations of the two turbines. The experimental setup and the one probe measurement station are sketched in *Fig 6.27*.

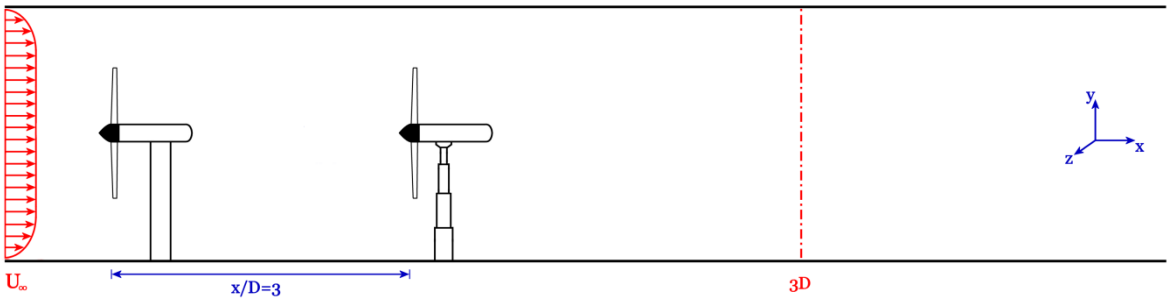

Fig. 6.27: *Experimental setup and axial probe measurement station for the investigation of the effect of turbine tip speed ratio variations*

Firstly, three C_P curves of the second turbine are recorded for three different operating points of the first turbine. At the optimum operation point of the first turbine ($\lambda = 5.5$), the power curve of the second turbine is acquired again. Thereafter, second turbine C_P curves for a low rotational speed ($\lambda = 3.0$) and a high rotational speed ($\lambda = 9.0$) of the first turbine are recorded.

Finally, wake profiles are measured in a horizontal line at hub height 3D downstream of the second turbine. Altogether, nine different tip speed ratio combinations of the two turbines are investigated. At first, the tip speed ratio of the first turbine is kept constant while the tip speed ratio of the second turbine is varied to three different operating points. Thereafter, three different tip speed ratios of the first turbine are set while the rotational speed of the second turbine is kept constant. That results in nine horizontal line wake measurements as presented in *Table 6.1*. The nine wake measurements are from here on referred to as “Case 1” to “Case 9”.

	TSR first turbine	TSR second turbine
Case 1 (Reference Case)	**optimal** ($\lambda = 5.5$) *1350 rpm*	**optimal** ($\lambda = 4.0$)* *1000 rpm*
Case 2	**optimal** ($\lambda = 5.5$) *1350 rpm*	**low** ($\lambda = 2.0$) *500 rpm*
Case 3	**optimal** ($\lambda = 5.5$) *1350 rpm*	**high** ($\lambda = 6.0$) *1500 rpm*
Case 4	**low** ($\lambda = 3.0$) *750 rpm*	**optimal** ($\lambda = 4.2$) *1020 rpm*
Case 5	**low** ($\lambda = 3.0$) *750 rpm*	**low** ($\lambda = 2.0$) *500 rpm*
Case 6	**low** ($\lambda = 3.0$) *750 rpm*	**high** ($\lambda = 6.0$) *1500 rpm*
Case 7	**high** ($\lambda = 9.0$) *2150 rpm*	**optimal** ($\lambda = 4.6$) *1130 rpm*
Case 8	**high** ($\lambda = 9.0$) *2150 rpm*	**low** ($\lambda = 2.0$) *500 rpm*
Case 9	**high** ($\lambda = 9.0$) *2150 rpm*	**high** ($\lambda = 6.0$) *1500 rpm*

* tip speed ratio λ of the second turbine referred to the wind tunnel inflow speed U_∞

Table 6.1: *Investigated test cases with different tip speed ratios of the turbines*

6.6.1 Turbine Performance Curves

The C_P curves of the second turbine operating in the wake 3D downstream of an upstream turbine, which is operating a three different tip speed ratios, are compared in *Fig. 6.28*. The curves presented in *Fig. 6.28 (a)* are referred to the wind tunnel inflow speed U_∞. In *Fig. 6.28 (b)* the power curves are referred to different reference velocities in order to compare their shape to the C_P curve of the unobstructed turbine. For the first turbine operating at its maximum power point at $\lambda_{Tu1} = 5.5$, the power curve of the second turbine is depicted in red. The C_P curve of second turbine for a low first turbine tip speed ratio of $\lambda_{Tu1} = 3.0$ is presented in blue. The yellow curve represents the power curve for a high first turbine tip speed ratio ($\lambda_{Tu1} = 9.0$).

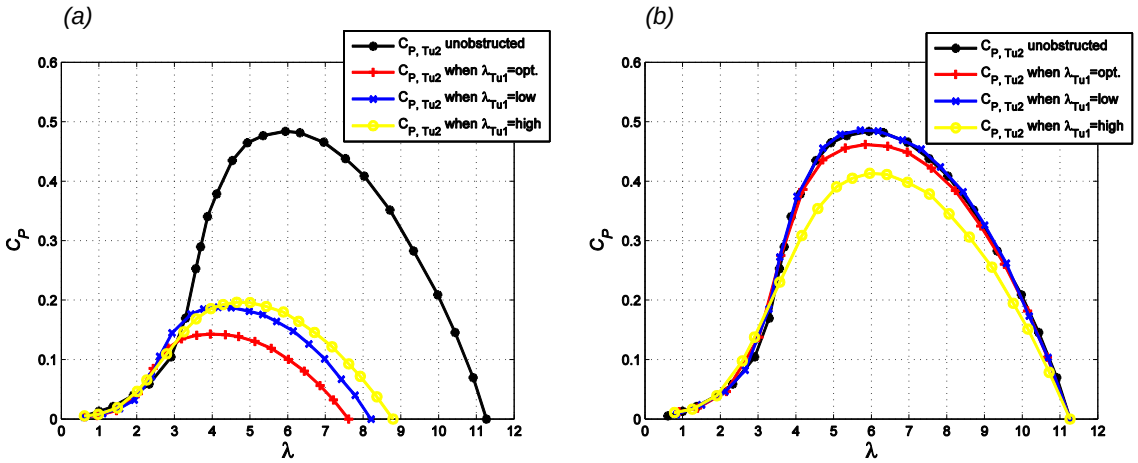

Fig. 6.28: *C_P curves of the second turbine operating in the wake 3D downstream for varying tip speed ratios of the first turbine:*
(a) reference velocity U_∞=11.5 m/s (b) $U_{ref,opt}$=7.8 m/s, $U_{ref,low}$=8.4 m/s and $U_{ref,high}$=9.0 m/s

Comparing the power curves of the second turbine in *Fig. 6.28 (a)* it can be observed that the second turbine has the lowest $C_{P,max,Tu2}$ when the first turbine is operated at its maximum power point. As the first turbine extracts the maximum possible power from the wind at $C_{P,max,Tu1} = 0.42$, only a small amount of kinetic energy is left in the wind so that the second turbine reaches a maximum power coefficient of $C_{P,max,Tu2} = 0.15$ corresponding to 31% of the power extracted from the unobstructed turbine. In case the first turbine is operated at a lower or higher than optimum tip speed ratio, the amount of kinetic energy left for the second turbine is significantly bigger. For a low tip speed ratio $\lambda_{Tu1} = 3.0$ of the first turbine only about $C_{P,low,Tu1} = 0.20$ are extracted from the first turbine. In this case the second wind turbine reaches a maximum power coefficient of $C_{P,max,Tu2} = 0.19$ corresponding to 39% of power extracted in the unobstructed case.
Likewise, the first turbine has a power coefficient of $C_{P,high,Tu1} = 0.20$ when driven at a high tip speed ratio of $\lambda_{Tu1} = 9.0$. For this setup the second wind turbine reaches a maximum power coefficient of $C_{P,max,Tu2} = 0.20$ corresponding to 41% of the power extracted from the unobstructed second turbine.
The shapes of the different C_P curves at different reference velocities are compared in *Fig. 6.28 (b)*. Being stretched to the same run-away tip speed ratio of the unobstructed case, the second turbine power curve is almost identical when the first turbine is operated at a low tip speed ratio of $\lambda_{Tu1} = 3.0$. As observed before, the operational characteristics of the second turbine operating in the wake of the first turbine at its optimum point are also

very similar to the unobstructed case. A slightly lower maximum efficiency of $C_{P,max,Tu2} = 0.46$ is reached in this case. The shape of the second turbine power curve when operated in the wake of the first turbine operated at a high tip speed ratio of $\lambda_{Tu1} = 9.0$, however, differs visibly from the unobstructed case. A maximum efficiency of $C_{P,max,Tu2} = 0.42$ is reached when being stretched to the run-away tip speed ratio of the unobstructed case.

A comparison of the combined power coefficients of both turbines for the nine different test cases is presented in *Fig. 6.29*. The black lower parts of the bars are the power coefficients of the first turbine, which is $C_{P,max,Tu1} = 0.42$ for the first three cases and $C_{P,low,Tu1} = 0.20$ for cases 4-6 respectively $C_{P,high,Tu1} = 0.20$ for cases 7-9. The power coefficients of the second turbine $C_{P,Tu2}$ constitute the upper part of the bars, which are coloured according to the power curves presented in *Fig. 6.28*.

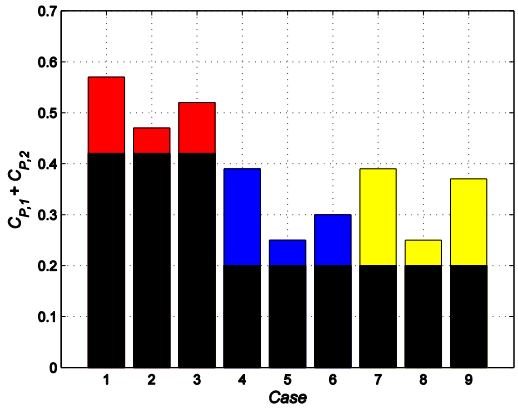

Fig. 6.29: *Combined power output ($C_{P,Tu1} + C_{P,Tu2}$) of both turbines operated in 3D distance for the nine investigated test cases*

It can be observed that the maximum combined power output is obtained for test case 1, in which both turbines are operated at their maximum power point. Comparing cases 1,4 and 7, it can be seen that the part of the power extracted by the second turbine $C_{P,Tu2}$ significantly increases, when less energy is extracted by the first turbine in cases 4 and 7.
In this specific setup, the combined power in cases 4 and 7 does, however, by far not reach the maximum extracted power of case 1.
Nevertheless, it should be noted that a variation in first turbine tip speed ratio from the optimum can lead to an increased overall power output. A comprehensive study on the wake interference effect on the performance of a downstream turbine was performed by Adaramola and Krogstad [14] at NTNU's wind tunnel. They investigated the effects of

variations in turbine separation distance x/D, first turbine yaw angle γ, first turbine pitch angle β and first turbine tip speed ratio λ_{Tu1} on the total power output from both turbines. They found a slight increase in total power output from both turbines, when the upstream turbine was operated at a slightly higher tip speed ratio than the optimum design tip speed ratio [14].

6.6.2 Downstream Flow Field

The velocity deficit U_m/U_∞ [-] and the turbulence intensity u'/U_m [%] in the wake 3D downstream of the second model wind turbine are recorded for nine different tip speed ratio combinations of the two turbines.

Firstly, the wake profiles are compared for a constant TSR of the first turbine and varying tip speed ratios of the second turbine. The 3D wake profiles for test cases 1, 2 and 3, in which the first turbine is driven at the optimum TSR, are compared in *Fig. 6.30*. *Fig. 6.31* shows the graphs acquired for a low first turbine TSR ($\lambda_{Tu1} = 3.0$) in the test cases 4, 5 and 6. The wake profiles for test cases 7, 8 and 9, which represent a high first turbine TSR ($\lambda_{Tu1} = 9.0$) are presented in *Fig 6.32*.

Thereafter, the exactly same data for the nine test cases is presented again. However, the single test cases are compared in a different order to each other as some properties of the single profiles are thus more apparent. This time, the velocity deficits and turbulence intensities in the 3D wake are compared again for varying tip speed ratios of the first turbine and a constant TSR of the second turbine. In *Fig. 6.33* the test cases 1, 4 and 7 are compared. For the optimum TSR of the first turbine, the maximum power point of the second turbine is found at $\lambda_{Tu2} = 4.0$ (case 1). When the first turbine is operated at low TSR, the second turbine maximum power point is at $\lambda_{Tu2} = 4.2$ (case 4). For a high first turbine TSR, the maximum power point of the second turbine is found at $\lambda_{Tu2} = 4.6$ (case 7). The wake profiles for the test cases 2, 5 and 8 are presented in *Fig. 6.34*. The first turbine TSR is varied, while the second turbine is constantly operated at a low TSR. Finally, *Fig. 6.35* shows the wake profiles for test cases 3, 6 and 9, which represent a varying first turbine TSR in combination with a high second turbine tip speed ratio.

Constant TSR of the first turbine, varying TSR of the second turbine

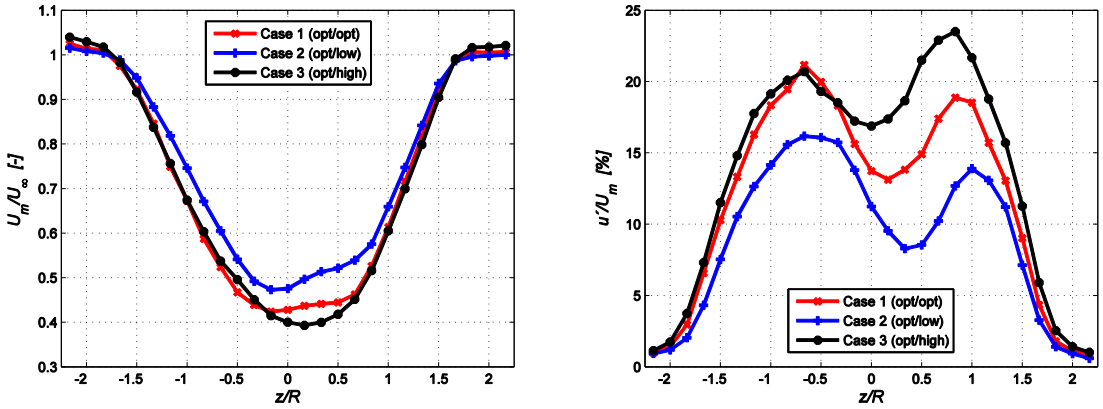

Fig. 6.30: *Velocity deficit (U_m/U_∞) and turbulence intensity (u'/U_m) in the wake 3D downstream of the second turbine for the TSR Cases 1, 2 and 3*

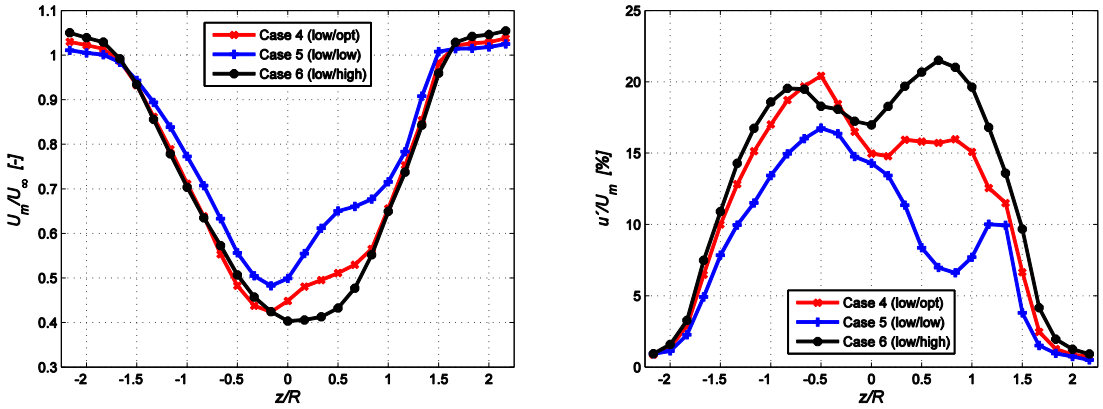

Fig. 6.31: *Velocity deficit (U_m/U_∞) and turbulence intensity (u'/U_m) in the wake 3D downstream of the second turbine for the TSR Cases 4, 5 and 6*

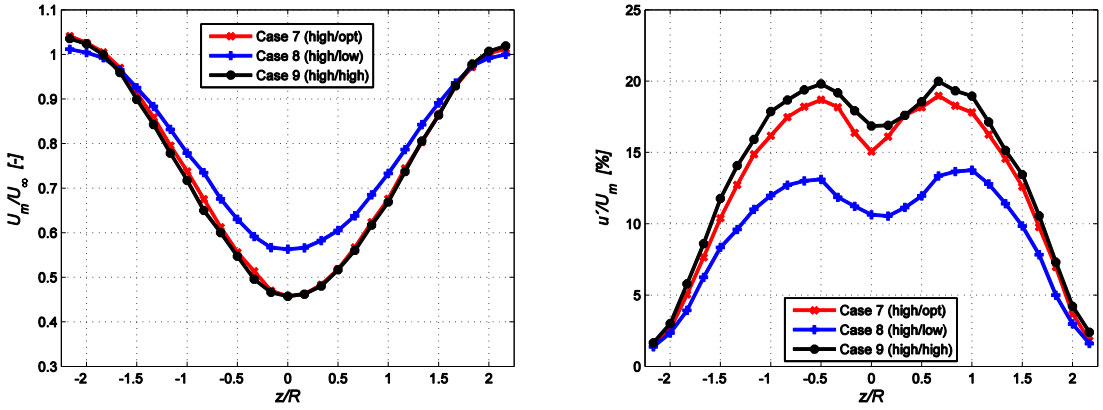

Fig. 6.32: *Velocity deficit (U_m/U_∞) and turbulence intensity (u'/U_m) in the wake 3D downstream of the second turbine for the TSR Cases 7, 8 and 9*

Varying TSR of the first turbine, constant TSR of the second turbine

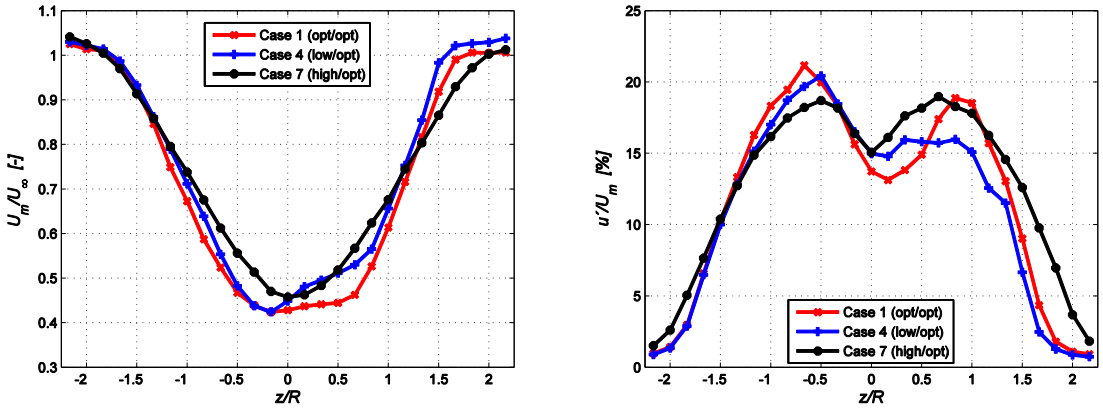

Fig. 6.33: *Velocity deficit (U_m/U_∞) and turbulence intensity (u'/U_m) in the wake 3D downstream of the second turbine for the TSR Cases 1, 4 and 7*

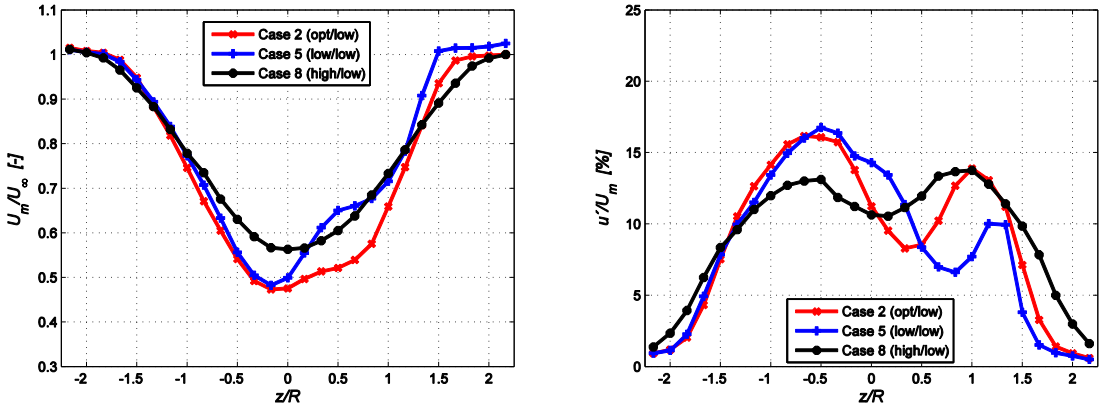

Fig. 6.34: *Velocity deficit (U_m/U_∞) and turbulence intensity (u'/U_m) in the wake 3D downstream of the second turbine for the TSR Cases 2, 5 and 8*

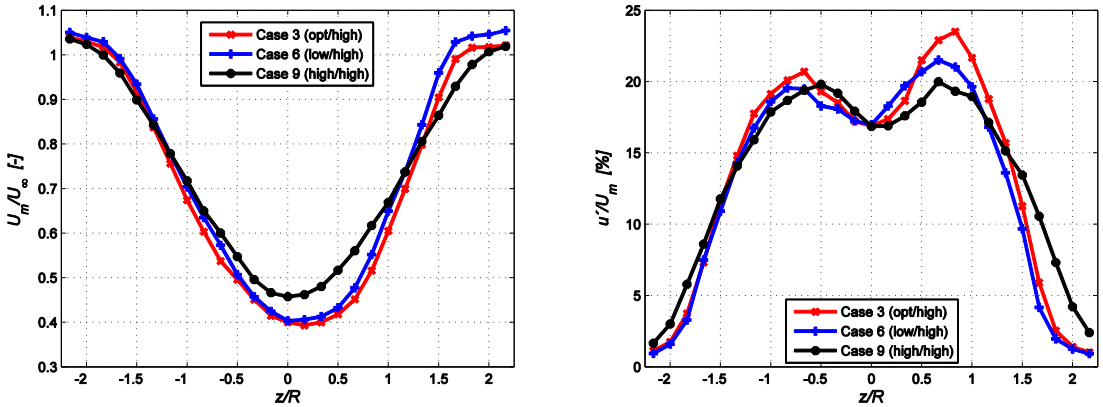

Fig. 6.35: *Velocity deficit (U_m/U_∞) and turbulence intensity (u'/U_m) in the wake 3D downstream of the second turbine for the TSR Cases 3, 6 and 9*

Velocity deficit

Comparing the minimum velocity deficit of the nine investigated test cases, the same trends can be observed in *Fig. 6.30 to 6.32*. When the first turbine tip speed ratio is kept constant, the minimum velocity deficit in the 3D wake is very dependent on the second turbine TSR. The highest velocity deficit can be found for a high tip speed ratio of the second turbine (black curves) in *Fig. 6.30*, *Fig. 6.31* and *Fig. 6.32*. A low second turbine TSR is yielding the lowest velocity deficit in all comparisons. For a high first turbine TSR as compared in *Fig. 6.32* the velocity profiles of the second turbine driven at optimum TSR (case 8) respectively high TSR (case 9) are almost identical.

When however the second turbine TSR is kept constant, an operation of the first turbine at the optimum point causes the highest velocity deficits as shown in *Fig. 6.33 to 6.35*. In these cases the maximum possible kinetic energy has been extracted by the first turbine yielding higher velocity deficits behind the second turbine. In case the first turbine is operated at high tip speed ratios, the lowest velocity deficit could be found.

A comparison of the velocity deficit values of all nine investigated test cases is presented in *Fig. 6.36* in the end of this chapter.

Freestream velocity

Analyzing the velocity profiles in a region outside of the rotor wake from approximately $z/R = \pm 1.8$ to $z/R = \pm 2.2$, the blockage effect in the wind tunnel due to the different rotational speeds of the second turbine rotor is apparent. The higher the second turbine TSR, the higher is the blockage due to the rotor swept area. Consequently, the flow that passes between the turbine rotor and the wind tunnel endwalls has a higher velocity when there is an increased blockage due to the turbine rotors. In *Fig. 6.30* to *6.32* a high second turbine TSR (black curve) causes freestream velocities up to $U_m/U_\infty = 1.05$, whereas the freestream velocities for an optimum and low TSR are always slightly lower.

Wake dimensions

Investigating the dimensions of the wake profiles, the tip speed ratio of the second turbine does not seem to have a significant influence. It is rather the influence of the first turbine TSR, which defines the width of the wake behind the array of the two model turbines.
Referring to the velocity deficit profiles, the wake is about $z/R = 3.2$ rotor radii broad for a low first wind turbine TSR (cases 4, 5 & 6). In case the first turbine is operated at optimum TSR, the wake is about $z/R = 3.5$ rotor radii broad. For a high first turbine TSR a wake width of approximately $z/R = 4.0$ rotor radii is found.
As the wake expands when moving downstream, the first turbine wake has grown a little more than the second turbine wake at the axial measurement station 3D downstream of the second turbine. Therefore, the second turbine rotational speed does not influence the width of the wake.

Wake asymmetries

Focusing on the center of the wake from $z/R = -1$ to $z/R = +1$, clear asymmetries are apparent in some of the wake profiles. The most obvious asymmetries are found for low tip speed ratios of the second turbine (cases 2 & 5). If second turbine is driven at high tip speed ratios as in cases 3, 6 and 9, however, the velocity profiles are almost symmetrical.
As explained before, the asymmetries can be ascribed to an interference of the rotation of the flow in the rotor wake and the wake of the turbine tower. The obvious asymmetries at low rotational speeds of the second turbine are assumed to be stem from a strong rotation in the rotor wake. The strength of the rotation of the flow in wake is dependent on the size of the circumferential component $U_{\theta,2}$ in the flow behind the rotor (see *Fig. 1.4*). When the turbine is rotating at a higher tip speed ratio, the circumferential component $U_{\theta,2}$ and thus the strength of the wake rotation reduces. Therefore, higher symmetries are found at high TSRs of the second turbine.
However, also the first turbine TSR seems to have a certain influence on the symmetry in the wake velocity profile. All velocity profiles as plotted in *Fig. 6.32* are almost perfectly symmetrical, although the second turbine is operated at low, optimum and high TSR (cases 7, 8 & 9). As the first turbine is driven at a high rotational speed in all three cases, it

causes increased turbulence levels in the incoming flow to the second turbine rotor. These increased turbulence levels are assumed to intensify the turbulent mixing process in the wake yielding more symmetrical profiles.

Turbulence intensities

Analyzing the turbulence intensity profiles of the nine investigated test cases, it can be observed that all profiles can be characterized by two distinct peaks. These two peaks can be ascribed to the vortices shed from the blade tips of the second turbine rotor.
The highest turbulence intensities can be found for a high tip speed ratio of the second turbine (cases 3, 6 & 9), whereas the lowest turbulence intensities are measured for low second turbine TSRs (cases 2, 5 & 8). A comparison of the maximum turbulence intensity levels found in all nine investigated test cases is presented in *Fig. 6.36* in the end of this chapter.
In most cases the peaks are deflected from their original position $z/R = \pm 1$ towards the center of the wake. At higher second turbine tip speed ratios the turbulence intensity profiles are more symmetrical than at low tip speed ratios. The highest asymmetry in a turbulence intensity profile is found for case 5, in which both the first and the second turbine are operated at low tip speed ratios. It is assumed that in this case there is a strong rotation in the flow behind the second turbine rotor and that the mixing process in the wake is weaker due to a reduced turbulence level in the incoming flow to the second rotor.
When the first turbine is operated at high tip speed ratios as in cases 7, 8 and 9, the turbulence intensity profiles are all almost symmetrical. High turbulence levels in the incoming flow are assumed to enhance the mixing process in these cases, in which high symmetries are also found in the the velocity deficit profiles.
Analyzing the wake dimension with respect to the width of the turbulence intensity profiles, the same conclusions as found for the velocity profiles can be made. The wake width is mainly influenced by the tip speed ratio of the first turbine, whereas the second turbine TSR does not have hardly any influence. High first turbine TSRs cause wider wakes profiles as observed in *Fig. 6.33* to *6.35*.

Comparison of minimum velocity deficit and maximum turbulence intensity

In *Fig. 6.36* the minimum velocity deficit $(U_m/U_\infty)_{min}$ and the maximum turbulence intensity $(u'/U_m)_{max}$ measured in the wake 3D downstream of the second turbine are compared for the nine investigated test cases.

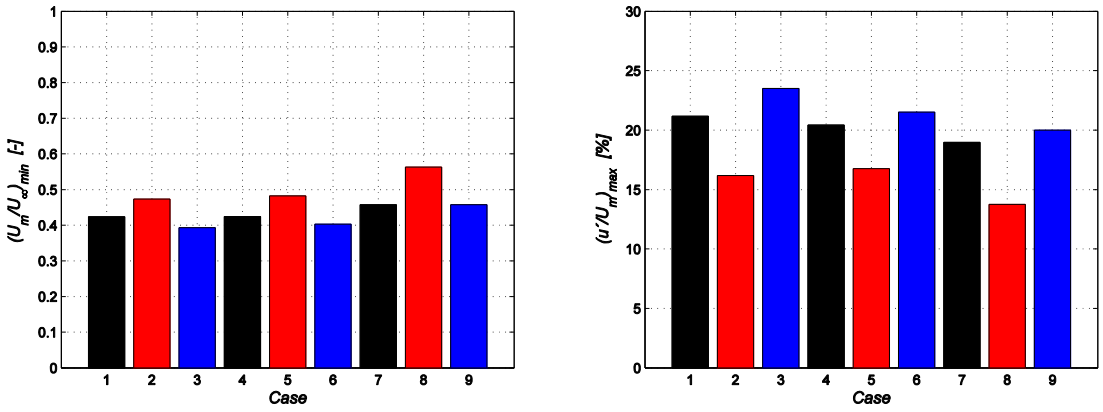

Fig. 6.36: *Comparison of the minimum velocity deficit $(U_m/U_\infty)_{min}$ and the maximum turbulence intensity $(u'/U_m)_{max}$ in the 3D wake for the nine different test cases*

Minimum velocity deficit

Comparing all nine investigated test cases, the highest velocity deficit can be found in case 3, in which the first turbine is operated at its optimum tip speed ratio and the second turbine at a high TSR. A proportion of only about $(U_m/U_\infty)_{min} = 0.39$ of the incident flow velocity can be found in the minimum of the velocity profile. Remarkably, the minimum velocity deficit is even higher as in case 1, in which both turbine are operated at optimum TSR and the most kinetic energy is extracted from the wind (see *Fig. 6.29*). The lowest value of velocity deficit is recorded for test case 8, in which the first turbine is operated at high, the second at low TSR. The minimum velocity found in the profile for case 8 corresponds to a value of about $(U_m/U_\infty)_{min} = 0.56$.

As observed before, the velocity deficit is always highest, when the second turbine is driven at high TSR and the first turbine TSR is kept constant (cases 3, 6 & 9). For a constant first turbine TSR, the lowest velocity deficit can always be found for a low second turbine TSR (cases 2, 5 & 8). When however the first turbine TSR is varied and the second turbine TSR is kept constant, the highest velocity deficits are acquired for an optimum TSR of the first turbine (comparing cases 1, 4 & 7 respectively 2, 5 &8 respectively 3, 6 & 9). In these cases (cases 1, 2 & 3) the maximum possible kinetic energy has been extracted

by the first turbine causing higher velocity deficits behind the second turbine. For the tip speed ratios set in these experiments, a low first turbine TSR yields higher velocity deficits than a high first turbine TSR (comparing cases 4 , 5 & 6 to cases 7, 8 & 9).

Maximum turbulence intensity

The highest maximum in turbulence intensity of $(u'/U_m)_{max} = 23.5\ \%$ is found in case 3, in which the first turbine is operated at optimum TSR and the second turbine at high TSR. In general, a high second turbine TSR causes high maximum turbulence levels of more than 20 % (cases 3, 6 & 9). The lowest maximum in the turbulence intensity profiles of $(u'/U_m)_{max} = 13.8\ \%$ is recorded for test case 8, in which the first turbine is operated at high TSR and the second at low TSR. It can be observed that a low second turbine TSR yields comparatively low maximum turbulence intensities (cases 2, 5 & 8). The tip vortices shed from the second turbine rotor are assumingly not as strong for higher second turbine rotational speeds.

The maximum turbulence intensities in the 3D wake behind the second turbine seem majorly to be influenced by the second turbine rotational speed. The influence of the first turbine TSR is small. Surprisingly, a high first turbine TSR as set in cases 7, 8 & 9 yields lower maximum turbulence intensities as for a low (cases 4, 5 & 6) or an optimum first turbine TSR (cases 1, 2 & 3).

Noteworthy, the maximum turbulence intensities are seemingly coupled to the minimum values of velocity deficit. High maximum turbulence intensity is observed in cases with high minimum velocity deficit and the other way round.

7 CONCLUSIONS & FUTURE WORK

7.1 Conclusions

Turbine Performance

Analyzing the performance curves of a single turbine acquired at different wind tunnel inlet speeds, a smooth shape of the curves can be observed at wind speed higher than $U_\infty = 8.5\ m/s$. At wind speeds below that, laminar separation effects in certain sections of the blades cause abnormal bumps in the power and thrust curves. For the design inflow speed of approximately $U_\infty = 11.5\ m/s$ the first model wind turbine reaches a maximum power coefficient of $C_{P,max,Tu1} = 0.42$, whereas a maximum power coefficient of $C_{P,max,Tu2} = 0.48$ is measured for the second model wind turbine, when it is operated unobstructed. As both turbines are equipped with exactly the same set of blades, the small difference in hub diameter seems to have a significant effect on the performance curves. At the maximum investigated tip speed ratio of about $\lambda = 11.0$, maximum thrust coefficients of $C_{T,max,Tu1} = 1.1$ respectively $C_{T,max,Tu2} = 1.3$ are recorded for the two turbines. The fact that these values are higher than one can be subscribed to a blockage effect by the wind tunnel endwalls.

In case the second turbine is operated in the wake of an upstream turbine, different maximum power points are found. For a turbine separation distance of $x/D = 3$ the second turbine reaches a maximum power coefficient of $C_{P,max,3D} = 0.15$. That corresponds to about 31% of the power extracted of the unobstructed turbine. When operated in the wake 5D downstream, the second turbine has a maximum power coefficient of $C_{P,max,5D} = 0.16$, which corresponds to about 33% of the power the unobstructed turbine extracts from the wind. Comparing the shapes of the power curves at proportioned reference velocities, it can be observed that the second turbine operating in the wake has very similar operating characteristics as the unobstructed turbine. For both investigated downstream distances, the power curves are fully developed and reach a similar efficiency as the unobstructed turbine.

Axial development of the wake velocity deficit

Evaluating the axial development of the velocity deficit in the wake, similar conclusions can be drawn for all investigated turbine arrangements. Moving downstream in the wake behind one single turbine or an array of two turbines, the velocity deficit recovers with increasing downstream distance. Comparing the velocity deficit in the wake of the three investigated configurations, it can be observed that the velocity deficit behind an array of two turbines is considerably higher than behind one unobstructed turbine. The highest velocity deficit is found for a small turbine separation distance of $x/D = 3$, as the second turbine extracts additional kinetic energy from the fluid. In case the separation distance between the turbines is increase to $x/D = 5$, the minimum velocity deficit increases slightly. More kinetic energy is recovered between the two turbines. The additional decrease in minimum mean velocity in the 1D wake ranges between 11% and 13%, if a second turbine is set up 5D respectively 3D downstream of the first turbine.
Furthermore, a gentle broadening of the wake can be observed for all configurations when moving axially downstream. As the turbulent flow in the wake gradually diffuses into the uniform flow outside the wake, the wake slowly grows in dimensions. For wake measurements behind two turbines a horizontal growth rate of approximately $\Delta z/\Delta x = 12.5\%$ is calculated. Moreover, it has been observed that the vertical growth rate is only about 70% of the growth rate in horizontal direction, which can be ascribed to a blockage effect of the wind tunnel roof and the automatic traverse system located there.

Axial development of the wake turbulence intensity

Moving downstream in the wake, the turbulence intensities gradually decrease for all investigated turbine configurations. The further downstream the velocity field is scanned, the broader the turbulence intensity profiles become. The turbulent wake slowly diffuses into the surrounding flow. Moreover, the turbulence intensity profiles become visibly smoother further downstream in the wake due to turbulent diffusion processes in the center of the wake. The distinct vortices blur into one complex turbulent structure, which is characterized by a more uniform turbulence intensity profile.

Comparing the turbulence intensity levels of the three different turbine configurations (A), (B) and (C), significantly increased turbulence levels can be observed for the cases with an upstream turbine. Especially for the higher downstream distances 3D and 5D more than double as high turbulence intensities are measured in the center of the wake than for the unobstructed case. As the inflow to the second rotor standing in the wake of an upstream turbine is already very turbulent, the turbulence intensity levels seem to add up due to the additional turbulence generated by the second turbine rotor.

The turbulent inflow to the rotor is also assumed to be responsible for the faster mixing process in the wake behind an array of two turbines. Three distinct peaks can be found in the turbulence intensity profiles in the 1D wake for the unobstructed and both obstructed turbine arrangements. The left and right peak can be attributed to the vortices shed from the blade tips whereas the central peak stems from turbulence generated by the blade roots and the turbine nacelle. The 5D wake behind the array of two turbines is characterized by only one peak, whereas in the unobstructed configuration still two peaks in turbulence intensity are measured.

Wake asymmetries and turbine tower influence

Especially the near wake is characterized by a very asymmetrical flow field with high variations in mean velocity and turbulence intensity, when investigating the wake in the region behind the rotor swept area. Moving further downstream, the wake profile becomes more symmetrical and these variations gradually even out. The evident asymmetries in the near wake velocity and turbulence profiles are assumed to stem from the influence of the turbine tower. The flow exiting the rotor is in a rotating motion and is hitting the tower at a certain angle yielding an asymmetrical velocity distribution in the wake behind the turbine.

Furthermore, the presence of the tower causes an additional velocity deficit in the lower half of the scanned flow field. Due to the clockwise rotation of the rotor wake, the wake behind the turbine tower is visibly deflected.

Influence of the first turbine resp. the second turbine on the wake profiles

Comparing the wake measurements at different turbine separations distances, it is possible to evaluate the influence of the first turbine respectively the second turbine wake. It can be observed that the flow structures in the wake directly behind the rotor swept area are governed by the rotational motion of the second turbine rotor. The influence of the turbine separation distance is found to be insignificant to the basic flow structures in this part of the wake.

Comparing the dimensions of the wake profiles, the influence of the first turbine wake is evident. At all downstream distances the dimensions of the wake are visibly bigger, when the turbine separation distance is increased. As the first turbine wake is growing in radial direction with increasing downstream distance, the outer dimensions are assumed to be predominately influenced by the first turbine wake.

Tip speed ratio variations

When the tip speed ratio of the first wind turbine is set to a higher or lower tip speed ratio than at its maximum power point, a significant increase in the maximum power point of the second turbine performance curve can be observed. More kinetic energy is left in the flow, in case the first wind turbine is operated outside its design tip speed ratio. With the settings of the investigated test cases in the scope of this project, a speed-up or slow-down of the first turbine does however not yield an increase in the total power output of both turbines.

It can be concluded that the minimum velocity deficit in the wake behind the two turbines is very dependent on the tip speed ratio of the second turbine. The highest velocity deficit is found for a high second turbine rotational speed. Conversely, a low second turbine tip speed ratio yields comparatively low velocity deficits. For constant second turbine tip speed ratios, however, an operation of the first turbine at the optimum power point causes the highest velocity deficits. In this case, the maximum possible kinetic energy is extracted by the first turbine.

Evaluating the dimensions of the wake profiles, the tip speed ratio of the second turbine does not seem to have a significant influence. It is rather the influence of the first turbine tip speed ratio, which defines the width of the wake behind the array of the two turbines.
The most obvious asymmetries are found for low tip speed ratios of the second turbine. If the second turbine is driven at high rotational speeds, the velocity profiles in the wake are almost symmetrical. The obvious asymmetries at low rotational speeds of the second turbine are assumed to originate from a strong rotation in the rotor wake interacting with the turbine tower. Nevertheless, also high tip speed ratios of the first turbine increase the symmetry in the wake velocity profile. It is assumed that high first turbine rotational speeds cause increased turbulence levels in the incoming flow to the second turbine rotor, which intensify the turbulent mixing process in the wake.
The maximum turbulence intensities in the wake behind the second turbine are majorly influenced by the second turbine rotational speed. The highest turbulence intensities can be found for a high tip speed ratio of the second turbine, whereas the lowest turbulence intensities are measured for low second turbine rotational speeds. The influence of the first turbine tip speed ratio is found to be small.

7.2 Future work

Analyzing the results of the measurements performed during this project, a number of answers could be found but simultaneously even more questions popped up. A major topic of discussion in this paper is the evident asymmetries found in the velocity deficit and turbulence intensity profiles. Although the influence of the turbine tower is assumed to cause these asymmetries, a further investigation of this phenomenon could possibly help to associate the peaks in the wake profiles to interactions of the air flow with solid structures. A number of questions emerge: At which angles is the turbine wake hitting the tower? At which rotational speed is the wake rotating? Why are there unevenly distributed centers of high turbulence intensity and high velocity deficit in the near wake?
A vorticity analysis in the near wake could be a first step to find some answers to those questions. Therefore, velocity measurements in more than one dimension would have to be performed. Multi-wire CTA measurements or Pitot tube measurements with a five-hole probe could be convenient experimental techniques.

Evaluating the full area wake profiles, it is observed that the center of the maximum velocity deficit is located slightly underneath the center of the rotor in the 3D and 5D wake. A blockage effect due to the traverse system underneath the wind tunnel roof is assumed to be responsible for this displacement. Also, a lower-pressure region in the tower wake is suspected to cause a certain downshift in the wake. In order to assess the influence governing this phenomenon, it is recommended to perform a vertical traverse of the flow field using a simple manual traverse mechanism.

In the present experimental setup there are numerous possibilities of parameter variations. So far, both turbines are operated at their maximum power point at one pitch angle and one yaw angle. Two different turbine separation distances are investigated. In these cases, wake measurements at up to three downstream distances are performed. Moreover, the tip speed ratios of the two turbines are varied to three defined operating points. In the resulting nine test cases, however, the turbines are set up in only one separation distance. So far, only the 3D wake is investigated, but especially the 1D wake is assumed to give further knowledge about the dependency of asymmetries in the wake of the tip speed ratios of the two turbines. Additionally, a variation of the tip speed ratios

while the turbine separation distance is increased is assumed to yield some interesting results. Furthermore, full area wake measurements at different tip speed ratio combinations could clarify some flow phenomena in the wake.

Besides the turbine separation distance and the tip speed ratios, there are a number of other parameters that could be varied in the present experimental setup. A variation of the blade pitch angles of the first and/or second model wind turbine is expected to have a significant influence onto the flow structures in the wake behind the second turbine. In addition, a variation in yaw angle of the first and/or second model wind turbine would yield some relevant information about the development of the velocities and turbulences in the wake under yawed conditions.

In order evaluate an optimum turbine separation distance in a wind farm, the axial separation distance should be further increased. Also, a number of wake measurements further downstream in the wake would be favorable to estimate an appropriate turbine separation distance. For wake measurements up to 10-12D downstream and the present model size, the wind tunnel at NTNU's laboratory is not long enough. An implementation of the current test case into a CFD model could be a convenient tool to obtain some results at more downstream distances.
All the data acquired from the experiments performed in the wind could be useful as input data for an extensive CFD study of the same experimental setup. If a comparison of the CFD results to the experimental results yielded a sufficiently good correspondence, the CFD routines would represent a powerful tool to predict the aerodynamic behavior of wind turbines in a wind farm arrangement.

REFERENCES

[1] *Wind Energy Technology: An Introduction*
World Wind Energy Association
[Cited: 08 12, 2011.]
www.wwindea.org/technology/ch01/en/1_1.html

[2] Dogde, D.M.
Illustrated History of Wind Power Development
Telosnet, 2006. [Cited: 05 28, 2011.]
http://telosnet.com/wind/

[3] Manwell, J.F., McGowan, J., Rogers, T.
Wind Energy Explained: Theory, Design and Application
The Atrium, Southern Gate, Chichester, West Sussex, England
John Wiley & Sons Ltd, 2002

[4] Scanion, B.
Renewable Energy World
[Cited: 05 30, 2011.]
http://www.renewableenergyworld.com

[5] Sawyer, S. (Edt.)
Global Wind Report 2010
[Cited: 05 30, 2011.]
http://www.gwec.net

[6] *IEA Wind Annual Report 2010*
[Cited: 05 30, 2011.]
http://www.ieawind.org/AnnualReports_PDF/2009/Norway.pdf

[7] *Nordic Energy Solutions*
[Cited: 06 14, 2011.]
http://www.nordicenergysolutions.org

[8] *Centre for Environmental Design of Renewable Energy*
[Cited: 06 14, 2011.]
http://www.cedren.no

[9] European Environment Acency
Europe's onshore and offshore wind energy potential
EEA technical report No. 6/2009, ISSN 1725-2237

[10] Vermeer, L.J., Sørensen, J.N., Crespo, A.
Wind turbine wake aerodynamics
Progress in Aerospace Sciences, 2003, pp. 467-510

[11] Burton, T. et al.
Wind Energy Handbook
John Wiley & Sons Ltd., 2001

[12] Betz, A.
Das Maximum der theoretisch möglichen Ausnutzung des Windes durch Windmotoren
Zeitschrift für das gesamte Turbinenwesen, 1920

[13] *General Introduction to Wind Turbines*
[Cited: 06 27, 2011.]
http://www.earthscan.co.uk/Portals/0/Files/Sample%20Chapters/9781844074389.pdf

[14] Adaramola, M.S., Krogstad, P-Å.
Experimental Investigation of Wake Effects on Wind Turbine Performance
Renewable Energy, 2011. doi:10.1016/j.renene.2011.01.024

[15] Bertin, J.J.
Aerodynamics for Engineers, 4th Edition
Prentice Hall, 1994

[16] Karlsen, J.A.
Performance Calculations for a Model Turbine
Master's Thesis, EPT, NTNU Trondheim, 2009

[17] Gómez-Elvira, R. et al.
Anisotropy of turbulence in wind turbine wakes
Journal of Wind Eng. and Ind. Aerodynamics, Elsevier Ltd., 2005, No. 93, pp. 797–814

[18] Sørensen, J.N.
Modeling and Simulation of Wakes
Statkraft Wind Power Meeting, Uppsala, Sweden. 2011

[19] Sanderse, B.
Aerodynamics of wind turbine wakes - Literature review
Energy Research Centre of the Netherlands, 2009, ECN-E-09-016

[20] Steiness, C.
Aeolus Website
[Cited: 05 12, 2011.]
http://ict-aeolus.eu

[21] Ivanell, S. et al.
Three dimensional actuator disc modelling of wind farm wake interaction
Tönsberg, Sweden, 2008. WindSim User Meeting

[22] *Horns Rev Offshore Wind Farm*
[Cited: 06 14, 2011.]
http://www.hornsrev.dk/nyheder/brochurer/Horns_Rev_GB.pdf

[23] Barber, S., Chokani, N., Abhari, R.S.
Wind Turbine Performance and Aerodynamics in Wakes within Wind Farms
Brussels, Belgium, EWEA, 2011

[24] Barthelmie, R.J. et al.
Modelling and Measuring Flow and Wind Turbine Wakes in Large Wind Farms Offshore
Wind Energy 12, 2009, pp. 431-444

[25] Marmidis, G. et al.
Optimal placement of wind turbines in a wind park using Monte Carlo simulation
Renewable Energy Volume 33, Issue 7, 2008, p.1455-1460

[26] Johnson, K.E., Thomas, N.
Wind farm control: addressing the aerodynamic interaction among wind turbines
American Control Conference; St. Louis, MO, USA, 2009

[27] Krogstad, P-Å.
Modelltest av tidevannsturbin for Kvalsundet
MTF rapport 2002:5 (C), Institutt for Mekanikk, Termo- og Fluiddynamikk, NTNU

[28] Adaramola, M.S. and Krogstad, P-Å.
Performance and Near Wake Measurements of a Model Horizontal Axis Wind Turbine
Internal report NTNU, 2009

[29] Krogstad, P-Å., Lund, J.A.
An experimental and numerical study of the performance of a model turbine
Wind Energy, John Wiley & Sons, Ltd., 2011. DOI: 10.1002/we.482

[30] Somers, D.M.
The S825 and S826 Airfoils, Period of Performance: 1994 – 1995
National Renewable Energy Laboratory, Airfoils, Inc., 2005

[31] Dantec Dynamics
Constant Temperature Anemometry
[Cited: 06 14, 2011.]
http://www.dantecdynamics.com/Admin/Public/DWSDownload.aspx?File=files%2ffiler%2fsupport_and_download%2fresearch_and_education%2fcta.pdf

[32] Jørgensen, F.E.
How to measure turbulence with hot-wire anemometers - a practical guide
Skovlunde, Denmark; Dantec Dynamics, 2002. Publication no.: 9040U6151

[33] Adaramola, M.S., Krogstad, P-Å.
Model Tests of a Horizontal Axis Wind Turbine in Yawed Condition
Stockholm, Sweden, 2009. European Offshore Wind Conference and Exhibition

[34] Tennekes, H., Lumley, J.L.
A First Course in Turbulence
3rd edition, MIT Press, 1972

[35] Loland, K.
Wind Turbine In Yawed Operation
Master's Thesis, NTNU Trondheim, 2011

[36] Nygard, Ø.V.
Wake behind a horizontal-axis wind turbine
Master's Thesis, NTNU Trondheim, 2011

[37] Adaramola, M.S., Krogstad, P.-Å.
Wind Tunnel Simulation Of Wake Effects On Wind Turbine Performance
European Wind Energy Conference and Exhibition (EWEC), Warsaw, Poland, 2010

[38] Smith, D.A.
Multiple wake measurements and analysis
Proceedings of the 12th BWEA Wind Energy Conference
Norwich, UK, pp. 53–56, 1990

[39] Talmon, A.M.
A wind tunnel investigation on the effects of tower and nacelle on wind turbine wake flow
TNO Division of Technology for Society, 1984. Report 84-08479

[40] Talmon, A.M.
The wake of a horizontal axis wind turbine model, measurements in uniform approach flow and in a simulated boundary layer
TNO Division of Technology for Society, 1985. Report 85-01021

[41] Crespo, A. et al.
Experimental validation of the UPM computer code to calculate wind turbine wakes and comparison with other model
Journal of Wind Engineering and Industrial Aerodynamics, 1988, pp. 77-88

APPENDIX: COMPARISON OF PERFORMANCE CURVES

Three power and thrust curves of the unobstructed second turbine at three different wind tunnel inlet speeds are presented in *Fig. 6.5* in *chapter 6.2.1.2*. However, these curves are actually recorded for five different inlet speeds. The objective of the variation of inlet speed is to obtain a Reynolds-independent result, i.e. that the dimensionless curves do not change above a certain wind speed. The curves acquired for wind speeds of $U_\infty = 5.8\ m/s$, $U_\infty = 7.2\ m/s$, $U_\infty = 8.5\ m/s$, $U_\infty = 9.7\ m/s$ and $U_\infty = 11.5\ m/s$ are presented in *Fig. A.1.*

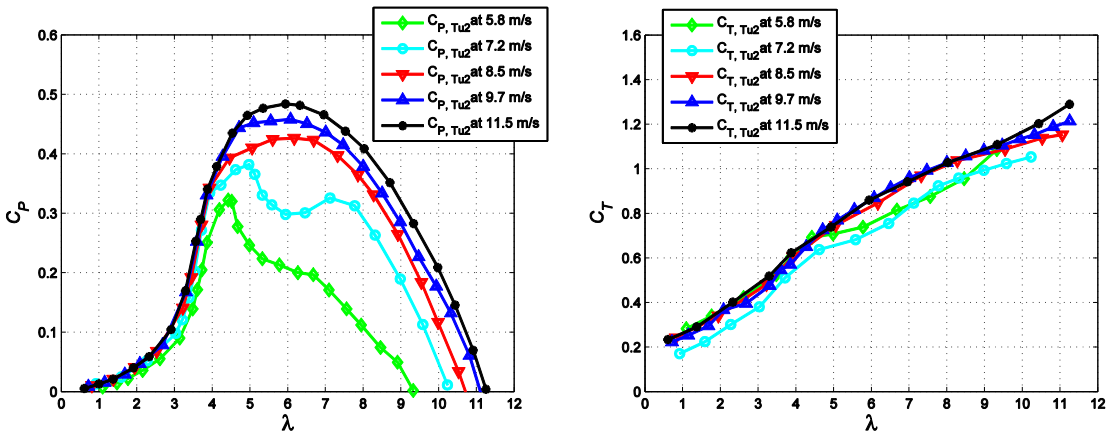

Fig A.1: *C_P and C_T curves of second turbine operating unobstructed at five different inflow wind speeds*

It can be observed, that the performance curves are not yet fully developed at $U_\infty = 5.8\ m/s$ and $U_\infty = 7.2\ m/s$ inflow speed. A distinct drop around the design tip speed of $\lambda = 6.0$ can be observed in the power and thrust curves for these inlet speeds. The inlet speed is too low that the flow entirely adheres on the blade profile. According to Karlsen [16], who comprehensively investigated the blade profiles of the model wind turbines, this effect can be ascribed to laminar separation bubbles near the blade leading edge, which can cause the flow to separate at too low Reynolds numbers.

These phenomena are consistent with the results found by Adaramola and Krogstad [28] on the same turbine. The power and thrust curves as recorded by Adaramola and Krogstad are shown in *Fig. A.2.*

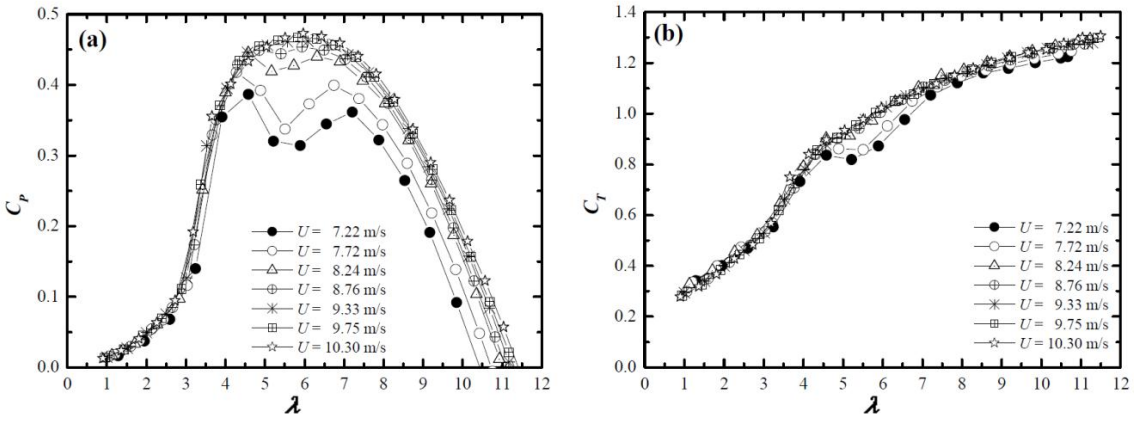

Fig A.2: *Reynolds number effect on model turbine performance characteristics [28]*

In contrast to the newly recorded performance curves, Adaramola and Krogstad found a certain drop in the power curves already for a wind speed lower than $U_\infty = 9\,m/s$ [28]. Also, laminar separation effects in certain sections of the blades were suspected to be responsible for this phenomenon.

Furthermore, Adaramola and Krogstad found Reynolds-independent power and thrust curves already at a wind tunnel inflow speed above $U_\infty = 9.0\,m/s$ [28]. In the present measurements as shown in *Fig. A.1*, however, the curves for $U_\infty = 9.7\,m/s$ and $U_\infty = 11.5\,m/s$ are very similar, but still not identical. Judging this correctly, the recorded performance curves are not yet Reynolds-independent.